

A DETAILED STUDY OF STAR FORMATION AT ITS COSMIC PEAK

A Dissertation

Presented to the Faculty of the Graduate School

of Cornell University

in Partial Fulfillment of the Requirements for the Degree of

Doctor of Philosophy

by

Cody James Lamarche

August 2019

© 2019 Cody James Lamarche

ALL RIGHTS RESERVED

A DETAILED STUDY OF STAR FORMATION AT ITS COSMIC PEAK

Cody James Lamarche, Ph.D.

Cornell University 2019

The star-formation-rate density of the universe has decreased by a factor of ~ 10 over the last 10 billion years, indicating a major change in either the efficiency with which galaxies form their stars or the availability of star-forming gas over the same time. In this thesis, we study the stellar populations within galaxies during the epoch of peak cosmic star-formation, ~ 10 billion years ago, using infrared observations of the ionized, neutral, and molecular phases of the interstellar medium (ISM) therein. In particular, we focus on two galaxies within this era, both of which have vigorous star-formation as well as active galactic nuclei (AGN), in an effort to learn more about the modes of star-formation at early times as well as the influence of AGN feedback on star-formation.

As a first example, we examine the stellar population within 3C 368, a Fanaroff-Riley Class II (FR-II) galaxy at redshift 1.131. Our observations suggest a powerful AGN, accompanied by vigorous and extended star formation. We estimate the age of the starburst and find that it is nearly concurrent with the latest episode of AGN flaring, suggesting a link between the growth of the supermassive black hole and stellar population in this source. Our ionized-gas observations suggest a low gas-phase metallicity within this source, consistent with the weak molecular gas lines that we observe. We suggest that perhaps 3C 368 is accreting pristine molecular gas from an external source, thereby diluting its gas-phase metallicity.

For our second example, we investigate the star-formation within SDP.11,

a gravitationally-lensed galaxy at redshift 1.783. Our high-resolution gas and dust-continuum observations show intense star-formation in this source extended over several kiloparsecs. Gravitational-lens modeling further indicates that the star formation in this source is extended over a 3-5 kpc rotating disk, suggesting that the starburst present here may not be the result of a major merger, as is the case for local ultraluminous infrared galaxies (ULIRGs), but some other mechanism.

The findings presented in this thesis support the idea of a different mode of star-formation being present in high-redshift galaxies. In contrast to local ULIRGs, which have intense star-formation confined to their centers, we find kiloparsec-scale star-forming disks present in galaxies during the epoch of peak cosmic star-formation. While local star-forming galaxies tend to be the product of major-mergers, high-redshift starburst galaxies may well be the product of another process, perhaps accretion of material from the cosmic web.

BIOGRAPHICAL SKETCH

Cody Lamarche grew up in Newport, Vermont, a small town just south of the Canadian border. He received Bachelor of Science (BS) degrees in both physics and mathematics from the University of Vermont in 2013. Cody joined the Cornell Department of Astronomy's graduate program in the fall of the same year, conducting research with Professor Gordon Stacey, and received his Ph.D. in 2019.

This work is dedicated to my parents, Pierre and Tina, my brother Joel, and my grandparents, George and Shirley. It would not have been possible without their support and encouragement.

ACKNOWLEDGEMENTS

Being a part of the Astronomy graduate program at Cornell has been the most rewarding experience of my life, thanks to the people I've met along the way. With you folks, the program was more than just a group of coworkers, it was truly a family. It would be impossible to list everyone who has helped me on this journey, so here I acknowledge just a few of the people that made my time here so enjoyable.

First, I'd like to thank my advisor Gordon Stacey. He is genuinely clever without ever taking himself too seriously; I admire his character greatly. I've had so much fun working with Gordon over the past six years and have learned a lot. I'd also like to thank Thomas Nikola, who's stick-to-itiveness and hard work were always an inspiration.

Over the past few years, I've also made some of the best friends anybody could ask for: Paul Corlies and Matt Hankins - from the 1st-year adventures of Jackson, house parties, and maybe a small fire, to recent thesis defenses and celebrations at the Creeker, I'm so glad to have experienced this journey with you two. Pato and Alexandra Gallardo - you are some of the nicest, most down-to-earth, people I know. Your friendship is worth more to me than I can say. Amit Vishwas - probably the most brilliant person I've ever met, I couldn't have made it through the grad program without your help and great advice. Avani Gowardhan (a.k.a. "The Meter-of-Evil") - now that you're in Boston, I can say, without fear of being mocked (by you, that is), that I really enjoyed our time together. Your sarcastic sense of humor always made me smile! Oscar Castaneda Fernandez, Jean Teyssandier, and Maryame El Moutamid - dinners with you all were so much fun! Sam and Michelle Birch – I'll miss the yearly prediction of the Winnipeg Jets' 1st Stanley-Cup victory. I'm going to make the predic-

tion that (regardless of when you’re reading this thesis) the Winnipeg Jets still haven’t won the cup! Kassandra Anderson - the porch parties, and “All That Jazz,” were so much fun! Riccardo Pavesi and Daisy Leung – I always enjoyed having scientific conversations with you. Tyler Pauly, Mike Jones, Michael Lam, and Luke Leisman – you all were great role models for me, and I have a tremendous amount of respect for you all. I’d also like to say a big thank-you to the Astronomy Grads Network (AGN) for organizing events, including trivia (Go “Rob Ford Fan Club”!), that kept the department lively and fun throughout my time as a graduate student.

I was also lucky enough to find a group of people at Cornell who share my passion for music. Meetings of the Astrophysics Piano Club (we never really came up with a name, so I’m going with that) were so much fun! I’d like to thank Ann Harch, Cynthia Lunine, Mary Mulvanerton, Michelle Birch, and especially Alexandra Gallardo, who stuck with me for many hours in the practice rooms of Lincoln Hall despite all the cringe-worthy notes and never once hit my knuckles with her violin bow!

I wouldn’t have been able to navigate the maze that is grad school without the support and friendship of Monica Carpenter, Mary Mulvanerton, Jessica Sutliff, Bez Thomas, Tom Shannon, Melanie Wetzel, Pam Smith, Patricia Fernandez de Castro Martinez, Jill Tarbell, Cheryl Neville, and of course Lynda Sovocool. I’ll never forget the day several of us flew angry-bird balloons into Lynda’s office, with Wagner’s “Ride of the Valkyries” blaring, or the scowl that we got for it. Despite that scowl, I’m still one of Lynda’s best friends...just ask her!

Also, sports! I want to thank Luke Leisman for rebooting “The Big Bangers,” the Astronomy department’s intramural softball team, and Matt Hankins for

taking up the mantle afterward. We didn't win the most games, but we sure had a great barbeque when the season ended! Last year, we somehow managed to win the losers' bracket of the playoffs. Go Big Bangers! I also enjoyed playing weekly ping-pong with Alexandra Gallardo, Brian Koopman, Antoine Chapelain, and Nate Rider.

I would further like to thank my collaborators beyond Cornell, including Carl Ferkinhoff, Drew Brisbin, Sarah Higdon, and Jim Higdon, for very helpful scientific discussions and advice.

Finally, I would like to thank Martha Haynes, Ira Wasserman, and Dong Lai, for being such supportive members of my special committee and for reading this thesis.

TABLE OF CONTENTS

Biographical Sketch	iii
Dedication	iv
Acknowledgements	v
Table of Contents	viii
List of Tables	x
List of Figures	xi
1 Introduction	1
1.1 The evolution of star formation over cosmic time	1
1.2 Feedback on star formation	4
1.3 Studying star formation	6
1.4 Ionized gas	9
1.4.1 FIR fine-structure lines	11
1.4.2 Radio free-free emission and gas-phase metallicity	15
1.4.3 Radiation field hardness	19
1.5 Neutral gas	21
1.5.1 Neutral gas tracers	22
1.5.2 Gas mass from optically-thin tracers	24
1.6 Molecular gas	30
1.6.1 CO	30
1.6.2 Thermal dust continuum	35
1.7 Telescopes	38
1.7.1 ALMA	38
1.7.2 Herschel	39
1.8 Overview of thesis	40
2 CO-Dark Star Formation and Black Hole Activity in 3C 368 at z = 1.131: Coeval Growth of Stellar and Supermassive Black Hole Masses	42
2.1 Introduction	42
2.2 Observations	44
2.2.1 Herschel/PACS	44
2.2.2 PdBI	45
2.2.3 ALMA	46
2.2.4 Spitzer/IRS	48
2.3 Results and Discussion	48
2.3.1 Line Fluxes	48
2.3.2 Neon Lines: Disentangling the AGN Contribution	56
2.3.3 H II region Models	57
2.3.4 Bounds on the N/O Ratio	60
2.3.5 Photodissociation Regions	61
2.3.6 Where is the CO?	65
2.4 Future Observations	69
2.5 Conclusions	69

3	Resolving Star Formation on Subkiloparsec Scales in the High-Redshift Galaxy SDP.11 Using Gravitational Lensing	71
3.1	Introduction	71
3.2	Observations and Data Reduction	75
3.2.1	ALMA	75
3.2.2	Herschel/PACS	76
3.2.3	Herschel/SPIRE	76
3.3	Results and Discussion	77
3.3.1	Line and Continuum Fluxes	77
3.3.2	Dust Opacity	82
3.3.3	H II Regions	85
3.3.4	PDRs	92
3.3.5	Lens Modeling	98
3.4	Conclusions	104
4	CO and Fine-Structure Lines Reveal Low Metallicity in a Stellar-Mass-Rich Galaxy at $z \sim 1$?	106
4.1	Introduction	106
4.2	Observations and Data Reduction	108
4.2.1	ALMA	108
4.3	Results and Discussion	109
4.3.1	Line and Continuum Fluxes	109
4.3.2	Continuum Science	112
4.3.3	PDRs	120
4.3.4	Dynamical Mass	126
4.4	Conclusions	126
5	Summary and future work	129
5.1	Star formation during the peak epoch	129
5.2	Future work	131
5.2.1	FIR abundance determinations in nearby galaxies	132
5.2.2	The James Webb Space Telescope	134

LIST OF TABLES

2.1	Spectral lines observed in 3C 368	55
2.2	Line corrections for PDR modeling	65
3.1	Spectral lines observed in SDP.11	84
3.2	Radio-continuum observations of SDP.11	85
3.3	Best-fit gravitational-lensing parameters for SDP.11	99
4.1	Spectral-line and continuum observations of 3C 368	112
4.2	Physical properties of 3C 368	127

LIST OF FIGURES

1.1	Star-formation rate density through cosmic time	2
1.2	The galaxy main-sequence	3
1.3	The black-hole bulge-mass correlation	5
1.4	The baryonic mass-function of field galaxies	7
1.5	Schematic showing the phases of the ISM surrounding sources of ionizing photons	9
1.6	Ground-state fine-structure splitting of the N ⁺ and O ⁺⁺ ions . .	11
1.7	The level populations of the the O ⁺⁺ and N ⁺ ions with electron density	14
1.8	Normalized line emissivity (ϵ_λ) for the ground-state fine-structure transitions of the O ⁺⁺ and N ⁺ ions	16
1.9	H II-region density from the ratio of O ⁺⁺ and N ⁺ lines	17
1.10	Determining the hardness of the radiation field from a ratio of spectral lines	20
1.11	Ground-state fine-structure splitting of the C ⁺ ion and O ⁰ atom .	22
1.12	Determining the fractional emission of [C II] from ionized-gas regions	25
1.13	PDR modeling with [C II], [O I], and FIR	26
1.14	The affects of metallicity on CO-based gas-mass determinations .	34
2.1	Spectral lines observed in 3C 368 with <i>Herschel/PACS</i>	51
2.2	1.3 mm and 205 μm rest-frame continuum maps of 3C 368 . . .	52
2.3	Spectral lines observed in 3C 368 with <i>Spitzer/IRS</i>	53
2.4	PDR best-fit parameters for 3C 368	54
3.1	ALMA [C II] 158 μm map of SDP.11	79
3.2	ALMA [C II] 158 μm spectrum of SDP.11	80
3.3	<i>Herschel/PACS</i> spectra of SDP.11	81
3.4	Radio-SED decomposition of SDP.11	89
3.5	[C II]/FIR ratio map of SDP.11	95
3.6	[C II]/FIR vs. Σ_{SFR} in SDP.11	96
3.7	Gravitational-lens models of SDP.11	101
3.8	Lens-corrected [C II] spectrum of SDP.11	103
4.1	ALMA CO(4-3) and [C I] 609 μm maps of 3C 368	111
4.2	225.5 GHz and 8.21 GHz (observed-frame) continuum maps of 3C 368	113
4.3	ALMA CO(4-3) and [C I] 609 μm spectra of 3C 368	114
4.4	Radio-SED decomposition of 3C 368	116
4.5	Updated best-fit PDR-parameters for 3C 368	122
5.1	Mass-metallicity relation using optical tracers	133

CHAPTER 1

INTRODUCTION

1.1 The evolution of star formation over cosmic time

Over the past few decades, great strides have been made in understanding the star-formation history of the universe. We now know that in its prime, ~ 10 billion years ago, the universe formed stars at a rate $\sim 10\times$ what it does today (see e.g., [Madau & Dickinson, 2014](#), and Figure 1.1). Where the Milky Way currently forms stars at a rate of $\sim 1 M_\odot \text{ yr}^{-1}$, ancient galaxies formed stars at rates in excess of ~ 100 's $M_\odot \text{ yr}^{-1}$. Why did galaxies form stars so vigorously at early times? And what caused the ensuing decline in the cosmic star-formation rate? Was there more molecular gas available to fuel star-formation in the early universe, or did the galaxies of the past somehow convert their gas into stars more efficiently than is done now? Were the modes of star formation different in the past?

One major clue to answering these questions was the emergence, over the past decade or so, of an observed relationship between the mass of galaxies and their star-formation rates. Dubbed the ‘galaxy main-sequence,’ it is the correlation between the star formation rate (SFR) and stellar mass (M_*) in ‘normal’ galaxies (see e.g., [Daddi et al., 2007](#), and Figure 1.2). As naïvely expected, more massive galaxies tend to form stars more quickly than do less massive galaxies, but the normalization of this relation is observed to evolve with time. The star-formation rate corresponding to a fixed stellar mass is observed to be higher at a lookback time of 10 billion years than at present. Or, equivalently stated, the specific star formation rate, $s\text{SFR} \equiv \text{SFR}/M_*$, and hence the slope of the galaxy

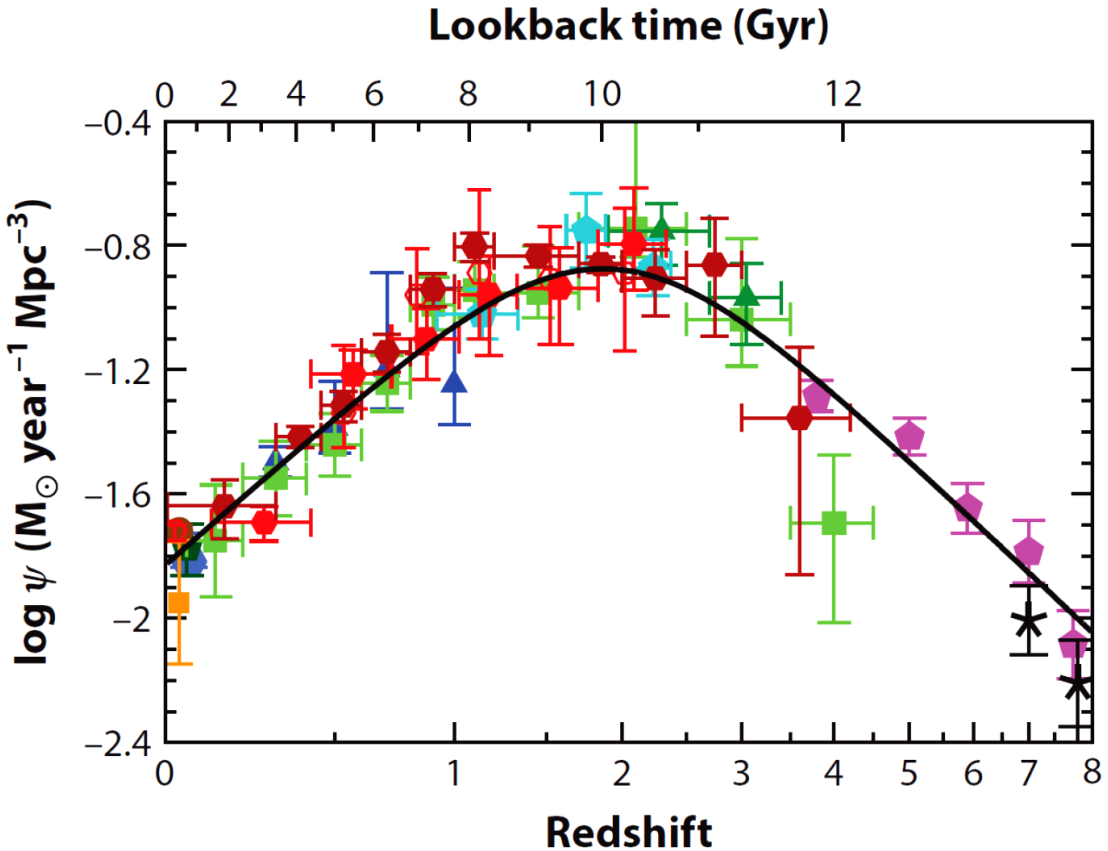


Figure 1.1 A plot showing the cosmic star-formation rate per comoving volume (Ψ) as a function of time, measured in the infrared (red, orange) and ultraviolet (green, blue, purple) (adapted from [Madau & Dickinson, 2014](#)).

main-sequence, is roughly constant at a given epoch, but varies with time. Why should this be the case?

The answer seems to be that the availability of molecular gas, the fuel for star formation, is the main driver of the variation in star-formation rate at a given epoch, with more molecular gas equating to a higher star-formation rate. However, the mode of star formation also changes between low- and high-redshift galaxies, suggesting a different star-formation mechanism, with a higher star-formation efficiency ($SFE \equiv SFR/M_{gas}$), in high-redshift galaxies (e.g., [Scoville et al., 2016](#)). So what are the different modes of star formation in high- and

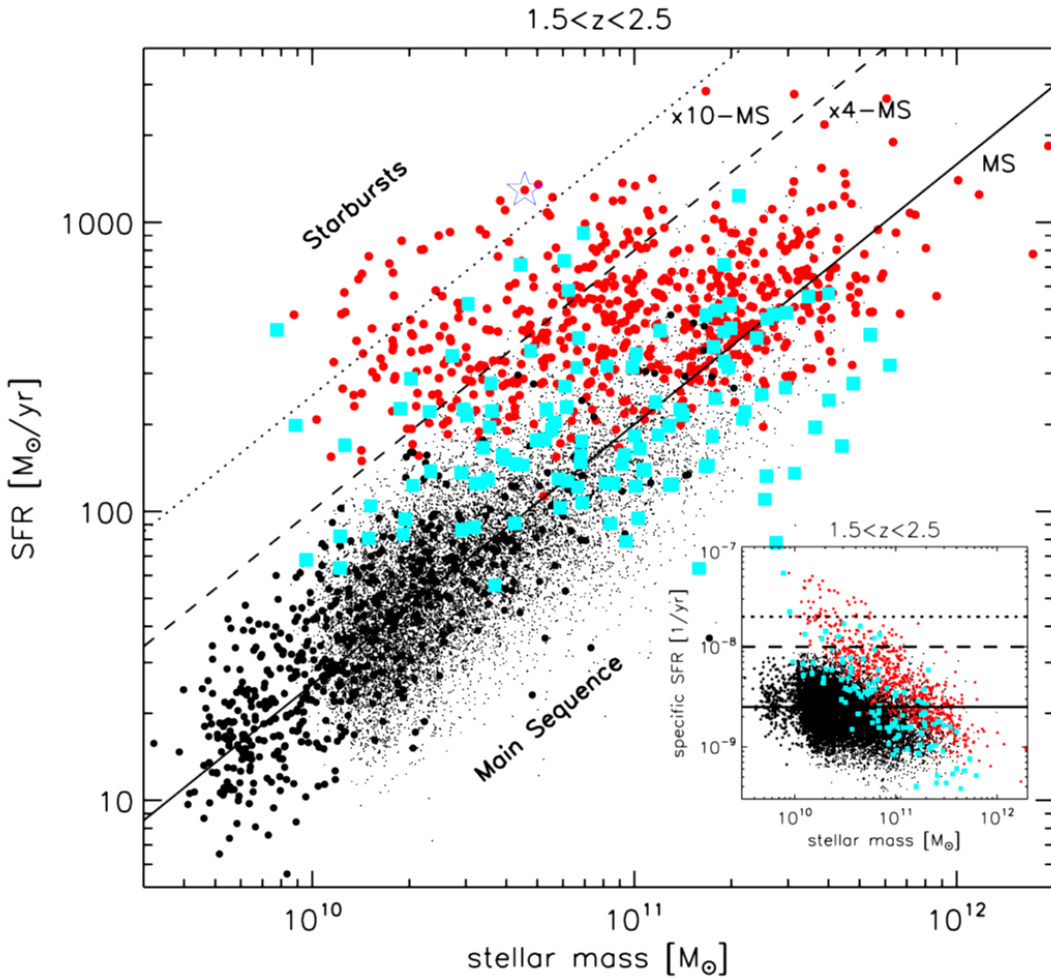


Figure 1.2 A plot showing the star formation rate (SFR) as a function of stellar mass (M_*), measured in a sample of galaxies between $1.5 < z < 2.5$. The ‘galaxy main-sequence’ is indicated by the solid black line, while galaxies lying $4\times$ and $10\times$ above the main-sequence, termed ‘starburst galaxies’, are indicated by the dashed and dotted black lines, respectively. The inset image shows that the specific star formation rate, $s\text{SFR} \equiv \text{SFR}/M_*$, is roughly constant with M_* at a given epoch (adapted from Rodighiero et al., 2011).

low-redshift galaxies?

The theory here is that early galaxies primarily accreted their gas from the cosmic web, whereas modern-day galaxies no longer have that option and instead tend to form stars rapidly only after violent merger events (e.g., Dekel et al., 2009, Kereš et al., 2005). This theory is backed up by observations, which show that high-redshift galaxies tend to have large-scale star-formation extended over kiloparsec-size disks (e.g., Brisbin et al., 2015, Genzel et al., 2010, Stacey et al., 2010b), whereas local star-forming galaxies tend to have concentrated star-formation at their centers, where the gas accreted during major-merger events is funneled (e.g., Armus et al., 1987).

1.2 Feedback on star formation

In addition to the availability of molecular gas, and the method of gas accretion, changing with time, internal factors, such as active galactic nuclei (AGN) and supernova (SN) explosions, can also affect a galaxy's ability to form stars. We use the term 'feedback' to describe processes which modify a galaxy's ability to produce stars. Feedback comes in two flavors, 'positive' and 'negative', the former describing processes which bolster star formation within a galaxy, while the latter describes processes which inhibit star formation. At the time of writing this thesis, papers are frequently published invoking both forms of feedback. Here we briefly describe some of the observations which suggest the need for feedback.

The first line of observational evidence for feedback is the black-hole bulge-mass correlation (e.g., Ferrarese & Merritt, 2000, see Figure 1.3). It has been ob-

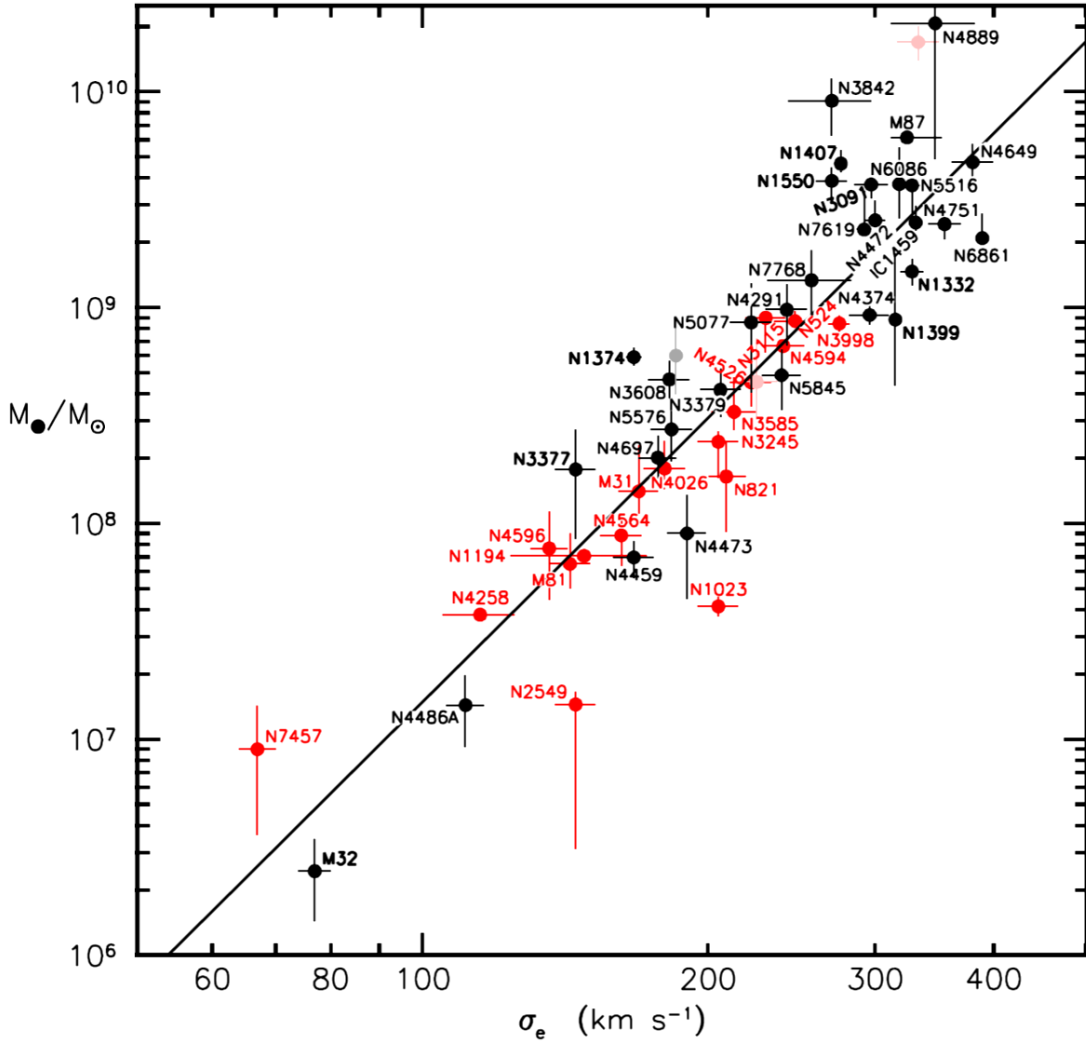


Figure 1.3 A plot showing the mass of central supermassive black holes (M_*) as a function of the dispersion velocity (σ_e) of the central stellar bulge. The observed relation suggests that the stellar population and supermassive black hole contained within a galaxy co-evolve (adapted from Kormendy & Ho, 2013).

served in many galaxies that the mass of the central supermassive black hole and the velocity dispersion, and hence mass, of the surrounding stellar bulge are tightly correlated. This suggests a kind of co-evolution between the supermassive black holes and stellar populations within galaxies, potentially with the growth of one regulating the growth of the other through a feedback mechanism.

Another important observational piece of evidence for feedback is the down-turn in the baryonic mass-function of field galaxies at both the high- and low-mass ends (e.g., [Read & Trentham, 2005](#), see Figure 1.4). When the number density of galaxies per comoving volume is plotted as a function of their mass (called a ‘mass function’), a power-law distribution is broadly found. This is to be expected, as the underlying dark-matter mass-function is also a power-law, such that multiplying the dark-matter mass-function by the baryon fraction should, to first order, yield the galaxy mass-function. It is observed, however, that there is a dearth of galaxies both at the high- and low-mass ends of the mass function. At the low-mass end, this lack of galaxies has been explained by feedback from supernova, which explode and disrupt the small gravitational potential wells of such galaxies, driving the gas reservoir out and quenching star formation therein. For more massive galaxies, which are less affected by supernova explosions, AGN feedback is invoked as a mechanism to quench star formation: the launching of jets from AGN accretion driving out the gas reservoir.

1.3 Studying star formation

Recent star formation is best traced by stars on the high-mass ($\geq 8 M_{\odot}$) end of the stellar main-sequence. This is because these stars (primarily O- and B-type stars) have very short lifetimes (~ 10 Myrs), and hence exist only in regions where recent star-formation has taken place. These stars are also the primary sources of hard ionizing photons, such that they strongly affect the surrounding interstellar medium (ISM). Observations of the ultraviolet (UV) continuum emitted by these stars would be a direct tracer of recent star formation, however

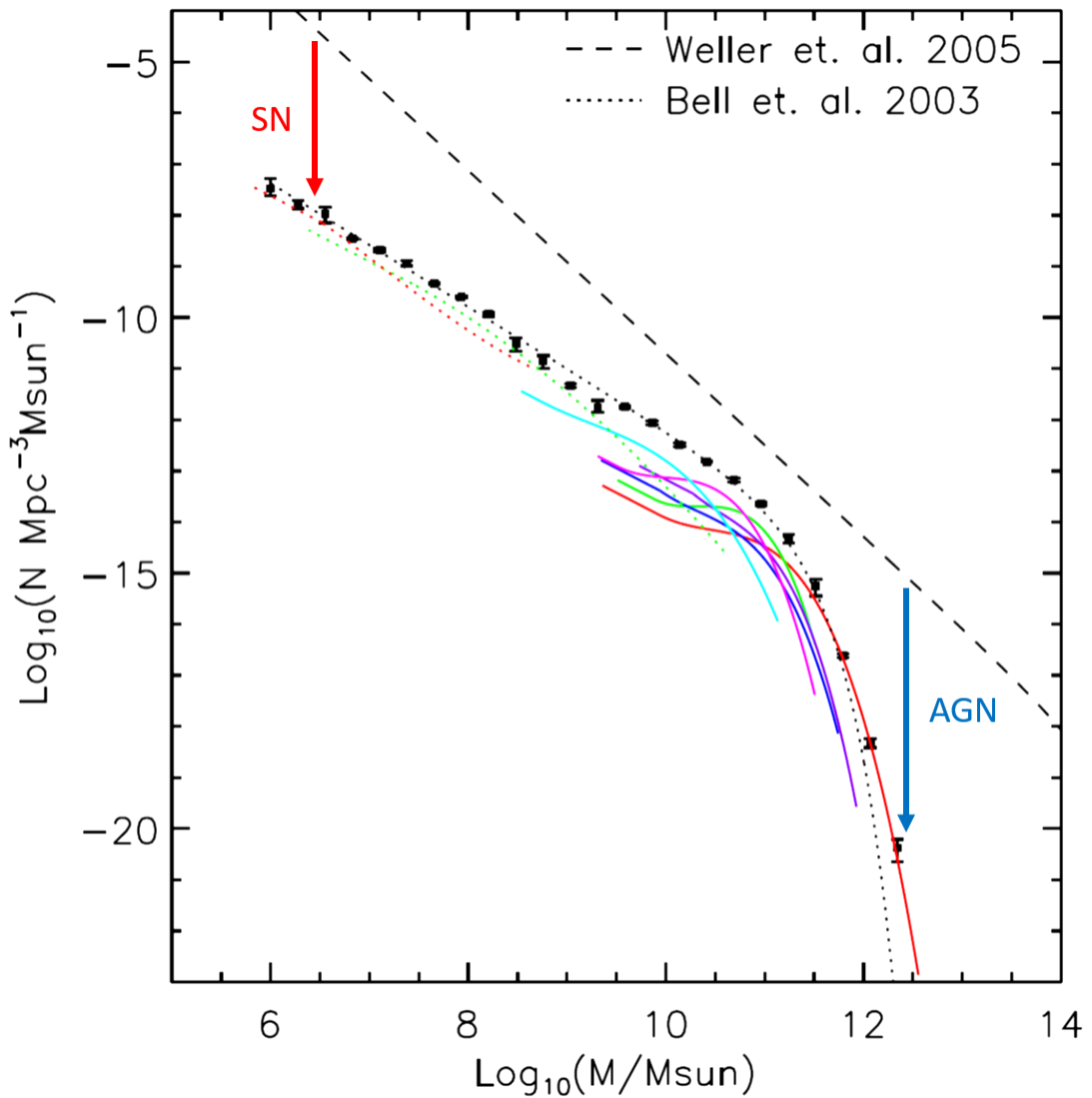


Figure 1.4 A plot showing the baryonic mass-function of field galaxies. Note that the observed mass function (black data points) tends away from the theoretical power law (black dashed line) at both the high- and low-mass ends. This is theorized to be due to feedback from supernova (SN) explosions at the low-mass end and active galactic nuclei (AGN) at the high-mass end, both of which are expected to quench star formation in their respective host galaxies, leading to the observed deviation from the theoretical values at both mass extremes. The colored lines show the baryonic mass-functions by galaxy classification (solid lines: red - E, green - S0, blue - Sa, purple - Sb, magenta - Sc, cyan - Sd; dotted: green - Irr, red: dE) (adapted from [Read & Trentham, 2005](#)).

these observations are not generally feasible. Dust and neutral gas in the ISM of the star’s host-galaxy heavily obscure and absorb the UV light, such that a proxy for these high-energy photons must be observed instead. This dust obscuration becomes very pronounced when observing highly star-forming galaxies, which also tend to be very dusty. The dust grains in these galaxies absorb much of the UV continuum emitted by young stars and re-emit that power thermally in the far-infrared (FIR). As such, the FIR continuum, which was down-converted from the UV continuum emitted by the young stellar population, can be used to estimate the star-formation rate within dusty star-forming galaxies (e.g., Kennicutt, 1998),

$$SFR = 4.5 \times 10^{-44} L_{FIR}, \quad (1.1)$$

$$\text{M}_\odot \text{ yr}^{-1}$$

where L_{FIR} is the integrated FIR luminosity in units of erg s^{-1} .

Studying the ISM of star-forming galaxies can yield much more information than just the star-formation rate. In the next few sections, we outline some of the observational methods, and the theory behind these methods, used for studying the interstellar medium (ISM) and star formation within galaxies. These sections are organized such that they follow the photons progressively through the zones of the ISM, from the regions of ionized gas surrounding the stars where the photons are emitted, through the transitional zones of neutral gas, and finally into the clouds of molecular gas (see Figure 1.5).

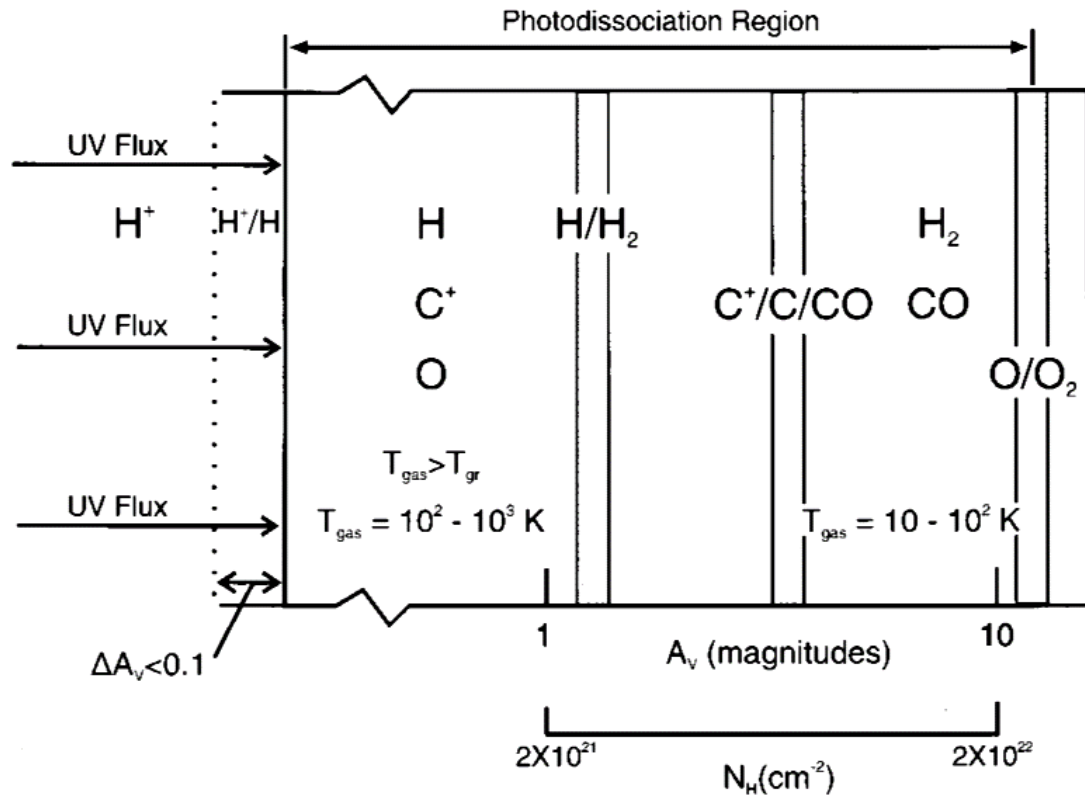


Figure 1.5 A schematic showing the phases of the ISM surrounding sources of ionizing photons, from the regions of ionized gas (left), through the photo-dissociation regions (center), and finally into the molecular clouds (right) (adapted from Hollenbach & Tielens, 1999).

1.4 Ionized gas

Regions of ionized gas, referred to as H II regions, or Strömgren spheres, are bubbles of plasma surrounding sources of hard radiation, such as young stars or AGN. These sources emit an appreciable number of photons with energies $> 13.6 \text{ eV}$ (called Lyman-continuum photons) capable of keeping the hydrogen atoms in their vicinity in an ionized state. When enveloped in neutral gas such that the size of the H II region is limited by the ionizing flux - an "ionization limited H II region" - the size of the ionized regions can be estimated by considering the volume over which the rate of ionization and recombination of hydrogen

atoms are balanced:

$$N_{Ly} = r_r V = \alpha_H n_e n_p \frac{4}{3} \pi R_S^3, \quad (1.2)$$

where N_{Ly} is the number of Lyman continuum photons emitted by the ionizing source per second, r_r is the hydrogen recombination rate ($\text{cm}^{-3} \text{ s}^{-1}$), V is the volume of the Strömgren sphere, α_H is the hydrogen recombination coefficient ($\sim 3 \times 10^{-13} \text{ cm}^3 \text{ s}^{-1}$), n_e and n_p are the number densities of electrons and protons (cm^{-3}), respectively, and R_S is the radius of the Strömgren sphere. This equation can be solved for the radius of the sphere of ionized gas (see, for example, [Osterbrock & Ferland, 2006](#), for details of the derivation):

$$R_S = \left(\frac{3N_{Ly}}{4\pi\alpha_H n_e n_p} \right)^{1/3}. \quad (1.3)$$

As an example, an O5 star emits $\sim 6 \times 10^{49}$ Lyman-continuum photons per second. In a region where $n_e \sim n_p \sim 1,000 \text{ cm}^{-3}$, the radius of the Strömgren sphere, R_S , is $\sim 1.2 \text{ pc}$.

In regions surrounding sources of harder photons still, metals can be ionized in addition to hydrogen. For example, the formation energy of the O^{++} and N^+ ions are 35.12 eV and 14.53 eV, respectively. This differing ionization energy provides a way to determine the hardness of the radiation field emitted by the sources of the ionizing photons: observe spectral lines emitted by species with differing ionization potential and recover the ionization state of the H II region, and hence the properties of the sources ionizing the gas.

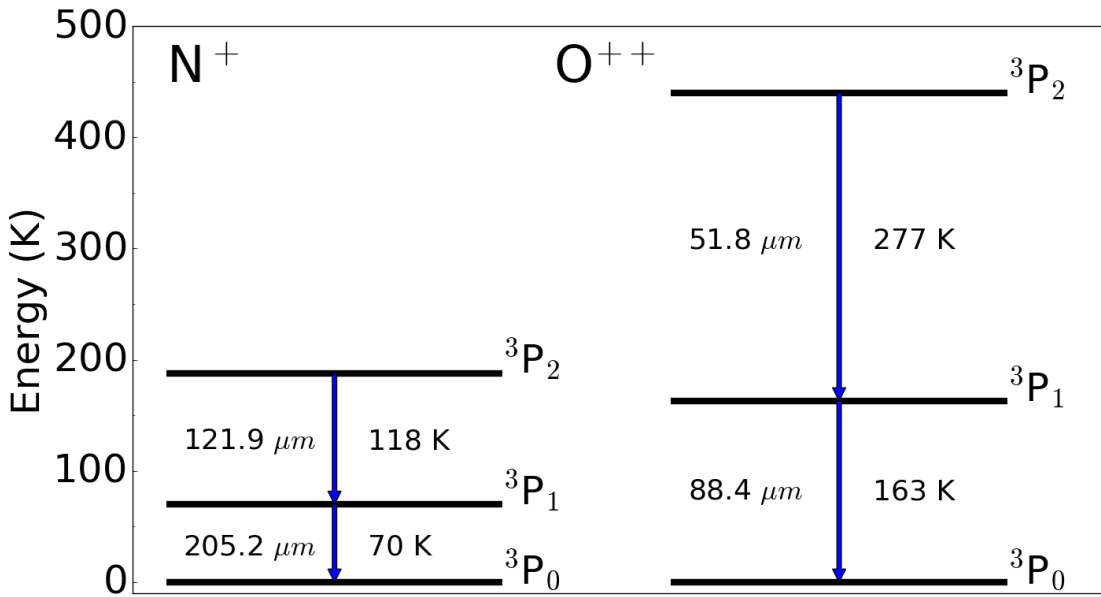


Figure 1.6 Energy level diagram showing the ground-state fine-structure splitting of the N^+ (left) and O^{++} (right) ions.

1.4.1 FIR fine-structure lines

The ground-state fine-structure splitting of multi-electron atoms and ions, such as carbon, oxygen, and nitrogen, gives rise to the far-infrared (FIR) fine-structure lines. Lying only several hundred kelvin above ground, these transitions require very little in the way of excitation energy, and, since they occur in H II regions which have electron temperatures of the order 8000 K, they are relatively insensitive to the temperature of the collisional partners which excite them (see Figure 1.6). At such long wavelength, these transitions also suffer very little from dust extinction. Taken together, these properties make the FIR fine-structure lines extremely attractive probes of the interstellar medium, requiring little in the way of corrections from modeling.

Let us consider a generic three-level system (appropriate for the O^{++} and N^+ ions, for example), with energy levels denoted by the subscripts 0, 1, and 2.

Let us further assume that the line transitions for this system are optically thin (hence, we may ignore absorption and stimulated emission). Detailed balance requires that the rates in to and out of each state be matched, yielding the following set of equations which relate the populations in the three energy states:

$$\begin{aligned}
 q_{02}n_0n_e + q_{12}n_1n_e &= A_{21}n_2 + q_{21}n_2n_e + q_{20}n_2n_e \\
 A_{21}n_2 + q_{21}n_2n_e + q_{01}n_0n_e &= A_{10}n_1 + q_{10}n_1n_e + q_{12}n_1n_e \\
 q_{20}n_2n_e + q_{10}n_1n_e + A_{10}n_1 &= q_{01}n_0n_e + q_{02}n_0n_e \\
 n_0 + n_1 + n_2 &= n_{total}
 \end{aligned} \tag{1.4}$$

where q_{ij} ($\text{cm}^3 \text{ s}^{-1}$) is the collisional rate coefficient between states i and j, given by

$$q_{ij} = \frac{h^2 \gamma_{ji}}{g_i (2\pi m_e)^{1.5} (kT)^{0.5}} \exp\left(-\frac{h\nu_{ji}}{kT}\right) \approx 8.629 \times 10^{-6} \frac{\gamma_{ji}}{g_i \sqrt{T}} \exp\left(-\frac{h\nu_{ji}}{kT}\right), \tag{1.5}$$

for the upward transition ($j > i$). One can show (e.g., [Osterbrock & Ferland, 2006](#)) that the downward collisional rate coefficient is related to the upward rate by:

$$q_{ji} = \frac{g_i}{g_j} q_{ij}, \tag{1.6}$$

γ_{ij} is the symmetric ($\gamma_{ij} = \gamma_{ji}$) collision strength, g_i is the degeneracy of state i, n_j (cm^{-3}) is the number density of particles in the state j, n_e (cm^{-3}) is the number density of electrons (the collisional partner of ions within H II regions), and A_{ij} (s^{-1}) is the Einstein A-coefficient for the downward transition between states i

and j. Within these fine-structure terms the radiative transition from level 2 to 0 is highly forbidden ($\Delta J = 2$) so that it is ignored in this analysis. This system of equations can be solved for the ratio of level populations between adjacent states:

$$\frac{n_2}{n_1} = \frac{q_{12}n_e(q_{01}n_e + q_{02}n_e) + q_{02}n_e(A_{10} + q_{10}n_e)}{(A_{21} + q_{21}n_e + q_{20}n_e)(q_{01}n_e + q_{02}n_e) - q_{20}n_e q_{02}n_e} \quad (1.7)$$

$$\frac{n_1}{n_0} = \frac{(A_{21} + q_{21}n_e + q_{20}n_e)(q_{01}n_e + q_{02}n_e) - q_{20}n_e q_{02}n_e}{(A_{21} + q_{21}n_e + q_{20}n_e)(A_{10} + q_{10}n_e) + q_{20}n_e q_{12}n_e}.$$

Figure 1.7 plots the level populations in the three levels of the fine-structure-split ground-state as a function of electron density for both the O⁺⁺ and N⁺ ions.

Given that we observe line emission from the radiative transitions, it is useful to examine the line intensity produced by these transitions, from an upper state (u) to a lower state (l):

$$I = \frac{h\nu_{ul}}{4\pi} \frac{n_u}{n_{total}} A_{ul} N_{total}, \quad (1.8)$$

erg s⁻¹ cm⁻² sr⁻¹

where ν_{ul} is the emission-line frequency for the transition between the upper and lower states, N_{total} is the total column of the emitting particles ($N_{total} \equiv n_{total}D$, where D is the thickness of the emitting slab), and h is the Planck constant. We can rewrite this equation in a more useful form:

$$I = \frac{h\nu_{ul}}{4\pi} \frac{n_u A_{ul}}{n_{total} n_e} n_e N_{total} = \epsilon_{ul} \frac{n_{total}}{n_e} n_e^2 D, \quad (1.9)$$

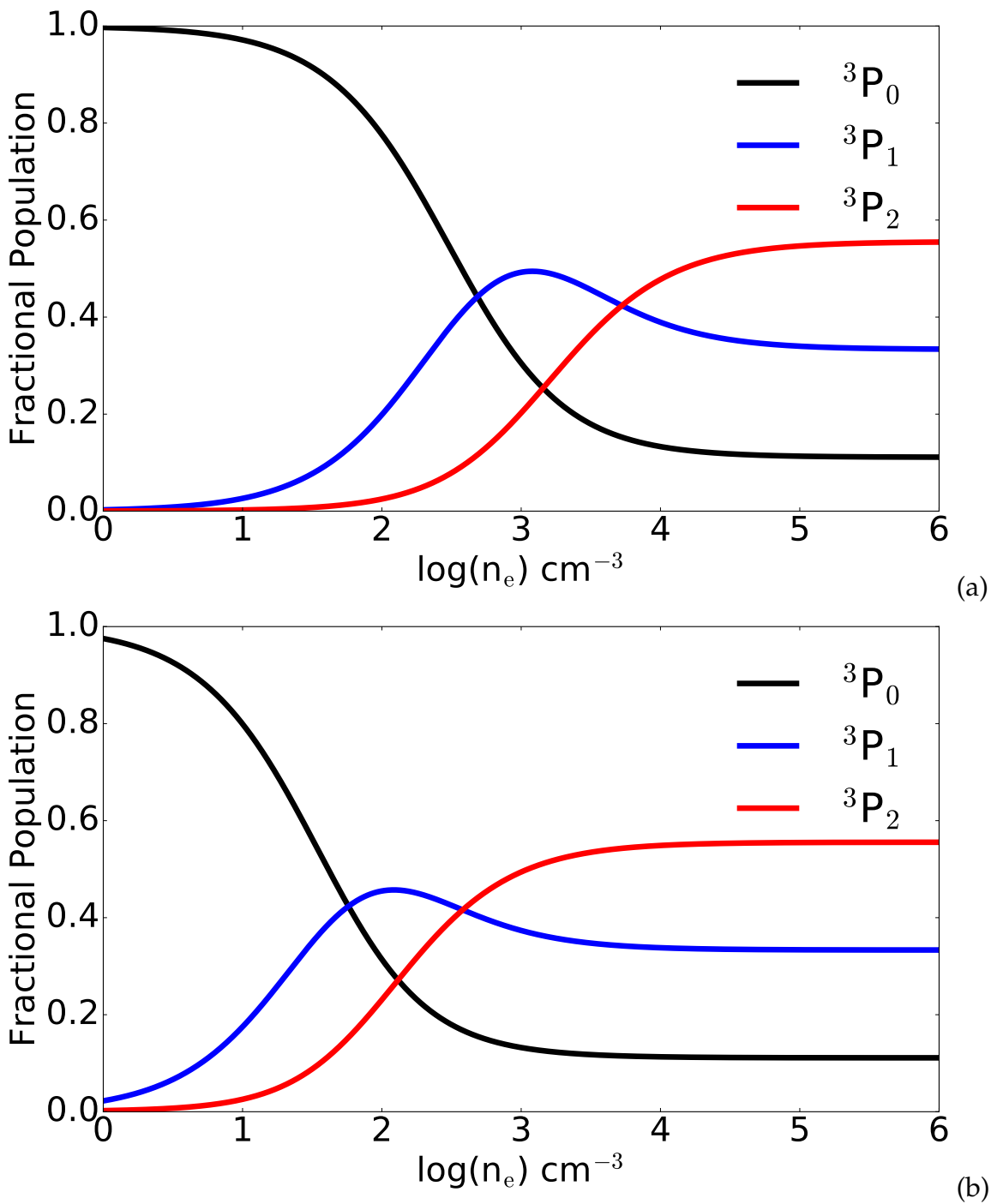


Figure 1.7 The fractional population in each of the three ground-state fine-structure energy levels as a function of electron density for the (a) O^{++} and (b) N^+ ions at $T_e = 10,000\text{K}$, using the collisional strengths of Palay et al. (2012) and Tayal (2011), respectively.

where

$$\epsilon_{ul} \equiv \frac{j_{ul}}{n_{total} n_e} \equiv \frac{h\nu_{ul}}{4\pi} \frac{n_u A_{ul}}{n_{total} n_e} = \frac{h\nu_{ul}}{4\pi} \frac{A_{ul}}{n_e} \frac{\frac{n_u}{n_2}}{1 + \frac{n_0}{n_2} + \frac{n_1}{n_2}} \text{ erg s}^{-1} \text{ cm}^3 \text{ sr}^{-1} \quad (1.10)$$

is the line emissivity (j_{ul}) normalized by the densities of both colliding species (the last equivalency holds specifically for three-level systems). A plot of this normalized emissivity can be seen in Figure 1.8 for the spectral lines associated with the O⁺⁺ and N⁺ ions. In this form, we can immediately see that the intensity ratio between the two radiative transitions for a three-level system is simply

$$\frac{I_{ul}}{I_{u'l'}} = \frac{\epsilon_{ul}}{\epsilon_{u'l'}} = \frac{\nu_{ul} n_u A_{ul}}{\nu_{u'l'} n_{u'} A_{u'l'}}, \quad (1.11)$$

which is primarily a function of electron density for the far-IR line-emitting ground-state terms. This is quite useful, since it implies that the intensity ratio between the two spectral lines of a three-level system yields the electron density within the emission region. Indeed, these ratios are leveraged in the case of the O⁺⁺ and N⁺ ions to determine the density of gas within ionized regions (see Figure 1.9).

1.4.2 Radio free-free emission and gas-phase metallicity

At this point, we note that, in the low-density limit, the line emissivity for the collisionally-excited transitions discussed above is proportional to the product

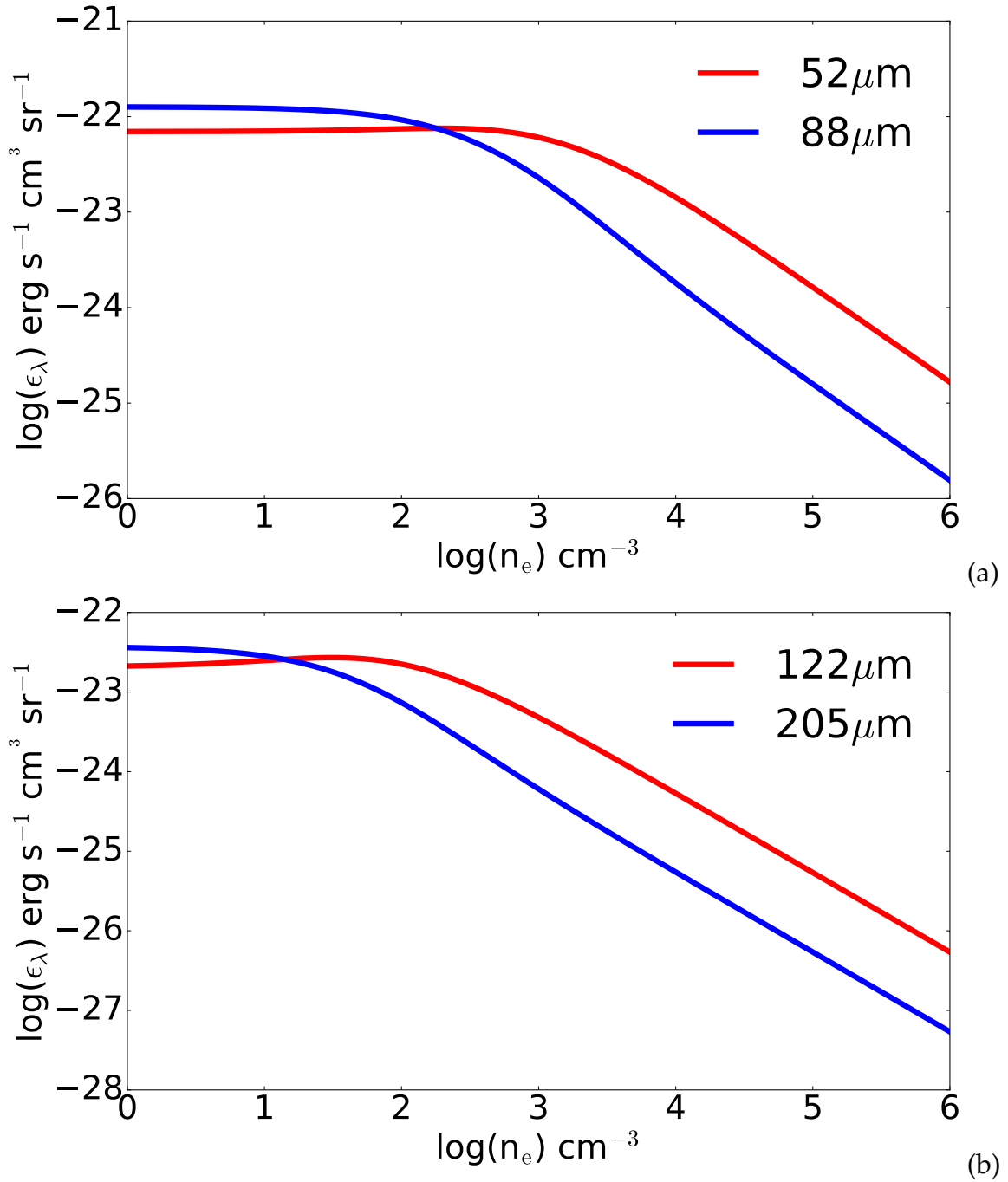


Figure 1.8 The normalized line emissivity (ϵ_λ) for the ground-state fine-structure transitions of the (a) O⁺⁺ and (b) N⁺ ions at $T_e = 10,000\text{K}$, calculated using the collisional strengths of Palay et al. (2012) and Tayal (2011), respectively.

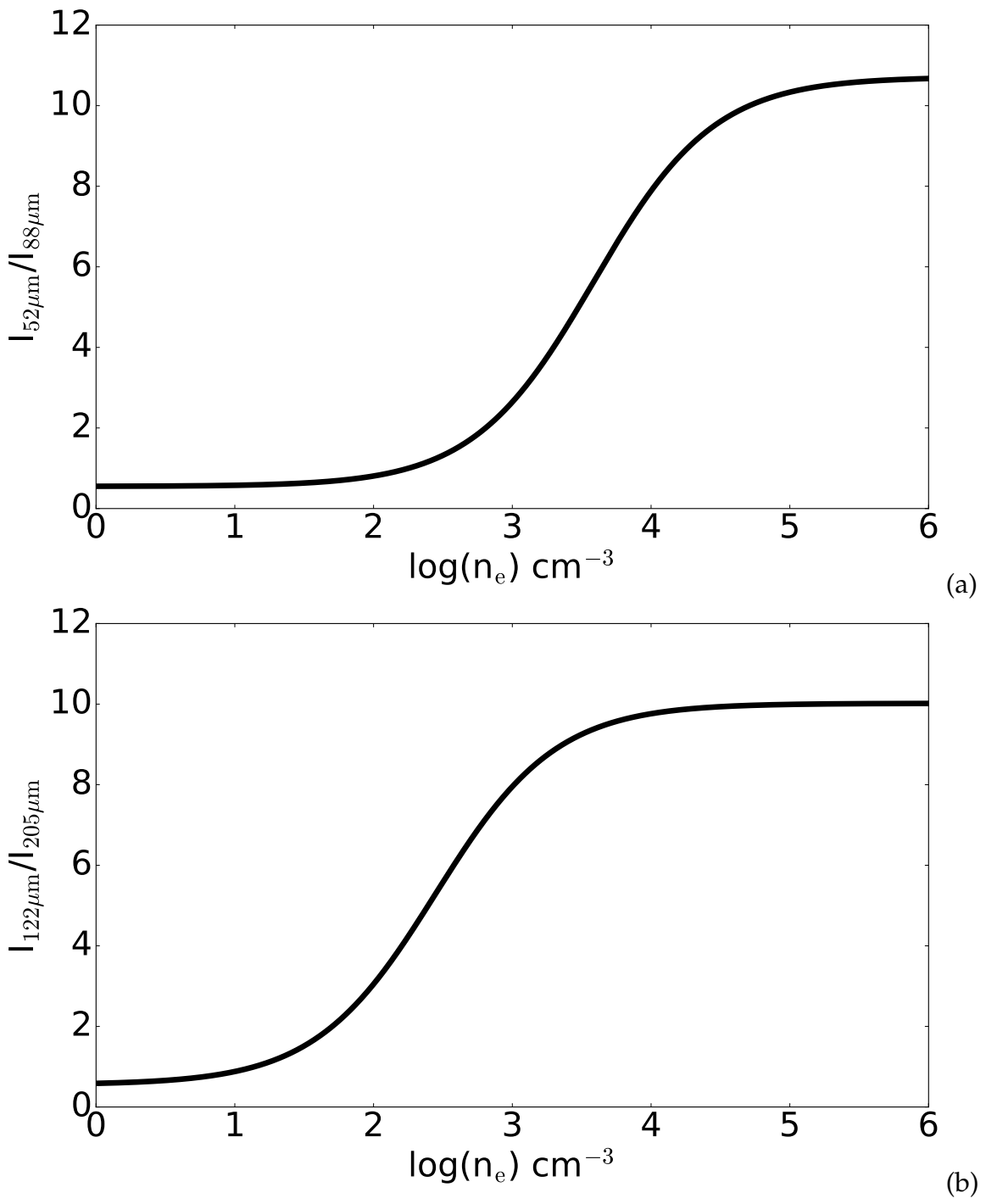


Figure 1.9 H II-region density can be determined by an intensity ratio of two spectral lines emitted by the same three-level ion, in this case the (a) O^{++} and (b) N^+ ions, assuming $T_e = 10,000K$, and using the collisional strengths of Palay et al. (2012) and Tayal (2011), respectively.

of the densities of the collisional partners, e.g. $j_{ul} \propto n_{ion} n_e$. Radio free-free emission, which is essentially just electron-proton scattering, has the property that $j_{ff} \propto n_p n_e$, thus allowing us to directly obtain absolute ionic abundances if we can measure both collisionally-excited line emission as well as radio free-free continuum emission.

It can be shown that the emissivity of radio free-free scattering is given by

$$j_{ff,\nu} = \frac{8}{3} \sqrt{\frac{2\pi m_e}{3kT}} \frac{Z^2 e^6}{m_e^2 c^3} n_{ion} n_e g(\nu, T) \exp\left(-\frac{h\nu}{kT}\right) \text{ erg s}^{-1} \text{ cm}^{-3} \text{ sr}^{-1} \text{ Hz}^{-1} \quad (1.12)$$

(e.g., [Spitzer, 1978](#)), where Z is the charge of the ions (primarily protons), e is the fundamental charge, c is the speed of light, m_e is the electron mass, T is the electron temperature, and $g(\nu, T)$ is the Gaunt factor, which differs from unity due to quantum mechanical effects. In the range $0.14 < Z \nu_9 T_4^{-1.5} < 250$, where ν_9 is the emission frequency in units of GHz and T_4 is the electron temperature within the ionized gas in units of 10,000 K, or essentially $0.14 \text{ GHz} < \nu < 250 \text{ GHz}$ for H II regions with $Z \sim T_4 \sim 1$, the emissivity can be approximated by

$$\begin{aligned} j_{ff,\nu} &\approx 3.35 \times 10^{-40} Z^2 n_{ion} n_e \nu_9^{-0.1} T_4^{-0.35} \\ &\approx 3.35 \times 10^{-40} n_p n_e \nu_9^{-0.1} T_4^{-0.35} \text{ erg s}^{-1} \text{ cm}^{-3} \text{ sr}^{-1} \text{ Hz}^{-1} \end{aligned} \quad (1.13)$$

(e.g., Draine, 2011). Then, the observed free-free flux density is given by:

$$S_{ff,\nu} = (4\pi j_{ff,\nu} D) 10^{23} \text{ Jy} \quad (1.14)$$

Taking the ratio of an observed collisionally-excited fine-structure line intensity with a radio free-free flux density yields the absolute abundance of the fine-structure-emitting species:

$$\frac{n_i}{n_p} = \frac{I_{ul}[\text{erg s}^{-1} \text{ cm}^{-2} \text{ sr}^{-1}]}{S_{ff,\nu}[\text{Jy}]} \frac{4.21 \times 10^{-16} T_4^{-0.35} \nu_9^{-0.1}}{\epsilon_{ul}[\text{erg s}^{-1} \text{ cm}^3 \text{ sr}^{-1}]} \left(\frac{n_e}{n_p} \right) \quad (1.15)$$

If the line-emitting species is an ion, the ionization state of the gas must be known in order to obtain a complete elemental abundance of the species in question. For example, if the [O III] 52 μm line is observed and compared to radio free-free emission, the O⁺⁺/O ratio within the ionized gas must be determined in order to obtain an O/H ratio from the computed O⁺⁺/H ratio.

1.4.3 Radiation field hardness

Observing spectral lines emitted by species with different ionization energies yields the hardness of the radiation field and hence reveals the properties of the sources of ionization. For H II regions heated by young stars, determining the hardness of the radiation field is equivalent to measuring the hottest star on the main sequence, or equivalently the age of the young stellar population.

Ideally, the hardness of the radiation field would be determined by observ-

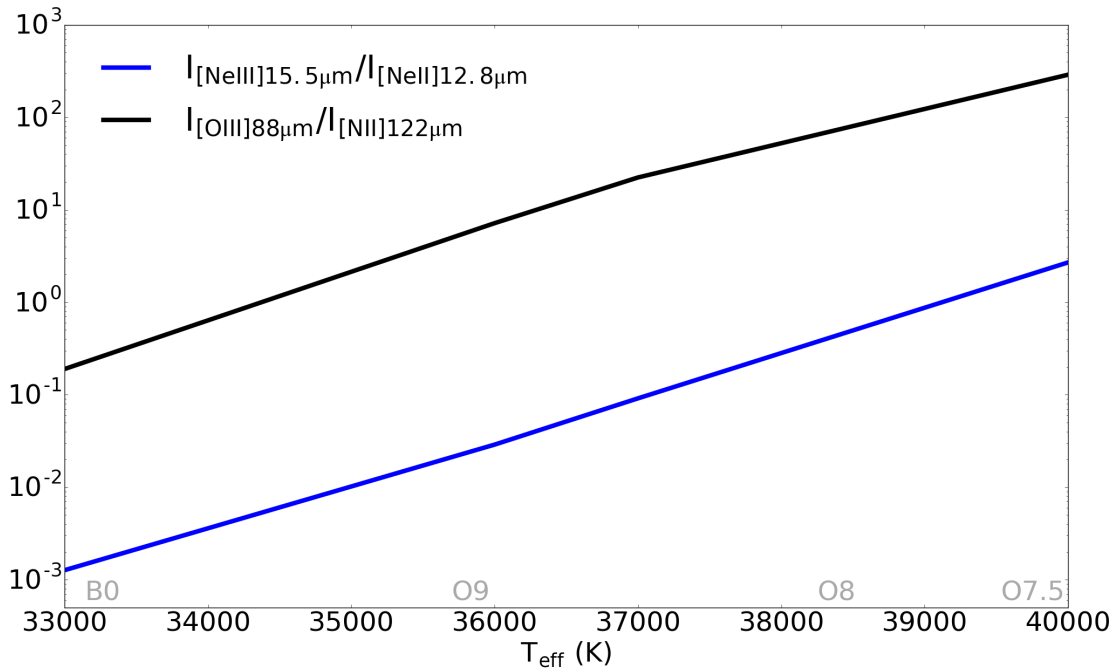


Figure 1.10 Ratios of spectral lines emitted by species with differing ionization potentials can be used to estimate the hardness of the UV radiation field. We plot the [Ne III]/[Ne II] (blue) and [O III]/[N II] (black) line-emission ratios as a function of effective stellar temperature and corresponding stellar type (adapted from the models of Rubin, 1985).

ing spectral lines of different ionization states of the same chemical element, such that differing abundance between elements does not enter into the determination. The best examples of these are line ratios of noble gas ionization states, e.g. Ne^{++} and Ne^+ , since noble gases will not, in general, be depleted onto grains. When observing multiple ionization states of the same element is not possible, however, a ratio between different emitting species of different ionization energies can also be used as a hardness indicator, e.g. O^{++} and N^+ , however variations in the intrinsic abundance ratios of the two elements may affect that determination (see Figure 1.10).

Thus, with observations of several FIR fine-structure lines, as well as radio free-free continuum emission, the density of the gas (and hence mass, since

these FIR transitions are optically thin), age of the young stellar population, and absolute gas-phase abundances can be determined within ionized gas regions, critical to understanding the evolution of star formation, and the buildup of metals, throughout cosmic time.

1.5 Neutral gas

The boundaries of H II regions are found where the hydrogen photo-ionization rates are reduced to the extent that most of the hydrogen will remain in the neutral phase. This boundary can be shown to be sharp – the H II region will go from nearly complete ionization to nearly completely neutral within the mean-free-path of a hydrogen-ionizing photon, or about 10^{-3} pc for ionized gas densities of $\sim 500 \text{ cm}^{-3}$. Photons with energies $< 13.6 \text{ eV}$ can escape the H II regions and heat the largely neutral gas regions beyond. These transitional zones between regions of ionized and molecular gas are called photo-dissociation regions (PDRs; so called because the molecular gas therein is dissociated by the flux of UV photons). In these regions, the dominant coolants of the gas are neutral oxygen (O^0) and singly-ionized carbon (C^+ ; formation energy 11.26 eV). These species are heated by photo-electrons ejected from poly-cyclic aromatic hydrocarbons (PAHs) and dust grains by the impinging far-ultraviolet (FUV) radiation field and cool the gas by line emission. Photon energies greater than about 6 eV are necessary to eject photo-electrons, so it is the FUV radiation field strength that is dominant for heating processes. Dust within these regions is heated by absorption of UV photons and cools by re-radiating the incident energy as FIR thermal continuum. Comparing the power output in line emission to that in thermal dust emission, then, yields the efficiency of photoelectric heat-

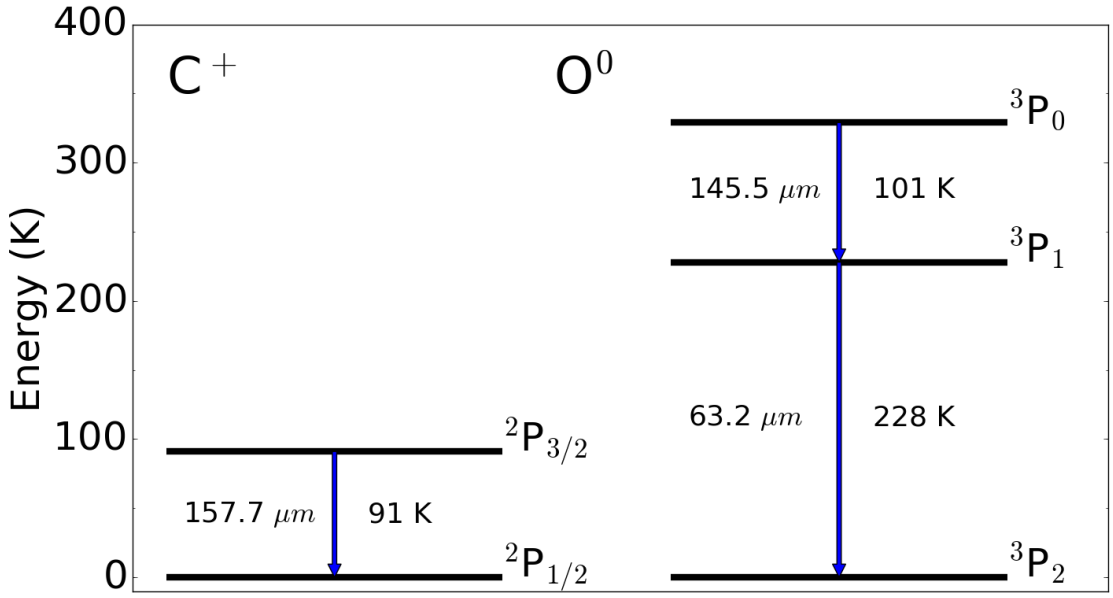


Figure 1.11 Energy level diagram showing the ground-state fine-structure splitting of the C^+ ion (left) and O^0 atom (right).

ing. Parametrizing the FUV radiation field ($6 \text{ eV} \leq h\nu \leq 13.6 \text{ eV}$) in units of the local (Habing) interstellar radiation field ($G = 1.6 \times 10^{-3} \text{ erg s}^{-1} \text{ cm}^{-2} \equiv 1$ Habing unit, e.g., [Kaufman et al., 2006](#)), the efficiency of photoelectric heating is sensitive to the ratio of the FUV field strength to the gas density, G_0/n .

1.5.1 Neutral gas tracers

The primary coolants of the gas within PDRs are two fine-structure transitions of neutral oxygen (at 63.18 and $145.53 \mu\text{m}$) and one of singly-ionized carbon (at $157.74 \mu\text{m}$; see Figure 1.11). The ground-state fine-structure splitting of the neutral oxygen atom gives rise to a three-level system, hence the two emission lines, which is well described by the equations presented for three-level systems in the section covering ionized gas. Detailed balance for the C^+ ion, a two-level

system in the optically-thin limit, is simply given by:

$$\begin{aligned} q_{10}n_1n_c + A_{10}n_1 &= q_{01}n_0n_c \\ n_0 + n_1 &= n_{total} \end{aligned} \tag{1.16}$$

such that the ratio of level populations is given by:

$$\frac{n_1}{n_0} = \frac{q_{01}n_c}{q_{10}n_c + A_{10}}. \tag{1.17}$$

Note that the collisional partner of the emitting species within PDRs is no longer electrons, which have recombined with protons, so we write n_c to refer generically to the number density of the collisional partner of the species in question. Then, as before,

$$\epsilon_{ul} \equiv \frac{j_{ul}}{n_{total}n_c} \equiv \frac{h\nu_{ul}}{4\pi} \frac{n_u A_{ul}}{n_{total}n_c} = \frac{h\nu_{10}}{4\pi} \frac{A_{10}}{n_c} \frac{1}{1 + \frac{n_0}{n_1}}, \tag{1.18}$$

$\text{erg s}^{-1} \text{cm}^3 \text{sr}^{-1}$

where the last equivalence holds specifically for two-level systems.

At this point, it is worth mentioning one caveat. Since the ionization energy of C⁺ (11.26 eV) is lower than that of hydrogen, it can exist in both regions of ionized and neutral gas. The fraction of line emission, then, emitted by the C⁺ ion in regions of ionized gas must be determined, and subtracted away, before employing any PDR modeling. Luckily, the N⁺ ion, which has an ionization energy of 14.53 eV and hence can only exist in regions of ionized gas, can be

used to tease out that contribution. The lower-lying ground-state fine-structure transition of the N⁺ ion, at 205.18 μm , and the only ground-state fine-structure transition of the C⁺ ion, at 157.74 μm , have nearly identical critical densities in regions of ionized gas (48 and 50 cm^{-3} , respectively), such that the intensity ratio of these two emission lines is nearly constant in H II regions, regardless of gas density (e.g., Oberst et al., 2006, see Figure 1.12). Any [C II] 158 μm line emission seen in excess of the standard ratio can be attributed to a PDR origin.

Once the contribution to the [C II] 158 μm line originating within PDRs is known, it can be compared to other gas-cooling lines, of neutral oxygen for example, as well as to the FIR thermal dust continuum emission, to determine the gas density, surface temperature, and incident FUV radiation field strength. These values are necessary for calculating the gas mass contained within, as well as the physical extent of, PDRs (see Figure 1.13).

1.5.2 Gas mass from optically-thin tracers

The neutral hydrogen gas mass within PDRs can be calculated from the [C II] 158 μm line luminosity in the optically-thin limit. Recall that the line emissivity (j , in units of $\text{erg s}^{-1} \text{cm}^{-3} \text{sr}^{-1}$) is related to the total luminosity produced within a volume (V) by:

$$L = 4\pi jV, \quad (1.19)$$

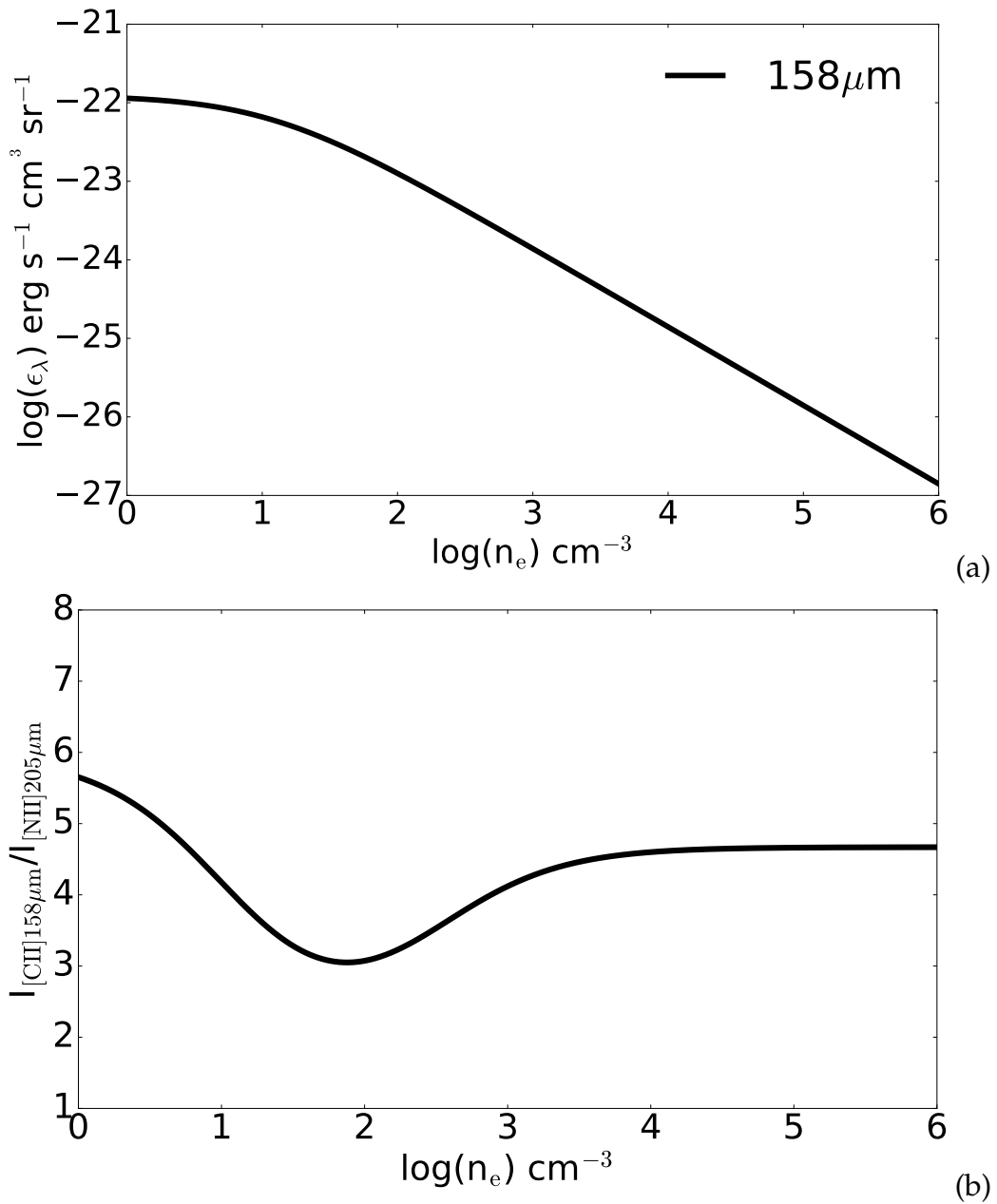


Figure 1.12 (a) The normalized line emissivity (ϵ_λ) for the $158 \mu\text{m}$ transition of the C^+ ion in regions of ionized gas at $T_e = 10,000 \text{ K}$, calculated using the collisional strengths of Hayes & Nussbaumer (1984). (b) The $[\text{C II}] 158 \mu\text{m}/[\text{N II}] 205 \mu\text{m}$ intensity ratio in ionized-gas regions, adopting the gas-phase carbon and nitrogen abundances of Savage & Sembach (1996) and assuming an ionization state such that $n_{\text{C}^+}/n_{\text{C}_{\text{total}}} = n_{\text{N}^+}/n_{\text{N}_{\text{total}}}$ (see, e.g., Oberst et al., 2006).

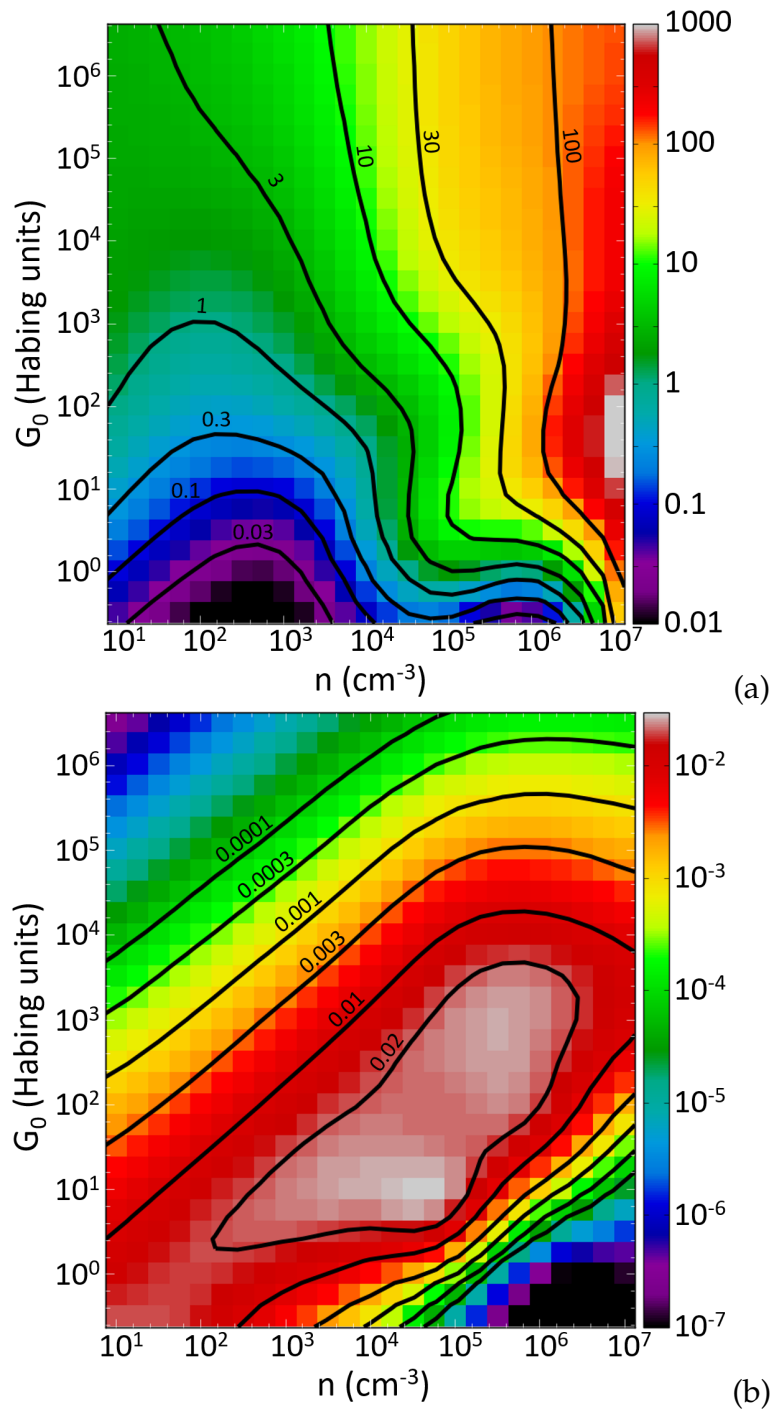


Figure 1.13 PDR models showing the variation in (a) $[\text{O I}]/[\text{C II}]$ and (b) $([\text{O I}] + [\text{C II}])/\text{FIR}$ with changing G_0 and n . Reproduced using the models of Pound & Wolfire (2008) and Kaufman et al. (2006).

or in terms of the density-normalized emissivity (ϵ) defined above,

$$L = 4\pi\epsilon n_{C^+} n_H V, \quad (1.20)$$

where here we take neutral hydrogen to be the collisional partner of the C^+ ion. The total mass of neutral hydrogen is then related to the mass of the hydrogen atom (m_H) and gas density (n_H) by:

$$M_{H,neutral} = m_H n_H V, \quad (1.21)$$

which is related to the line luminosity by:

$$L = 4\pi\epsilon n_{C^+} n_H \frac{M_{H,neutral}}{m_H n_H}, \quad (1.22)$$

where

$$\epsilon_{ul} = \frac{h\nu_{ul}}{4\pi} \frac{n_u A_{ul}}{n_{total} n_c} = \frac{h\nu_{10}}{4\pi} \frac{A_{10}}{n_c} \frac{1}{1 + \frac{n_0}{n_1}}, \quad (1.23)$$

the last equivalency being specifically for a two-level system, which accurately describes the C^+ ion. Combining all of this, we get:

$$L = 4\pi \frac{h\nu_{10}}{4\pi} \frac{A_{10}}{n_H} \frac{1}{1 + \frac{n_0}{n_1}} n_{C^+} n_H \frac{M_{H,neutral}}{m_H n_H}. \quad (1.24)$$

Simplifying and solving this equation for the neutral-hydrogen mass, and recasting everything in more useful astronomical units, we obtain:

$$\left(\frac{M_{H,neutral}}{M_\odot} \right) = 0.876 \left(\frac{L_{[CII]}}{L_\odot} \right) \left(1 + \frac{n_0}{n_1} \right) \left(\frac{1.4 \times 10^{-4}}{X_{C^+}} \right), \quad (1.25)$$

where

$$X_{C^+} \equiv \frac{n_{C^+}}{n_H} \quad (1.26)$$

taken here to be 1.4×10^{-4} (Savage & Sembach, 1996). The ratio of the level populations for the two-level system describing the C^+ ion can be written in a more tractable way:

$$1 + \frac{n_0}{n_1} = 1 + \frac{q_{10}n_H + A_{10}}{q_{01}n_H} \quad (1.27)$$

where, making a common fraction and dividing the numerator and denominator by $q_{10}n_H$, we obtain:

$$1 + \frac{n_0}{n_1} = \frac{\frac{q_{01}}{q_{10}} + 1 + \frac{A_{10}}{q_{10}n_H}}{\frac{q_{01}}{q_{10}}}. \quad (1.28)$$

We then recall that

$$\frac{q_{01}}{q_{10}} = \frac{g_1}{g_0} \exp \left(\frac{-T_{10}}{T_{gas}} \right) = 2 \exp \left(\frac{-91K}{T_{gas}} \right), \quad (1.29)$$

where the last equivalence holds specifically for the [C II] 158 μm transition, and that the critical density (n_{crit}) is defined to be the density at which the rate of collisional deexcitations balance that of radiative deexcitations, which for the two-level [C II] emitting configuration reduces to:

$$n_{crit} \equiv \frac{A_{10}}{q_{10}}. \quad (1.30)$$

$n_{crit} \sim 2,800 \text{ cm}^{-3}$ in regions of neutral hydrogen for the [C II] 158 μm line (Stacey, 2011). This simplifies our equation for neutral-gas mass from the [C II] 158 μm line:

$$\left(\frac{M_{H,neutral}}{M_\odot} \right) = 0.876 \left(\frac{L_{[CII]}}{L_\odot} \right) \left(\frac{1 + 2 \exp \left(\frac{-91K}{T_{gas}} \right) + \frac{n_{crit}}{n_H}}{2 \exp \left(\frac{-91K}{T_{gas}} \right)} \right) \left(\frac{1.4 \times 10^{-4}}{X_{C^+}} \right). \quad (1.31)$$

where the density and gas temperature can be determined by PDR modeling (e.g., Kaufman et al., 2006, Pound & Wolfire, 2008).

The extent to which PDRs, and hence star-forming regions, are extended over a galaxy can be estimated simply. Once the FUV radiation field strength is determined from modeling, and employing the assumption that the majority of the FUV continuum is absorbed by dust and re-radiated as FIR continuum, the ratio of the FIR continuum luminosity to the FUV field strength yields the

extent of the PDRs (e.g., Stacey et al., 1991, Wolfire et al., 1990):

$$R_{PDRs} \sim \left(\frac{L_{FIR}[\text{erg s}^{-1}]}{G_0[\text{erg s}^{-1} \text{cm}^{-2}]} \right)^{\frac{1}{2}}. \quad (1.32)$$

1.6 Molecular gas

Inventorying molecular gas, the fuel for star formation within galaxies, is crucial to our understanding of the evolution of star formation through cosmic time. It is complicated, however, by the fact that hydrogen, whose lowest rotational transition takes ~ 500 K to excite, is difficult to observe in cold molecular clouds. To circumvent this problem, the easily-excited low-J rotational levels of carbon-monoxide (CO) are generally used as a proxy for molecular gas content. Here we briefly detail the ways in which CO observations, as well as thermal dust continuum observations, can be used to infer the total molecular gas mass within galaxies, as well as some of the shortcomings of these indirect methods.

1.6.1 CO

Given that CO is a fairly abundant molecule ($n_{CO}/n_{H_2} \sim 10^{-4}$) whose asymmetry and molecular mass give it a permanent dipole moment with an easily-excited fundamental rotational mode that exists in the millimeter bands, it is a natural candidate to be used as a gas-mass proxy. Recalling that the energy of a quantum rigid rotator is proportional to the square of its quantized angular momentum, $E_J \propto L_J^2 \propto J(J+1)$, the energy difference between adjacent rotational

states, and hence the energy of the photons corresponding to the transitions between those states, is given by multiples of the fundamental frequency of the system. For the CO molecule, the fundamental frequency, corresponding to the transition between the $J = 1$ and $J = 0$ states, is 115.27 GHz. This is perfect for probing the cold gas within molecular clouds ($\sim 10 - 20$ K), since the energies above ground of the $J = 1$ and $J = 2$ states are ~ 5 K and ~ 15 K, respectively, such that these states are populated, and hence radiate, within molecular clouds.

In terms of the observed line flux, the CO luminosity can be calculated using the following equation:

$$L_{\text{CO}} = 1.04 \times 10^{-3} S_{\text{CO}} \Delta v \nu_{\text{rest}} (1+z)^{-1} D_L^2 \quad (1.33)$$

L_{\odot}

where $S_{\text{CO}} \Delta v$ is the velocity-integrated line flux in Jy km s⁻¹, related to the standard line flux by

$$F[\text{W m}^{-2}] = \frac{10^{-23} S_{\text{CO}} \Delta v [\text{Jy km s}^{-1}]}{\lambda_{\text{obs}} [\text{m}]} \quad (1.34)$$

ν_{rest} is the rest-frequency of the line in GHz, D_L is the luminosity distance in Mpc, and z is the redshift of the source. Equivalently, the CO luminosity can be written in the following form (e.g., [Solomon & Vanden Bout, 2005](#)):

$$L'_{\text{CO}} = 3.25 \times 10^7 S_{\text{CO}} \Delta v \nu_{\text{obs}}^{-2} (1+z)^{-3} D_L^2, \quad (1.35)$$

$\text{K km s}^{-1} \text{ pc}^2$

where all quantities are as in the previous equation. This form of the luminosity has the advantage of being proportional to the brightness temperature T_b , since $L'_{CO} \propto L_{CO}/\nu^3$, such that the ratio between different CO rotational transitions is unity if the CO-emitting gas is fully thermalized. This is particularly useful for constructing CO spectral line energy distributions (SLEDs), measured CO-line fluxes as a function of transition, which reveal the molecular-gas density and temperature and hence can point to the sources of gas heating (e.g., recent star formation or AGN activity).

The CO luminosity is then used to estimate the molecular-hydrogen mass by way of a scaling relation (e.g., [Bolatto et al., 2013](#)):

$$M_{H_2} = \alpha_{CO} L'_{CO}, \quad (1.36)$$

$$\text{M}_\odot$$

where α_{CO} , in units of $\text{M}_\odot (\text{K km s}^{-1} \text{ pc}^2)^{-1}$, is the linear conversion factor between CO luminosity and molecular-gas mass. A quick note is warranted here about why this scaling relation works: in both the ionized- and neutral-gas sections above, we considered optically-thin line-emission, which emanates from a volume, such that the mass of the entire emitting volume is probed. CO emission, however, is not optically thin, such that it does not probe a volume but rather a surface. This apparent problem is circumvented by noting that, for virialized molecular clouds, the molecular-gas mass (M_{gas}) is related to the velocity dispersion (σ) and radius of the cloud (R) by $M_{gas} \propto \sigma^2 R$. It was also found empirically by [Larson \(1981\)](#) that giant molecular clouds exhibit a scaling relation between their linewidths and radii, such that $\sigma \propto R^{1/2}$. Combining these two relations implies that $M_{gas} \propto R^2 \propto \sigma^4$. And $L'_{CO} \propto T_b \sigma R^2$, such that

$L'_{CO} \propto T_b \sigma^5$, which implies that $M_{gas} \propto T_b^{-0.8} L'^{0.8}_{CO}$, and thus molecular-gas mass scales nearly linearly with observed CO-line luminosity, at a given brightness temperature.

While this linear scaling between molecular-gas mass and CO luminosity is a useful estimator for gas mass, there is a large caveat here. It is well known that the α_{CO} conversion factor varies from galaxy to galaxy, from a value of $\sim 0.8 M_\odot (K \text{ km s}^{-1} \text{ pc}^2)^{-1}$ in nearby ultra-luminous infrared galaxies (ULIRGs) to a value of $\sim 4.3 M_\odot (K \text{ km s}^{-1} \text{ pc}^2)^{-1}$ in the Milky Way, to much higher values in dwarf galaxies. This variation can arise from variations in gas excitation, as for ULIRGs where the extreme star-formation can heat the gas, which would clearly reflect the conversion factor as outlined above. In addition, changes in metallicity can affect the conversion factor. Molecular hydrogen is self-shielding whereas CO molecules depend on a column of dust to extinct the photons which would otherwise dissociate them. Since the dust-to-gas ratio scales with metallicity (e.g., Rémy-Ruyer et al., 2014), so too does the penetration depth of CO-dissociating photons into molecular clouds. At lower metallicity, and hence lower dust-to-gas ratio, the CO-emitting cores of molecular clouds retreat toward the center of the clouds, as CO-dissociating photons penetrate deeper. Meanwhile, the molecular hydrogen, which is self-shielding, is less affected. This makes the α_{CO} conversion factor much higher in low-metallicity sources, where CO becomes a poor tracer of molecular hydrogen and hence the conversion factor must be boosted to compensate (e.g., Bolatto et al., 2013, see Figure 1.14). These effects were first modeled theoretically by Maloney & Black (1988), and first confirmed observationally through [C II] observations of the 30 D-radius region of the Large Magellanic Cloud (LMC) in Stacey et al. (1991).

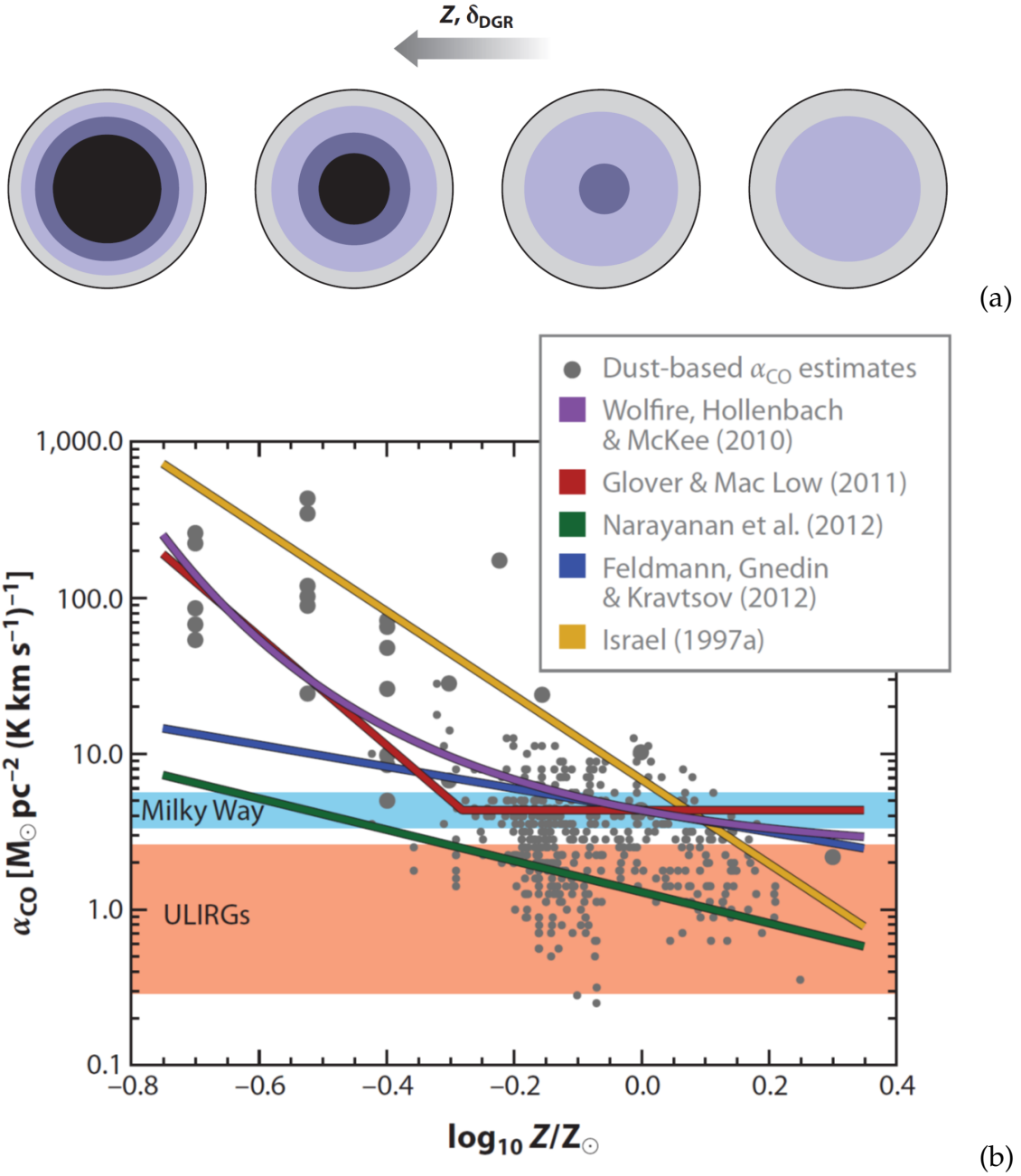


Figure 1.14 (a) As the metallicity, or equivalently the dust-to-gas ratio, of the ISM decreases (moving left to right), the CO-emitting core of the molecular cloud (dark purple) shrinks and the α_{CO} parameter must necessarily be boosted to compensate, as shown in (b). Reproduced from Bolatto et al. (2013).

1.6.2 Thermal dust continuum

In addition to using CO measurements, the molecular-gas mass contained within a galaxy can be estimated using observations of the FIR thermal dust continuum. This method is particularly useful, since continuum observations are often easier observationally than the alternative CO spectroscopic observations, however it does have its own drawbacks.

Dust on the Rayleigh-Jean's tail of the blackbody function is optically thin, such that a continuum flux measurement at sufficiently long wavelength yields the dust mass. Then, a dust-to-gas ratio can be adopted to arrive at the total molecular-gas mass. Here we illustrate this method, following [Scoville et al. \(2016\)](#):

Consider continuum emission from a thermal blackbody, dust in this case, at temperature T_d :

$$S_{\nu_{obs}} = \frac{(1 - e^{-\tau_d(\nu_{rest})})B_{\nu_{rest}}(T_d)(1 + z)}{d_L^2}, \quad (1.37)$$

where $S_{\nu_{obs}}$ is the flux density at observed frequency ν_{obs} , $\tau_d(\nu)$ is the dust optical depth, given by $\tau_d(\nu) = 1.36\kappa(\nu)N_H m_H = \kappa(\nu)M_{gas}$, where $\kappa(\nu)$ is the absorption coefficient per unit total mass of gas (effective area per unit gas mass), N_H is the hydrogen column density, m_H is the mass of the hydrogen atom, the factor of 1.36 accounts for species other than hydrogen (primarily helium), $B_\nu(T_d)$ is the blackbody function evaluated at temperature T_d , z is the source redshift, and d_L is the luminosity distance.

The dust is optically thin at long wavelength, simplifying the equation:

$$S_{\nu_{obs}} = \frac{M_{gas}\kappa(\nu_{rest})B_{\nu_{rest}}(T_d)(1+z)}{d_L^2}. \quad (1.38)$$

The expression can be further simplified by replacing the full form of $B_\nu(T_d)$ with the Rayleigh-Jean's approximation:

$$S_{\nu_{obs}} = \frac{M_{gas}\kappa(\nu_{rest})(1+z)}{d_L^2} \frac{2kT_d\nu_{rest}^2}{c^2} \Gamma_{RJ}(T_d, \nu_{obs}, z), \quad (1.39)$$

where $\Gamma_{RJ}(T_d, \nu_{obs}, z)$ is the departure from the Rayleigh-Jean's tail, i.e.,

$$\Gamma_{RJ}(T_d, \nu_{obs}, z) \equiv \frac{B_{\nu_{rest}}}{RJ_{rest}} = \frac{h\nu_{obs}(1+z)}{kT_d} \frac{1}{e^{h\nu_{obs}(1+z)/kT_d} - 1}, \quad (1.40)$$

where k and h are the Boltzmann and Planck constants, respectively. The flux density can be recast as a luminosity in the rest-frame of the galaxy by:

$$L_{\nu_{rest}} = \frac{S_{\nu_{obs}} 4\pi d_L^2}{(1+z)} = M_{gas}\kappa(\nu_{rest}) \frac{8\pi k T_d \nu_{rest}^2}{c^2} \Gamma_{RJ}(T_d, \nu_{obs}, z). \quad (1.41)$$

At long wavelength, dust opacity is well approximated by a power law in wavelength, here anchored at 850 μm ,

$$\kappa(\nu) = \kappa(\nu_{850\mu\text{m}}) \left(\frac{\lambda}{850\mu\text{m}} \right)^{-\beta}, \quad (1.42)$$

with $\beta \sim 1.8$.

The rest-frame luminosity-to-gas-mass ratio at $850 \mu\text{m}$ ($\alpha_{\nu_{850\mu\text{m}}}$) is given by:

$$\frac{L_{\nu_{850\mu\text{m}}}}{M_{\text{gas}}} = \kappa(\nu_{850\mu\text{m}}) \frac{8\pi k \nu_{850\mu\text{m}}^2}{c^2} T_d \Gamma_{RJ} \equiv \alpha_{\nu_{850\mu\text{m}}}. \quad (1.43)$$

[Scoville et al. \(2016\)](#) measure an average value of $\alpha_{\nu_{850\mu\text{m}}} = (6.7 \pm 1.7) \times 10^{19} \text{ erg s}^{-1} \text{ Hz}^{-1} \text{ M}_\odot^{-1}$ in a sample containing local star-forming galaxies, ultra-luminous infrared galaxies (ULIRGs), and sub-millimeter galaxies (SMGs). We can estimate the rest-frame $850 \mu\text{m}$ luminosity from the observed flux density at a different wavelength by marching up or down the Rayleigh-Jean's tail of the modified blackbody:

$$L_{\nu_{850\mu\text{m}}} = 1.19 \times 10^{27} S_\nu [\text{Jy}] \left(\frac{\nu_{850\mu\text{m}}}{\nu_{\text{obs}}(1+z)} \right)^{3.8} \frac{(d_L[\text{Mpc}])^2}{1+z} \frac{\Gamma_0}{\Gamma_{RJ}}, \quad (1.44)$$

$\text{erg s}^{-1} \text{ Hz}^{-1}$

where

$$\frac{\Gamma_0}{\Gamma_{RJ}} \equiv \frac{\Gamma_{RJ}(T_d, \nu_{850\mu\text{m}}, z=0)}{\Gamma_{RJ}(T_d, \nu_{\text{obs}}, z)}. \quad (1.45)$$

Combining equations 1.39 and 1.44, and adopting a fiducial dust temperature (T_d) of 25 K, as in [Scoville et al. \(2016\)](#), we arrive at the relation between

observed flux density and molecular-gas mass:

$$M_{gas} = 1.78 S_{\nu_{obs}} [mJy] (1+z)^{-4.8} \left(\frac{\nu_{850\mu m}}{\nu_{obs}} \right)^{3.8} (d_L [Gpc])^2 \left(\frac{6.7 \times 10^{19}}{\alpha_{\nu_{850\mu m}}} \right) \left(\frac{25K}{T_d} \right) \frac{\Gamma_0}{\Gamma_{RJ}} 10^{10} M_\odot. \quad (1.46)$$

Thus, the molecular-gas mass determined using this method depends on $\alpha_{\nu_{850\mu m}}$, essentially a dust-to-gas ratio, and the temperature of the dust, meaning that this determination is dependent on the metallicity of the source. It is, therefore, critically important to have some constraints on the metallicity of a galaxy before blindly applying either this method or the CO-based method that we described above.

1.7 Telescopes

Over the past few decades, the technology required to conduct observations in the far-infrared and sub-millimeter bands has matured significantly. Here we briefly describe two of the observatories crucial in obtaining the observations presented in this thesis: the Atacama Large (sub-)Millimeter Array (ALMA) and the *Herschel Space Observatory*.

1.7.1 ALMA

The Atacama Large (sub-)Millimeter Array (ALMA) is an interferometer consisting of 50 – 12 m antennas, located in the Atacama Desert of Chile. It currently

conducts observations in 8 atmospheric windows situated between $\sim 350\,\mu\text{m}$ and $\sim 3\,\text{mm}$. With baselines spanning up to $\sim 14\,\text{km}$ in some observing bands, the array can achieve an angular resolution of $\sim 42\,\text{mas}$ at $3\,\text{mm}$, $12\,\text{mas}$ at $850\,\mu\text{m}$, and $24\,\text{mas}$ at $350\,\mu\text{m}$. While such high-angular-resolution observations of high-redshift galaxies are not generally feasible, we are able to observe FIR fine-structure lines of carbon, oxygen, and nitrogen, at redshift $\sim 1 - 2$ in the 350 and $450\,\mu\text{m}$ atmospheric windows, as well as CO transitions in longer wavelength bands, at kiloparsec resolution.

1.7.2 Herschel

The *Herschel Space Observatory* was a space-based observatory, operating in the FIR bands. The *Photodetector Array Camera and Spectrometer (PACS)* was composed of two sub-instruments: an imaging photometer, with bands centered at 70 , 100 , and $160\,\mu\text{m}$, and a two-camera integral-field spectrograph, capable of obtaining spectra over the range $\sim 50 - 210\,\mu\text{m}$. The *Spectral and Photometric Imaging Receiver (SPIRE)* instrument was similarly composed of two sub-instruments: an imaging photometer, with bands centered at 250 , 350 , and $500\,\mu\text{m}$, and a two-band imaging Fourier-Transform Spectrometer (FTS), covering $194 - 318\,\mu\text{m}$ and $294 - 671\,\mu\text{m}$. This observatory enabled the study of FIR fine-structure lines in nearby galaxies, impossible to observe from the ground due to water vapor in Earth's atmosphere, as well as in high-redshift galaxies.

1.8 Overview of thesis

The work presented in this thesis focuses on multi-band observations of two galaxies situated within the peak epoch of cosmic star formation, though the techniques employed here can be applied to studying star-forming galaxies more broadly.

In chapter 2, we present observations of several far-infrared fine-structure lines from both ionized and neutral gas, as well as CO observations from molecular gas, in 3C 368, a well-studied radio-galaxy at $z = 1.131$. These new observations suggest a powerful active galactic nucleus (AGN), accompanied by vigorous and extended star formation. The estimated age of the starburst makes it nearly concurrent with the latest episode of AGN flaring, suggesting a link between the growth of the supermassive black hole and stellar population in this source. We do not detect CO emission in 3C 368, consistent with recent star-formation activity if the star-forming molecular gas has low metallicity, is highly fractionated (such that CO is photodissociated through much of the clouds), or is chemically very young (such that CO has not yet had time to form).

In chapter 3, we investigate the properties of the interstellar medium, star formation, and the current-day stellar population in the gravitationally-lensed star-forming galaxy SDP.11, at $z = 1.7830$. We map the [C II] $158\,\mu\text{m}$ line emission, using ALMA, at $0''.2$ resolution. The values seen in the [C II]/FIR ratio map are similar to those of local starburst galaxies, suggesting intense star-formation in this source. By applying gravitational-lens models, we find that the lensing magnification factor varies by a factor of two across SDP.11, affecting the observed line profiles. After correcting for the effects of differential lensing, a

symmetric line-profile is recovered, suggesting that the starburst present here is extended over a 3-5 kpc rotating disk, in contrast to local ULIRGS, suggesting that it may not be the result of a major merger.

In chapter 4 we return to 3C 368, having detected spectral lines which trace both the molecular (CO) and neutral (C^0) phases of the ISM. These observations allow us to inventory the molecular-gas reservoirs, the fuel for star formation, by applying independent methods based on emission from CO, [C I], and thermal dust. We also present gas-phase metallicity estimates in this source, both using far-infrared (FIR) fine-structure lines together with radio free-free continuum emission and independently employing the optical R_{23} method. Both methods agree on a sub-solar gas-phase metallicity of $\sim 0.3 Z_\odot$. Intriguingly, comparing the molecular-gas mass estimated using this sub-solar metallicity to dust-mass estimates from multi-component spectral energy distribution (SED) modeling yields a gas-to-dust ratio within $\sim 15\%$ of the accepted value for a metallicity of $0.3 Z_\odot$. This gas mass puts 3C 368 on par with other galaxies at $z \sim 1$ in terms of specific star formation rate and gas fraction. We suggest that perhaps 3C 368 is accreting pristine molecular gas from an external source, thereby diluting its gas-phase metallicity.

Finally, in chapter 5 we summarize the work presented here and discuss the future direction of this research.

CHAPTER 2

CO-DARK STAR FORMATION AND BLACK HOLE ACTIVITY IN 3C 368

AT $z = 1.131$: COEVAL GROWTH OF STELLAR AND SUPERMASSIVE

BLACK HOLE MASSES

C. Lamarche, G. J. Stacey, D. Brisbin, C. Ferkinhoff, S. Hailey-Dunsheath, T. Nikola,

D. Riechers, C. E. Sharon, H. Spoon, A. Vishwas

The Astrophysical Journal, 836:123, 2017

2.1 Introduction

A major goal in the study of galaxy evolution is understanding the interplay between active galactic nuclei (AGN) and star formation in their host galaxies. A correlation exists between the mass of central black holes, which power AGN, and stellar bulge mass, which suggests that the growth of black holes by accretion is linked to the growth of stellar mass by star formation (e.g., Ferrarese & Merritt, 2000). Gas accretion onto a central black hole can spur AGN activity, including winds and high-energy radiation, which may disrupt the ISM of the host galaxy, quenching star formation (e.g., Sanders et al., 1988). On the other hand, AGN activity through jets and winds, for example, can contribute an additional pressure to the interstellar medium (ISM) of the host galaxy, leading to cloud collapse, and thereby bolstering star formation (both theoretically and observationally, e.g. Croft et al., 2006, Dey et al., 1997, Gaibler et al., 2012, Silk, 2013). Here we investigate the relationship between star formation and AGN activity in the bright radio galaxy 3C 368 at redshift $z = 1.131$ (as determined by the [O II] 372.8 nm line, Meisenheimer & Hippelein, 1992). We observe 3C 368

as it was in the epoch of both peak star formation and AGN activity in the Universe.

3C 368 was discovered as part of the Third Cambridge Radio Catalog (Edge et al., 1959). Since then, it has become one of the best studied, high-redshift, radio-loud, Fanaroff-Riley class II (FR-II) type galaxies, with observations spanning the electromagnetic spectrum from the radio (e.g., Best et al., 1998a) to the X-Ray (e.g., Crawford & Fabian, 1995).

Not only does it exhibit considerable AGN activity, with radio emission extended over 73 kpc (Best et al., 1998a), 3C 368 also has a substantial stellar mass ($\sim 3.6 \times 10^{11} M_{\odot}$, Best et al., 1998b), and is undergoing a period of vigorous ($350 M_{\odot} \text{ yr}^{-1}$, calculated by spectral energy distribution (SED) modeling in the far-infrared, Podigachoski et al., 2015) and extended (over $\sim 2\text{--}4$ kpc, Stacey et al., 2010b) star formation. McCarthy et al. (1987) suggested a link between AGN activity and star formation in this source, in that the jets emanating from the AGN seem to be spurring star formation. To date, however, no CO emission, which traces the molecular gas necessary for star formation, has been detected in this source (e.g., Evans et al., 1996).

To further explore the properties of the stellar population in 3C 368, including its age and spatial distribution, we observed the [O I] $63 \mu\text{m}$ line, the [O III] 52 and $88 \mu\text{m}$ lines, and the [O IV] $26 \mu\text{m}$ line using the *PACS* spectrometer on the *Herschel Space Observatory*, the [N II] $205 \mu\text{m}$ line with the Atacama Large Millimeter/submillimeter Array (ALMA), and the CO(2–1) line using both ALMA and the Plateau de Bure Interferometer (PdBI). The [O I] line arises from dense photodissociated gas on the surfaces of molecular clouds, and combined with our prior detection of the [C II] $158 \mu\text{m}$ line with ZEUS on the Caltech Submil-

limeter Observatory (CSO) (Stacey et al., 2010b), traces the strength of the UV radiation field. The [O III] 52 and 88 μm lines taken together allow us to estimate the density within H II regions, and the [O IV] 26 μm line, with an ionization potential of 54.93 eV, traces the narrow line region (NLR) of the AGN.

Taken together with spectroscopic observations conducted with the *Infrared Spectrograph* (IRS) on board the *Spitzer Space Telescope*, including [Ne II] and [Ne III] lines in the mid-infrared, these new data allow us to estimate the age of the starburst in 3C 368, furthering the theory of AGN-driven star formation in this powerful, yet enigmatic, galaxy.

We assume a flat Λ CDM cosmology, with $\Omega_M = 0.27$, $\Omega_\Lambda = 0.73$, and $H_0 = 71 \text{ km s}^{-1} \text{ Mpc}^{-1}$, throughout this paper (Spergel et al., 2003).

2.2 Observations

2.2.1 Herschel/PACS

The oxygen fine-structure lines were observed in 3C 368 using the *Photodetector Array Camera and Spectrometer* (PACS) (Poglitsch et al., 2010) on board the *Herschel Space Observatory* (Pilbratt et al., 2010). The [O I] 63 μm and [O III] 88 μm lines were observed in line-scan chop-nod mode (Obs. ID: 1342243546), with a total observing time of \sim 124 minutes, before the [O III] 52 μm and [O IV] 26 μm lines were observed simultaneously in range-scan mode (Obs. ID: 1342243547), with an observing time of \sim 38 minutes. All observations took place on March 25, 2012.

These observations were reduced using the Herschel Interactive Processing Environment (HIPE, Version 13) (Ott, 2010). For each of the oxygen lines, with the exception of the [O I] 63 μm line, the central $9''.4 \times 9''.4$ spatial pixel (spaxel) was used to generate the spectrum, and the results were point-source corrected. For the [O I] 63 μm line, the inner 3×3 spaxels of the integral field spectrometer were combined and point-source corrected to create one spectrum. This step was taken in order to correct what appears to be pointing jitter with this observation, as indicated by the presence of line flux on multiple spaxels. Significant line flux was not seen to extend over multiple spaxels for any of the other lines observed by *PACS*.

These line fluxes are reported in Table 2.1 and the line spectra are shown in Figure 2.1.

2.2.2 PdBI

As a follow-up to our detection of the [C II] line, we attempted to detect the CO(2–1) rotational line with the Plateau de Bure Interferometer (PdBI) in 3C 368. The observations were carried out on May 31 and June 1, 2010, with five antennas in the D configuration, producing a synthesized beam of size $4''.69 \times 4''.26$ (FWHM). Total on-source integration was 5.25 hr, with the band-1 receivers tuned to the redshifted frequency of the line, 108.183 GHz. We used the WideX correlator, which provides an instantaneous 3.6 GHz coverage in both polarizations. For this observation, we used MWC349 for absolute flux calibration. The data were calibrated and imaged using GILDAS¹, resulting in a 1σ sensitivity of $279 \mu\text{Jy beam}^{-1}$ for this observation, calculated over an assumed line width of

¹<https://www.iram.fr/IRAMFR/GILDAS>

500 km s^{-1} ; to match the width of the [C II] line. The line was not detected, with a 3σ upper limit, assuming the source is small with respect to the ($39 \times 35 \text{ kpc}$) beam, of $0.42 \text{ Jy km s}^{-1}$, or equivalently $1.5 \times 10^{-21} \text{ W m}^{-2}$.

We detect the 1.3 mm rest-frame continuum in both the northern and southern lobes of 3C 368. We report these values using our subsequent, more sensitive, ALMA observations.

2.2.3 ALMA

Having made no detection with the PdBI, we next attempted to detect the CO(2–1) line in 3C 368 with the Atacama Large Millimeter/submillimeter Array (ALMA)². These band-3 observations were performed on January 31, 2015, with a synthesized beam size of $3''.12 \times 1''.81$ (FWHM). Our on-source integration time was ~ 37 minutes.

For these observations, which were conducted with a precipitable water vapor (PWV) measurement of $7.9 \pm 0.1 \text{ mm}$, we used Titan as a flux calibrator, at a distance of 41.7° from the source, and J1751+0939 as both a phase and bandpass calibrator, located 3.6° from the source. Characteristic absolute flux calibrations with ALMA are accurate to $\sim 10\%$ (ALMA Technical Handbook). The data were reduced, imaged, and cleaned with the Common Astronomy Software Application (CASA)³, version 4.3.1.

The 1σ sensitivity for these observations is $134 \mu\text{Jy beam}^{-1}$, over an assumed line width of 500 km s^{-1} . Again the line is not detected. A 3σ detection limit for

²The National Radio Astronomy Observatory is a facility of the National Science Foundation operated under cooperative agreement by Associated Universities, Inc.

³<https://casa.nrao.edu/>

a source enclosed by the 25.8×15.0 kpc beam yields an upper limit on the line intensity of $0.201 \text{ Jy km s}^{-1}$, or equivalently, $7.3 \times 10^{-22} \text{ W m}^{-2}$.

This time, we detect the continuum in three components of 3C 368: the northern lobe at $673 \pm 39 \mu\text{Jy}$, the southern lobe at $712 \pm 45 \mu\text{Jy}$, and the core at $123 \pm 34 \mu\text{Jy}$ (see Figure 2.2).

In addition to the CO(2–1) line, we attempted to detect the [N II] 205 μm line with ALMA. These band-9 observations were carried out on February 21 and April 13, 2014, with a synthesized beam of size $0''.41 \times 0''.29$ (FWHM) and an on-source integration time of ~ 54 minutes.

For these observations, which were conducted with a PWV of 0.32 ± 0.02 mm, we used Titan as a flux calibrator, at a distance of 47.9° from the source, J1751+0939 as a phase calibrator, located 3.6° from the source, and J1924-2914 as a bandpass calibrator, 44.77° from the source. Characteristic absolute flux calibrations for observations performed in cycle 1 with the ALMA band-9 receivers are accurate to $\sim 15\%$ (ALMA Technical Handbook). The data were reduced, imaged, and cleaned with CASA, version 4.2.1.

We obtain a 1σ sensitivity of $891 \mu\text{Jy beam}^{-1}$, over an assumed line width of 500 km s^{-1} . Presuming that the line source is extended over ~ 2 beams (as the continuum contours in Figure 2.2 suggest), the 3σ upper limit is $3.78 \text{ Jy km s}^{-1}$ or $8.65 \times 10^{-20} \text{ W m}^{-2}$.

We detect the rest-frame 205 μm continuum, which traces thermal dust emission, from only the core component of 3C 368, with an integrated intensity of $5.6 \pm 1.3 \text{ mJy}$ (see Figure 2.2).

2.2.4 Spitzer/IRS

The [Ne II] $12.81\text{ }\mu\text{m}$, [Ne III] $15.56\text{ }\mu\text{m}$, and [Ne V] $14.32\text{ }\mu\text{m}$ lines were obtained from the Cornell Atlas of *Spitzer/IRS* Sources (CASSIS, Version 6) ([Lebouteiller et al., 2011](#)), and were observed as part of a program to study multiple radio galaxies and quasars near the peak of cosmic star formation using the *Spitzer Space Observatory* (PI: Martin Haas, AORKEY=22912000). The observations of 3C 368 were carried out on May 1, 2008, with the *InfraRed Spectrograph (IRS)* ([Houck et al., 2004](#)) in low-resolution long-slit mode (LL1), covering a wavelength range of $19.5\text{--}38\text{ }\mu\text{m}$. The total on-source integration time for these observations was ~ 48 minutes. The data were reduced and extracted using the CASSIS software, which employs an “optimal” extraction technique in order to produce a spectrum with the highest possible signal-to-noise ratio ([Lebouteiller et al., 2015](#)).

The line fluxes from the three neon lines are reported in Table 2.1, and the spectrum is plotted in Figure 2.3.

2.3 Results and Discussion

2.3.1 Line Fluxes

In order to determine the line fluxes for the fine-structure lines observed with *Herschel/PACS*, we sum the flux from the line channels (shaded in Figure 2.1), and propagate the statistical uncertainties per channel to calculate the signal-to-noise ratios. The channels associated with the spectral lines are determined by

a Gaussian fit to the line profiles (see Table 2.1), with two exceptions.

First, the central line velocity and FWHM obtained by a Gaussian fit to the [O I] 63 μm line, our most significant *Herschel/PACS* detection, are used to determine the line channels for the [O III] 88 μm line. This is necessary because of the low signal-to-noise in the [O III] 88 μm line spectrum.

Second, a Gaussian fit to the [O III] 52 μm line shows that it is considerably broader ($\Delta v \sim 760 \text{ km s}^{-1}$) than any of the other lines that we observed in 3C 368 (green dashed line, Figure 2.1). The reported flux for this line (see Table 2.1) is calculated by summing the flux from all channels under this best-fit Gaussian (shaded both yellow and cyan in Figure 2.1). Given that the signal-to-noise ratio per channel in the [O III] 52 μm line spectrum is $\lesssim 2$ and that the fitted velocity width is so much larger than that of the [O I] 63 μm line (our most significant oxygen line detection), we additionally calculate the flux by summing over only the channels coincident with our [O I] 63 μm line (red dashed line and yellow shaded channels in Figure 2.1). We use this flux value, $6.8 \times 10^{-18} \text{ W m}^{-2}$, which we use in all calculations involving line ratios, since the flux excluded from this value originates within a different velocity component of 3C 368.

With the exception of the [O III] 52 μm line, the central line velocities, $\sim +200\text{--}300 \text{ km s}^{-1}$ (calculated using $z = 1.131$), and velocity widths, $\sim 200\text{--}500 \text{ km s}^{-1}$, calculated for the fine-structure lines observed with *Herschel/PACS* are very similar.

The flux values along with central line velocities and FWHMs for the lines with higher signal-to-noise ratio, [Ne II] 12.81 μm and [Ne III] 15.56 μm , observed with *Spitzer/IRS* were obtained from the Infrared Database of Extragalac-

tic Observables from Spitzer (IDEOS) (Hernán-Caballero et al., 2016, Spoon et al. in prep.). The flux for the line with lower signal-to-noise ratio, [Ne V] $14.32\text{ }\mu\text{m}$, was obtained by summing the line channels, exactly as done for the *Herschel/PACS* spectra.

The central line velocities, determined by Gaussian fits to the [Ne II] $12.81\text{ }\mu\text{m}$ and [Ne III] $15.56\text{ }\mu\text{m}$ lines, overlap with those calculated for the oxygen lines observed with *Herschel/PACS* within the 2σ uncertainty level, indicating that these neon lines most likely originate within the same regions of 3C 368 as do the oxygen lines.

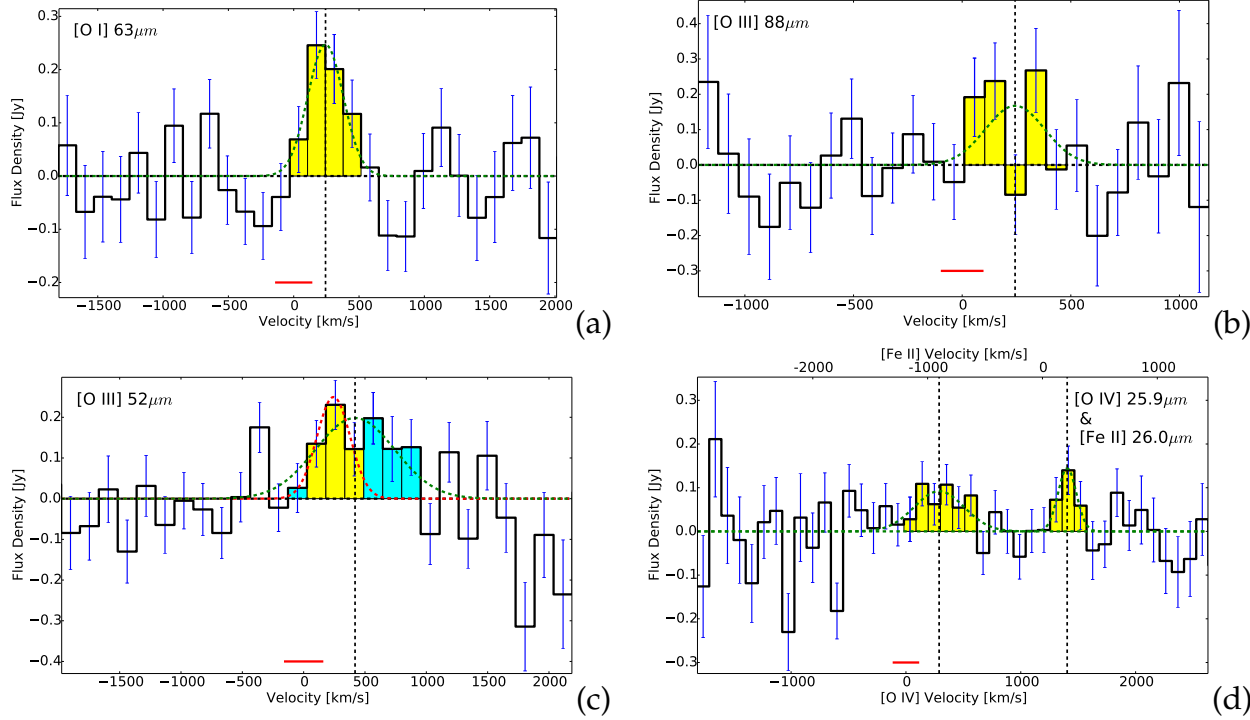


Figure 2.1 Spectral lines observed in 3C 368 with *Herschel/PACS*: (a) [O I] $63\mu\text{m}$ line, spectral resolution $\sim 270\text{ km s}^{-1}$; (b) [O III] $88\mu\text{m}$ line, spectral resolution $\sim 190\text{ km s}^{-1}$; (c) [O III] $52\mu\text{m}$ line, spectral resolution $\sim 300\text{ km s}^{-1}$; (d) [O IV] $25.9\mu\text{m}$ and [Fe II] $26.0\mu\text{m}$ lines, spectral resolution $\sim 210\text{ km s}^{-1}$. Gaussian fits to the line profiles are shown by the green dashed lines, with the central velocities indicated by vertical black dashed lines ($v = 0$ corresponds to $z = 1.131$). The blue error bars represent the 1σ statistical uncertainty in the flux measurement in each channel, and the red bar below each spectrum indicates the velocity resolution of that spectrum. The flux in the [O III] $52\mu\text{m}$ line is calculated in two different ways, one including both the yellow and cyan spectral channels, and the other using only the yellow spectral channels (see section on line fluxes).

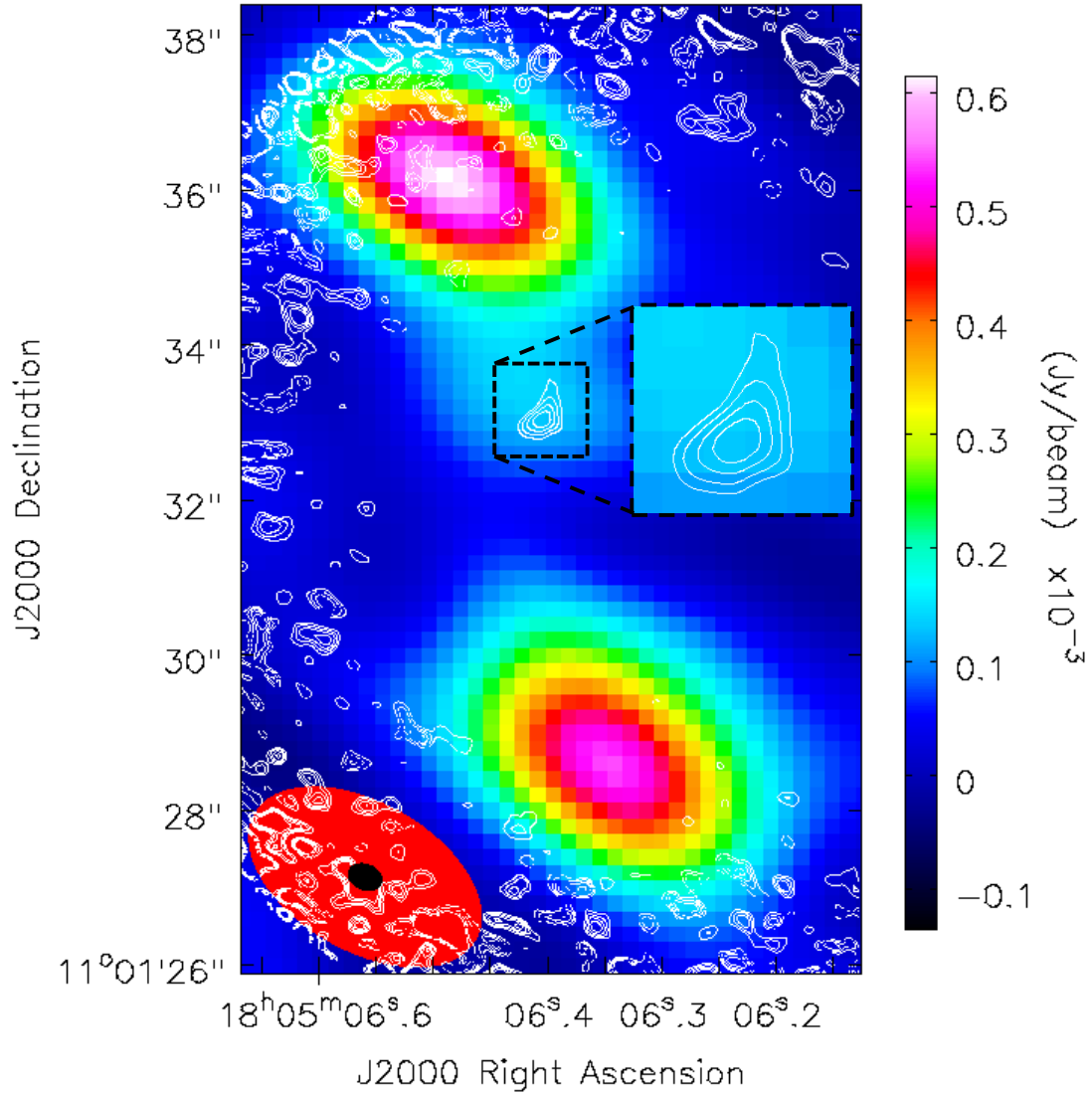


Figure 2.2 ALMA observations of the 1.3 mm (color map) and 205 μm (contours) rest-frame continua in 3C 368. The maps are primary-beam corrected. The contour levels are ± 3 , ± 4 , ± 5 , and $\pm 6\sigma$ (negative contours are dashed, $1\sigma = 0.4 \text{ mJy beam}^{-1}$). The beams are shown at the bottom left corner of the image, with the large (red) and small (black) ellipses from the 1.3 mm and 205 μm maps, respectively. The inset shows the 205 μm rest-frame continuum from the core of 3C 368.

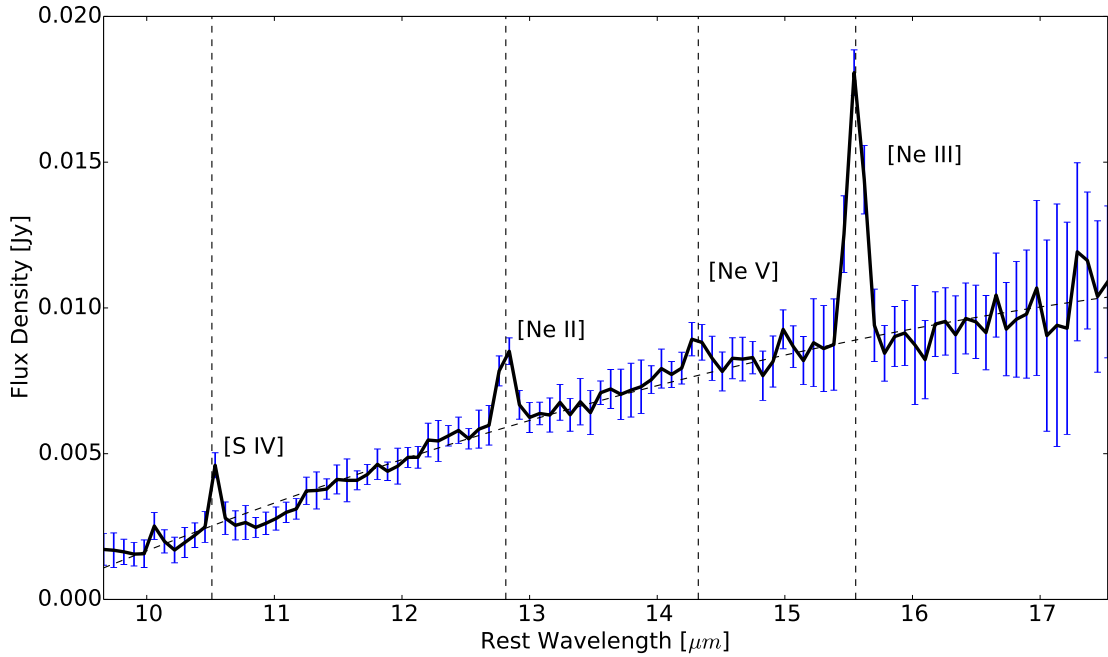


Figure 2.3 Spectral lines observed in 3C 368 with *Spitzer/IRS*. The positions of the various fine-structure lines are indicated by the vertical black dashed lines ($z = 1.131$). The blue error bars represent the 1σ statistical uncertainty in the flux measurement in each channel. The spectral resolution ranges from ~ 60 – 120 over the wavelength range of this observation.

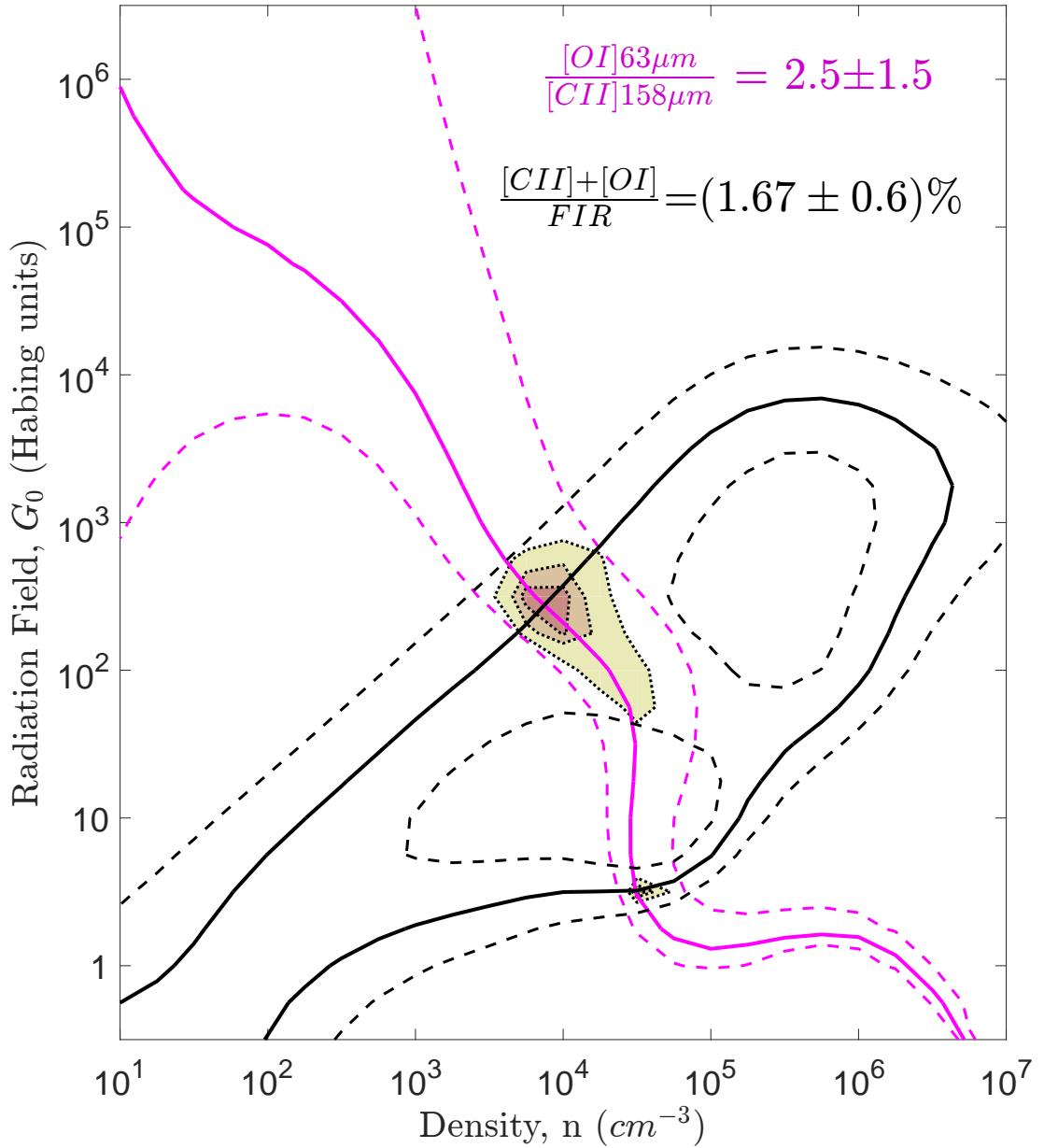


Figure 2.4 A plot of the best-fit PDR parameters in 3C 368, using the PDR Toolbox (Kaufman et al., 2006). The black (magenta) solid line traces the values of the radiation field (G_0) and density (n) allowed by the $[C\,II]+[O\,I]/FIR$ ($[O\,I]/[C\,II]$) ratio and is bounded by the uncertainty in the ratio (dashed lines). The three filled contours represent χ^2 fitting values of 0.25, 0.5, and 1.0. The fit favors PDRs with $G_0 \sim 280$ and $n \sim 7,500\,cm^{-3}$. The low G_0 solution is disregarded because it would result in an emitting region with an unphysically large size.

Table 2.1. Spectral lines observed in 3C 368

Line	[Ne II] 12.8 μm	[Ne V] 14.3 μm	[Ne III] 15.5 μm	[O IV] 25.9 μm	[Fe II] 26.1 μm	[O III] 51.8 μm	[O I] 63.2 μm	[O III] 88.4 μm	[C II] ^a 158 μm	[N II] 205 μm	CO(2–1) 1.3 mm
Critical Density (cm^{-3})	7×10^5 ^b	3×10^4 ^b	3×10^5 ^b	1×10^4 ^b	1×10^4 ^b	3.6×10^3 ^c	4.7×10^5 ^e	510 ^c	2.8×10^3 ^e	48 ^c	1.1×10^4 ^e
Flux ($10^{-18} \text{ W m}^{-2}$)	3.3 ± 0.6	1.5	9.1 ± 0.6	8.5	5.2	13.4 ^d	6.4	3.0	5.1	< 0.0865	< 0.00073
Significance (σ)	-	2.9	-	3.8	2.9	5.5	5.0	2.4	6.4	-	-
Line Center (km s^{-1})	-40 ± 210	-	-40 ± 100	290 ± 130	220 ± 60	420 ± 120	240 ± 40	240 ^e	-140	-	-
Line Width (km s^{-1})	3100 ± 700 ^f	-	3000 ± 200 ^f	510 ± 330	190 ± 120	760 ± 290	320 ± 90	320 ^e	-	-	-

Note. — The line fluxes were obtained by summing the flux over the line channels (shaded in Figure 2.1), while the line widths (FWHMs), positions ($v = 0$ corresponds to $z = 1.131$), and their associated uncertainties were obtained from fitting Gaussian line profiles to the data. The fluxes for the higher signal-to-noise ratio neon lines were obtained from Gaussian fits to the line profiles.

^aStacey et al. (2010b).

^bCormier et al. (2012).

^cCarilli & Walter (2013).

^dThis value is the full [O III] 52 μm line flux (sum of the yellow and cyan spectral bins in Figure 2.1). In all calculations involving line flux ratios, we sum only the spectral channels at the same velocity as the [O I] 63 μm line (yellow spectral bins in Figure 2.1). See the section on line fluxes for further explanation.

^eThe line position and FWHM of the [O III] 88 μm line are not left as a free parameters in the Gaussian fitting. Instead, the prior from the [O I] 63 μm line is assumed. See the section on line fluxes for further explanation.

^fThe large FWHM of the fitted Ne lines is due to the resolution of the IRS in the LL1 observing mode and is not the physical width of these lines.

*These critical densities correspond to lines originating from neutral gas regions.

2.3.2 Neon Lines: Disentangling the AGN Contribution

The mid-IR fine-structure lines in the *Spitzer/IRS* spectral regime that arise from the three ionization states of neon are excellent probes of the hardness of the ambient UV radiation fields in galaxies. It takes 21.56 eV photons to form Ne^+ , 40.96 eV photons to form Ne^{++} , and 97.11 eV photons to form Ne^{4+} . Therefore, the $12.81\ \mu\text{m}$ $[\text{Ne II}]$ line arises from H II regions formed by O/B stars, the $15.56\ \mu\text{m}$ $[\text{Ne III}]$ line arises from H II regions formed by O stars, and the $14.32\ \mu\text{m}$ $[\text{Ne V}]$ line requires the very hard UV radiation fields found near AGN or planetary nebula created by hot white dwarfs. This series of lines is quite useful since extinction corrections between these lines are modest, and the lines have similar critical densities (Table 2.1). Furthermore, since neon is a noble gas, its gas phase abundance is not dependent on local conditions, since it is neither depleted onto grains nor incorporated into molecules.

$[\text{Ne V}]$ line emission is known to be associated with planetary nebulae exposed to the hard UV radiation of very young white dwarfs (cf. [Bernard Salas et al., 2001](#)), but on galactic scales, detectable $[\text{Ne V}]$ is predominantly associated with the NLR of AGN. However, detectable $[\text{Ne III}]$ emission can arise from both the NLR of AGN and from H II regions formed by hot O stars. [Gorjian et al. \(2007\)](#) studied the neon fine-structure line emission from a variety of galaxies, including 77 3C radio sources, and found that the amount of $[\text{Ne III}]$ line emission from the NLR of AGN is directly proportional to the $[\text{Ne V}]$ line emission. Therefore, a simple scaling law, based on the observed $[\text{Ne V}]$ line emission from a galaxy, can be applied to estimate the fraction of the observed $[\text{Ne III}]$ line emission that arises from any central AGN. We use this scaling law to “correct” the $[\text{Ne III}]$ line emission for the AGN contribution before applying

any H II region models to the star forming regions in 3C 368.

Applying the relation of Gorjian et al. (2007),

$$\log \left(\frac{L_{\text{NeIII}}}{10^{33} W \text{ sr}^{-1}} \right) = 0.30 + 0.89 \log \left(\frac{L_{\text{NeV}}}{10^{33} W \text{ sr}^{-1}} \right), \quad (2.1)$$

to the observed luminosity of the [Ne V] $14.32 \mu\text{m}$ line, we estimate that 20% of the observed [Ne III] emission originates from the AGN, leaving 80% from star forming regions. This AGN-corrected 80% is the flux which we use in our star-formation-driven H II region models. We note that 3C 368 is comparable to the higher luminosity sources used in the determination of this [Ne III]/[Ne V] relation (Gorjian et al., 2007, Figure 1, right panel, of), where there are fewer sources and larger scatter in the trend, and so we also consider several limiting cases in the following analysis.

2.3.3 H II region Models

Given the large number of fine-structure lines observed in 3C 368, we can determine several properties of the H II regions within this source.

The ground-state-term level populations within the O⁺⁺ ion are density sensitive, so that the [O III] $52 \mu\text{m}$ /[O III] $88 \mu\text{m}$ line ratio yields the ionized gas density. We find a line ratio of 2.3, which indicates H II region gas densities of $n_e \sim 1000 \text{ cm}^{-3}$ (we here use the collision strengths from Palay et al., 2012).

Then, using the models of Rubin (1985), we can combine the [O III], [Ne II], and AGN-corrected [Ne III] fine-structure lines to arrive at a consistent model

for the H II regions in 3C 368. We find that the fit favors regions of star formation that are heated by stars with effective temperatures of $\sim 37,000$ K and with gas densities of $\sim 1000 \text{ cm}^{-3}$. The density is consistent with our estimates from the [O III] 52/88 μm line ratio, and the ionization state is consistent with the neon line ratios, provided that neon is overabundant to oxygen in 3C 368 by a factor of 3 compared with either the “N” models, which have Orion Nebular abundances ($\text{O/H} = 4.0 \times 10^{-4}$ and $\text{N/H} = 4.5 \times 10^{-5}$), or the “D” models, with all metals depleted by a factor of $\sqrt{10}$ from the N models.

This factor of three overabundance is consistent with the recent results of Rubin et al. (2016), who used *Spitzer* spectroscopy together with their ionization models and found neon-to-sulfur ratios (~ 12) for a wide variety of galaxies than were higher than previously expected. This suggests that the canonical neon-to-sulfur ratio (~ 3.7) that was used in the H II region models employed here is too low by a factor of about three. Since neon, sulfur, and oxygen are all primary elements, their abundances should scale together, and our neon overabundance when compared to oxygen is therefore consistent with this newly measured Ne/S ratio.

Because the AGN contribution to the [Ne III] line is only $\sim 20\%$, and because of the uncertainty in both the line fluxes and the scatter in the [Ne III]/[Ne V] correlation (0.2 dex in log space), we consider both the limiting case of no AGN contribution to the [Ne III] line and the case of the maximum allowed AGN contribution to the [Ne III] line ($\sim 40\%$). In all cases, we find that the models favor regions of star formation heated by stars with effective temperatures of $\sim 37,000$ K and with gas densities of $\sim 1000 \text{ cm}^{-3}$.

To retain the necessary effective stellar temperatures indicated by our mod-

eling, at the observed far-IR luminosity in 3C 368 ($2.0 \times 10^{12} L_{\odot}$, Podigachoski et al., 2015), we require a starburst with the equivalent of $\sim 1.2 \times 10^7$ O8 V stars (Vacca et al., 1996). Such a starburst would have an age of ~ 6.5 Myr (Meynet & Maeder, 2003), as constrained by the stellar lifetimes of the most massive stars. Using the 73 kpc radio source size of 3C 368 from Best et al. (1998a), and a range of jet propagation speeds from 0.03 to 0.3 c (King & Pounds, 2015), we estimate the duration of the latest episode of AGN activity to be between 0.4 to 4 Myr, comparable in time to the age of the starburst.

This concurrence lends further support to the possibility that we may be witnessing AGN-driven star formation in 3C 368, as has been suggested previously from the alignment of the radio and optical axes, which trace AGN jets and stars, respectively, seen in many of the 3CR galaxies, including 3C 368 (McCarthy et al., 1987). In addition to the optical continuum, Chambers et al. (1988) find the $2.2 \mu\text{m}$ continuum, also associated with stellar emission, to be aligned with both of the other axes.

It has also been previously suggested that 3C 368 may be undergoing a major merger (Djorgovski et al., 1987), providing another possible mechanism for triggering both black hole accretion and star formation simultaneously. While we cannot rule out this possibility, the $[\text{C II}]/F_{\text{FIR}}$ ratio of 0.5% in 3C 368 (see Sections 3.5 and 3.6) is more than an order of magnitude larger than the typical values found in the local ultraluminous infrared galaxies (ULIRGs), which are predominantly powered by major-merger-driven starbursts (e.g., Luhman et al., 1998).

The physical parameters derived from our H II region modeling also explain our non-detection of the $[\text{N II}] 205 \mu\text{m}$ line. At such hight effective temperatures,

Rubin (1985) calculated that $\sim 86\%$ of the nitrogen contained within the H II regions of 3C 368 would be in the N⁺⁺ state. Unfortunately, the [N III] 57 μm line is redshifted into an absorption band in the atmosphere for 3C 368 with $z = 1.131$ ($\sim 122 \mu\text{m}$), making observations impossible from the ground, and even beyond the reach of airborne facilities. These observations will have to wait for the next generation of far-IR space telescopes, such as the Space Infrared Telescope for Cosmology and Astrophysics (SPICA) and the Origins Space Telescope (OST).

2.3.4 Bounds on the N/O Ratio

Following Ferkinhoff et al. (2010), we can estimate the minimum mass of oxygen in the O⁺⁺ state in 3C 368 from the luminosity in the oxygen fine-structure lines:

$$M_{\min}(O^{++}) = \frac{F_{ul} 4\pi D_L^2 m_O}{\frac{g_u}{g_t} A_{ul} h \nu_{ul}}, \quad (2.2)$$

where F_{ul} is the flux in the fine-structure line between the upper (u) state and the lower (l) state, D_L is the luminosity distance (7.735 Gpc), m_O is the mass of an oxygen atom, g_u and g_l are the statistical weights of the upper and lower states, respectively, g_t is the partition function (the sum of the statistical weights of all relevant states available to the O⁺⁺ ion at $T = 8,000$ K), A_{ul} is the Einstein coefficient for the relevant transition ($2.6 \times 10^{-5} \text{ s}^{-1}$ for the [O III] 88 μm line, Carilli & Walter, 2013), and ν_{ul} is the frequency of that transition. Using the [O III] 88 μm line, we obtain a minimum O⁺⁺ mass of $4.4 \times 10^6 M_\odot$.

Similarly, we can use our 3σ upper limit for the [N II] 205 μm line flux ($A = 2.1 \times 10^{-6} \text{ s}^{-1}$, Carilli & Walter, 2013) to put a bound on the mass of N⁺ in

3C 368:

$$M_{\min}(N^+) < \frac{F_{ul} 4\pi D_L^2 m_N}{\frac{g_l}{g_t} A_{ul} h \nu_{ul}}. \quad (2.3)$$

We obtain a limit of $< 3.2 \times 10^6 M_\odot$.

We use the models of Rubin (1985) to calculate the total mass in oxygen and nitrogen by scaling from the fraction in the ionization state that we observe back to the total abundance of the element in question.

With $\sim 84\%$ of the oxygen in the O^{++} state, and $\sim 14\%$ of the nitrogen in the N^+ state, within the H II regions of 3C 368, we calculate masses of $5.3 \times 10^6 M_\odot$ and $< 2.3 \times 10^7 M_\odot$, for oxygen and nitrogen respectively.

Using these values, we find an upper limit for the N/O ratio in 3C 368 of 5.0. Asplund et al. (2009) reported a solar N/O abundance ratio of 0.126. While the result which we obtain is consistent with the solar N/O ratio, it also allows for enhanced nitrogen relative to oxygen.

We are continuing our campaign to detect the [N II] 205 μm line in 3C 368 and were recently granted ALMA time to push our sensitivity deeper in this source. These new observations will effectively double our on-source integration time, which will improve our sensitivity.

2.3.5 Photodissociation Regions

In addition to the lines associated with H II regions, we have also detected the [O I] 63 μm line associated with photodissociation regions (PDRs). [O I] and

[C II] are the two dominant coolants of PDRs, so that the sum of the line fluxes divided by the far-IR flux (which tracks the impinging FUV (6 – 13.6 eV) flux) tracks the efficiency of photoelectric heating. Parameterizing the FUV in terms of the local (Habing) interstellar radiation field, the photoelectric heating is sensitive to the ratio of FUV field strength to gas density, G_0/n . With different critical densities the line ratio constrains the PDR gas density, so that the line intensities and their ratio independently constrain G_0 and n .

We use our previous detection of [C II] (Stacey et al., 2010b), together with the PDR Toolbox (Kaufman et al., 2006), for our analysis. This software fits input line flux ratios to a bank of line ratios calculated using a radiative transfer code that assumes a plane-parallel geometry for the gas.

Before using this software, we correct for the different optical depths of the lines used in modeling the PDRs. The [O I] 63 μm line is likely to be optically thick for PDRs with A_V on the order of a few (e.g., Stacey et al., 1983, Tielens & Hollenbach, 1985). We therefore multiply the [O I] 63 μm line flux by a factor of two to account for its opacity (as in Stacey et al., 2010a), taking the uncertainty in this correction to be equal to the correction which we applied.

Owing to the lower abundance of C⁺, and the greater populations in its excited levels, the [C II] line is expected to have significantly smaller optical depth than the [O I] line. Observations of the hyperfine structure lines of ¹³C⁺ indicate optical depths lower than one of the order of 0.5-1.5 for galactic PDRs (cf. Bordeiko et al., 1988, Ossenkopf et al., 2013, Stacey et al., 1991). PDR models indicate optical depths of the same order (Kaufman et al., 1999). Therefore, we make no correction to the [C II] 158 μm line for opacity effects.

We perform an additional correction to remove any contributions to the [C II] $158\text{ }\mu\text{m}$ line emission originating from H II regions, which we subtract away before performing our PDR analysis. With an ionizing energy of only 11.26 eV, ionized carbon can be found both in the neutral hydrogen phases of the ISM (13.6 eV ionizing energy) and also in the ionized gas phase where species like ionized nitrogen (14.5 eV) exclusively reside (Oberst et al., 2006). Since the [N II] $205\text{ }\mu\text{m}$ and [C II] $158\text{ }\mu\text{m}$ lines have very similar critical densities in ionized gas regions, 48 cm^{-3} and 50 cm^{-3} , respectively, their ratio can be used to calculate the percentage of C⁺ coming from H II regions (Oberst et al., 2006). We calculate a flux ratio of [C II] $158\text{ }\mu\text{m}$ / [N II] $205\text{ }\mu\text{m}$ > 60 . Oberst et al. (2006) find that if all of the C⁺ observed were to come from H II regions, this ratio would vary from 3.1 for a low-density gas to 4.3 for a high-density gas, so that <7% of the [C II] $158\text{ }\mu\text{m}$ line flux in 3C 368 comes from within H II regions. Since this contribution is very small and within the uncertainties, we make no correction to the [C II] $158\text{ }\mu\text{m}$ line flux for our PDR analysis.

Finally, we correct the observed FIR luminosity to include only the component produced by the UV flux from young stars that has been reprocessed by the dust into the FIR. We adopt the fit from Podigachoski et al. (2015), who modeled the SED of 3C 368 with three components: one for the AGN-fueled warm dust component (using a library of torus models from Hönig & Kishimoto, 2010), one blackbody for the optical/NIR stellar emission, and one graybody in the FIR/submillimeter with the dust emissivity index (β) as a free parameter. We use the luminosity in this last component for our PDR analysis. Podigachoski et al. (2015) also used this FIR luminosity to calculate a star formation rate in 3C 368, obtaining a value of $350 M_{\odot}\text{ yr}^{-1}$.

Inserting these three observations (see Table 2.2), the corrected [C II] 158 μm and [O I] 63 μm line intensities, and the fitted FIR luminosity into the PDR Toolbox software (Kaufman et al., 2006), we obtain best fits for PDRs with $G_0 \sim 280$ and $n \sim 7,500 \text{ cm}^{-3}$ (see Figure 2.4). Using the scaling relations found in Wolfire et al. (1990), and adopting an FIR luminosity of $2.0 \times 10^{12} L_\odot$ (Podigachoski et al., 2015), we calculate that these PDRs are extended over 1.9 – 4.8 kpc, which is consistent with our CASA 2D Gaussian fit to the source from the rest-frame 205 μm continuum map ($\sim 1.0 \times 5.9 \text{ kpc}$, see Figure 2.2).

One potential caveat for our PDR modeling results is that the observed [C II] and [O I] lines may originate within the X-ray dominated region (XDR) surrounding the AGN of 3C 368 (e.g., Meijerink et al., 2007), with the [O III] lines coming from the closer-in NLR (e.g., Ferkinhoff et al., 2010). Because we can form a consistent picture of star formation in 3C 368 using our observations and because optical fine-structure lines have also been observed to be extended over several arcseconds around the central source (e.g., Best et al., 2000, Hammer et al., 1991, Jackson & Rawlings, 1997, Meisenheimer & Hippelein, 1992), the theory of large-scale star formation in 3C 368 seems more plausible.

This theory can be tested by spatially resolving the [C II] line emission in 3C 368. Extended [C II] emission may confirm the existence of large-scale star forming regions, while confined emission may suggest an AGN origin. We have been awarded ALMA time to carry out these very observations (see the section on future observations).

Table 2.2. Line corrections for PDR modeling

Line	[O I] 63.2 μm	[C II] ^a 158 μm	$F_{\text{FIR}}^{\text{b}}$
Uncorrected Flux ($10^{-18} \text{ W m}^{-2}$)	6.4	5.1	1075.0
Corrected Flux ($10^{-18} \text{ W m}^{-2}$)	12.8	5.1	1075.0
Uncertainty ($10^{-18} \text{ W m}^{-2}$)	6.4 ^c	1.5	107.5

^aStacey et al. (2010b).

^bPodigachoski et al. (2015).

^cWe take the uncertainty in the [O I] 63 μm line to be equal to the opacity correction which we applied.

2.3.6 Where is the CO?

While the fine-structure lines from PDRs allow us to model these regions in 3C 368, the complete picture of star formation can only come from including molecular gas observations as well. We have attempted to observe the CO(2–1) transition with both ALMA and PdBI, and like others in the past (e.g., Evans et al., 1996), we did not detect any emission. Our ALMA observations probe down to a sensitivity of $134 \mu\text{Jy beam}^{-1}$, over an assumed line width of 500 km s^{-1} .

Assuming a ratio of [C II] to CO(1–0) of $\sim 4,100$, which is typical of normal metallicity star forming regions in the Milky Way and starburst galaxies (Stacey et al., 1991), and a CO(2–1) to CO(1–0) flux ratio of 7.2 (90% of the high-temperature thermalized value), we would expect a [C II] to CO(2–1) flux ratio of ~ 570 in 3C 368. The 3σ CO upper limit from our ALMA observations, however, yields a limit of $[\text{C II}]/\text{CO}(2-1) > 7,000$, which is more than 12 times the expected value.

Following Scoville et al. (2016), we can estimate the total molecular gas mass

in 3C 368 using the 850 μm SCUBA observations from Archibald et al. (2001). Assuming a dust temperature of 35 K, consistent with the SED fit from Podigachoski et al. (2015), we obtain a value of $1.57 \times 10^{11} \text{ M}_\odot$. Then, using our upper limit for the CO(2–1) line and assuming that the gas is fully thermalized, we obtain a 3σ limit for $L'_{\text{CO}} < 3.45 \times 10^9 \text{ K km s}^{-1} \text{ pc}^2$. Using these values, we estimate an $\alpha_{\text{CO}} > 45.5 \text{ M}_\odot (\text{K km s}^{-1} \text{ pc}^2)^{-1}$ in 3C 368. This α_{CO} value is an order of magnitude higher than the typical range of values quoted in the literature, $\sim 0.8\text{--}4.3$ (e.g., Bolatto et al., 2013, Solomon & Vanden Bout, 2005).

Previous attempts to detect molecular gas using the CO(1–0) line in high-redshift radio galaxies have been largely unsuccessful (e.g., Emonts et al., 2014). Our limit of $L'_{\text{CO}} < 3.45 \times 10^9 \text{ K km s}^{-1} \text{ pc}^2$ is a factor of ~ 6.4 deeper than the lowest limit reported in Emonts et al. (2014) ($L'_{\text{CO}} < 2.2 \times 10^{10} \text{ K km s}^{-1} \text{ pc}^2$).

Comparing the observed $[\text{C II}]/F_{\text{FIR}}$ and upper limit $\text{CO}(1\text{--}0)/F_{\text{FIR}}$ ratios for 3C 368 to those of other sources (see, e.g., Hailey-Dunsheath et al., 2010, Figure 3), we find that 3C 368 has a higher $[\text{C II}]/F_{\text{FIR}}$ ratio ($\sim 0.5\%$) than either the starburst nuclei or galactic star forming regions, and deficient CO for a source with this $[\text{C II}]$ flux. There are several factors that might explain this anomalously high $[\text{C II}]/\text{CO}(2\text{--}1)$ line ratio, including the metallicity, age, and degree of fractionation of the molecular clouds in 3C 368.

Moving toward the core of a molecular cloud from its surface, a transition is made from C^+ to CO as carbon-ionizing and CO-dissociating photons are extinguished by dust. This transition occurs at $A_V \sim 3$ (Hollenbach & Tielens, 1999). If the dust-to-gas ratio follows metallicity, then it follows that the penetration depth of these carbon-ionizing photons can be very large in a low-metallicity ISM, making the CO core relatively small compared to the C^+ envelope, and

leading to high [C II]/CO ratios (e.g., [Maloney & Black, 1988](#), [Stacey et al., 1991](#)). While the CO-emitting core of a molecular cloud retreats as the metallicity decreases, the size of the molecular region, defined by the transition from H to H₂, does not. This transition from H to H₂ is set by the self-shielding of H₂ molecules and is therefore metallicity independent. CO would therefore be a poor tracer of the total molecular gas in low-metallicity molecular clouds, which could still be present in the near absence of CO (e.g., [Madden et al., 1997](#), [Poglitsch et al., 1995](#), [Stacey et al., 1991](#)).

However, the low-metallicity case seems unlikely for 3C 368, which has a stellar mass of $\sim 3.6 \times 10^{11} M_{\odot}$ ([Best et al., 1998b](#)). At the current star formation rate, it would take $\sim 10^9$ years to accumulate such a stellar population. Assuming that each star formation episode lasts $\sim 10^7 - 10^8$ years, 3C 368 would have been through $\sim 10 - 100$ cycles of star formation, making a low-metallicity ISM seem improbable. Additionally, 3C 368 lies on the galaxy main-sequence for a source at redshift 1.131 (using the definition of [Genzel et al., 2015](#)), furthering the idea that a low-metallicity ISM is not responsible for the lack of CO in this case.

A different scenario that might be used to explain the lack of CO is that the ISM in 3C 368 may be highly fractionated into small cloudlets. Such a fractioned ISM would have modest extinction to the core of individual cloudlets, allowing for considerable C⁺ emission with relatively little CO emission.

Since the upper limit from our CO observation shows that the line is suppressed from the expected value by more than 12 times, the CO-emitting cores of the molecular clouds in 3C 368 must correspondingly be more than $\sqrt{12} \times$ smaller in radius than the entire clouds. Taking A_V ~ 3 , or a corresponding

column density of $6 \times 10^{21} \text{ cm}^{-2}$, as the CO depth, and our fitted PDR density of $\sim 7,500 \text{ cm}^{-3}$, we calculate that the clouds in 3C 368 must have size $\sim 0.3 \text{ pc}$, smaller than the sizes derived for clouds in the highly disturbed ISM of M82 by [Lord et al. \(1996\)](#) ($0.4 - 1.0 \text{ pc}$), while the CO-emitting cores of these clouds must have size $< 0.1 \text{ pc}$.

Yet another possible explanation for the lack of CO in 3C 368 is that the molecular clouds in the galaxy may be chemically young. [Glover & Clark \(2012\)](#) have shown that C^+ recombines with free electrons to form C^0 in less than $\sim 0.1 \text{ Myrs}$, while the subsequent formation of CO from the neutral atoms can take significantly longer, $\sim 1-3 \text{ Myrs}$. It could be that we are observing these molecular clouds before they have had the chance to form an appreciable amount of CO.

The work of [Stoerzer et al. \(1997\)](#) suggests that a chemically young ISM may be possible here. Cloudlets within a clumpy ISM, moving relative to one other, can periodically shield each other from the intense UV radiation field present in the ISM. In this scenario, the [C II] which we observe would originate from the surfaces of dense cloudlets exposed to the intense UV field. The CO-emitting cores of the cloudlets would retreat toward the center each time they were exposed to the full UV field, and then take an appreciable time to reform after the next shielding event. This effect would be particularly pronounced if the cloudlets were small, and hence much of their volume was penetrated by UV photons between shielding events, as seems to be the case here. A testable prediction of this model would be the existence of considerable [C I] emission, since C^+ recombines quickly after the shielding event is initiated. For this reason, we plan follow-up observations of 3C 368 in [C I], in order to try and resolve the

mystery of the missing CO.

2.4 Future Observations

In an effort to answer some of the remaining questions pertaining to 3C 368, we have been awarded ALMA time to observe the [C II] $158\text{ }\mu\text{m}$ line, at $0''.2$ spatial resolution, to determine the extent of star formation in this source. The models which we have employed here predict star formation extended over kilo-parsec scales, which, if correct, will appear in the ALMA observations as an extended source over ~ 10 beams.

In addition to the ionized carbon line, we have also been awarded time to observe the [C I] $609\text{ }\mu\text{m}$ line in 3C 368 (the $370\text{ }\mu\text{m}$ line is blocked by the atmosphere). We expect that if the molecular clouds in the galaxy are indeed chemically young, the neutral carbon line will be very bright when compared to our CO line upper limit, since the CO would not have had sufficient time to form.

2.5 Conclusions

We have observed the fine-structure lines constituting the “oxygen toolkit” in 3C 368, including the [O I] $63\text{ }\mu\text{m}$, [O III] $52\text{ }\mu\text{m}$ and $88\text{ }\mu\text{m}$, and [O IV] $26\text{ }\mu\text{m}$ lines. Using these oxygen lines together with archival fine-structure neon lines in the mid-infrared, we have modeled the H II regions in 3C 368, using the models of Rubin (1985), and found them to be ionized by starbursts headed by O8 stars, with an age of ~ 6.5 Myr. This age is comparable to the estimated age of the

latest episode of AGN activity in 3C368, determined by the propagation of the radio lobes.

Given the rate of star formation that we are witnessing in 3C368, with the alignment of the optical and radio axes, and estimated age of both the starburst and most recent epoch of AGN activity, this source is a strong candidate for further study in the field of galaxy-BH coevolution.

We have also modeled the PDRs in 3C368 and found them to be consistent with star formation spread over kilo-parsec distance scales. However, we did not detect any CO in 3C368. Our 3σ limit for the CO(2–1) line is $<0.201 \text{ Jy km s}^{-1}$, or equivalently $<7.3 \times 10^{-22} \text{ W m}^{-2}$, a level 12 times smaller than the value expected from standard PDR models. The lack of CO emission may be due to a low-metallicity, highly-fractionated, or possibly chemically-young ISM. We find that the most likely explanation is that the ISM is highly fractionated into small clouds, perhaps as a result of the interactions between AGN winds and the star forming molecular clouds, causing it appear to chemically young. Future ALMA observations will enable us to test this theory of large-scale star formation in the highly fractionated ISM of 3C368.

CHAPTER 3

**RESOLVING STAR FORMATION ON SUBKILOPARSEC SCALES IN THE
HIGH-REDSHIFT GALAXY SDP.11 USING GRAVITATIONAL LENSING**

C. Lamarche, A. Verma, A Vishwas, G. J. Stacey, D. Brisbin, C. Ferkinhoff, T. Nikola,

S. J. U. Higdon, J. Higdon, M. Tecza

The Astrophysical Journal, 867:140, 2018

3.1 Introduction

One of the key goals of modern astrophysics is to understand the processes that govern star formation and galaxy assembly in the early universe. The epoch of peak star-formation rate density, which occurred between 8 and 11 billion years ago ($1 < z < 3$), is of particular interest to understanding the assembly of present-day massive elliptical galaxies. Within this epoch, most of the star formation is obscured by a heavy veil of dust (e.g., [Casey et al., 2014](#)). This dust absorbs stellar ultraviolet (UV) radiation and re-emits it thermally in the far-infrared (FIR). The best probes of the physical conditions within these dusty star-forming galaxies (DSFGs) therefore lie in the far-IR and include several bright fine-structure lines that emanate from astrophysically abundant species such as carbon, nitrogen, and oxygen. These FIR lines arise from energy levels in the ground state term whose degeneracy is broken by spin-orbit coupling. As such, they are easily excited at modest (few hundred K) gas temperatures. These FIR lines trace the physical conditions of the gas, often being important sources of gas cooling, such that they reveal the properties of the sources that heat the gas.

For example, the [C II] 158 μm line largely arises from warm, dense, photodissociation regions (PDRs) on the surfaces of molecular clouds and the [C II] to FIR continuum luminosity ratio is a sensitive measure of the far-UV (6 to 13.6 eV) radiation field intensity, G_0 , and hence star formation intensity (e.g., [Wolfire et al., 1990](#)). The [O I] 63 μm line arises from deeper within PDRs and, together with the [C II] line and FIR continuum, constrains the PDR gas density and further refines the estimate of G_0 .

The [O III] 88 and 52 μm , [N II] 122 and 205 μm , and [N III] 57 μm lines originate in ionized gas regions. The typical temperature of these H II regions is $\sim 8,000 \text{ K}$, and hence the populations in the FIR line-emitting levels, which lie a few hundred K above ground, are primarily sensitive to the density of the medium. Thus, line ratios within a given ionic species yield H II region density. Hardness of the radiation field strongly affects the ionization equilibrium of metal ions, such that comparing the relative brightness of lines emitted from ions with significantly different ionization potentials allows us to constrain that property. For example, the [O III] 88 μm and the [N II] 122 μm lines have nearly identical critical densities (510 cm^{-3} and 310 cm^{-3} , respectively, at 8,000 K) but significantly different formation potentials (O^{++} : 35 eV and N^+ : 14 eV). Hence, the [O III]/[N II] line ratio probes the hardness of the stellar radiation field, and thus the high-mass end of the current-day stellar mass function (e.g., [Ferkinhoff et al., 2011](#)). The combination of these ionized gas lines provides tight constraints on the UV field hardness and enables us to make estimates of the N/O abundance ratio (e.g., [Lester et al., 1987](#)).

Each of these lines has been surveyed for galaxies in the local universe (e.g., [Cormier et al., 2015](#), [Crawford et al., 1986](#), [Díaz-Santos et al., 2017](#), [Graciá-Carpio](#)

et al., 2011, Herrera-Camus et al., 2016, Hughes et al., 2015, Malhotra et al., 1997, 2001, Parkin et al., 2013, Stacey et al., 1991) and [C II] and [O I] surveys of high-redshift galaxies have appeared (e.g., Brisbin et al., 2015, Coppin et al., 2012, Gullberg et al., 2015, Stacey et al., 2010c). In this paper, we study the ISM and star forming conditions within H-ATLAS J091043.1-000321 (hereafter SDP.11), a strongly-lensed, ultraluminous infrared galaxy- (ULIRG-) like source, at $z = 1.7830$, using multiple far-IR fine-structure lines of carbon, nitrogen, and oxygen.

SDP.11 was first identified as a potential high-redshift, gravitationally lensed, source in the Science Demonstration Phase of the Herschel Astrophysical Terahertz Large Area Survey (H-ATLAS; Eales et al., 2010) due to its large observed $500 \mu\text{m}$ flux (Negrello et al., 2010). Follow-up observations conducted with Z-Spec on the Caltech Submillimeter Observatory (CSO) detected several mid-J CO lines, consistent with a redshift of 1.786 ± 0.005 (Lupu et al., 2012).

Bussmann et al. (2013) presented Submillimeter Array (SMA) observations of the thermal dust continuum at $880 \mu\text{m}$ (observed-frame) that revealed two images of the lensed galaxy separated by $\sim 2''.2$ on the sky. Negrello et al. (2014) identified an elliptical Einstein ring in near-infrared images taken with the Wide-Field Camera-3 onboard the Hubble Space Telescope (HST/WFC3). Using these data, the magnification factor due to gravitational lensing was estimated to be ~ 8 based on stellar emission (Dye et al., 2014) and ~ 11 based on thermal dust emission (Bussmann et al., 2013). The lensing galaxy was found to coincide with the position of a known optical source at $z = 0.792$.

Ferkinhoff et al. (2014) first reported the detection of the [C II] $158 \mu\text{m}$ line with the second-generation redshift (Z) and Early Universe Spectrometer

(ZEUS-2) on the Atacama Pathfinder Experiment (APEX) telescope. Combined with an estimate of the FIR luminosity and a preliminary estimate of the [O I] 63 μm line flux from *Herschel/PACS*, they constrained the source-averaged physical conditions of the photodissociation regions in SDP.11. They suggest that SDP.11 hosts an intense and dense starburst ($G_0 \sim 20,000$ Habing units, $n \sim 2,300 \text{ cm}^{-3}$), as evidenced by the low $L_{[\text{C II}]} / L_{\text{FIR}}$ ratio, $(1.0 \pm 0.3) \times 10^{-3}$, analogous to that of local ULIRGs, possibly driven by a merger.

Here we present follow-up observations of the [C II] 158 μm line, conducted with the Atacama Large Millimeter/submillimeter Array (ALMA), at a spatial resolution of 0''.2. We also present strong detections of a suite of far-IR fine-structure lines, arising from both neutral and ionized gas, observed with the *PACS* spectrometer onboard the *Herschel Space Observatory*, as well as multiband radio continuum observations conducted with the Karl G. Jansky Very Large Array (VLA). We combine these datasets with *Herschel/SPIRE* observations to constrain the time since the last starburst, estimate the gas-phase [N/O] abundance ratio, perform lens modeling of SDP.11 to recover the intrinsic (unlensed) properties of the source, and examine the variation in the [C II]/FIR ratio on 500 pc spatial scales.

We assume a flat ΛCDM cosmology, with $\Omega_M = 0.27$, $\Omega_\Lambda = 0.73$, and $H_0 = 71 \text{ km s}^{-1} \text{ Mpc}^{-1}$, throughout this paper (Spergel et al., 2003), such that $1'' = 8.54 \text{ kpc}$, $D_A = 1.76 \text{ Gpc}$, and $D_L = 13.65 \text{ Gpc}$.

3.2 Observations and Data Reduction

3.2.1 ALMA

The [C II] 158 μm line was observed in SDP.11 using the Atacama Large Millimeter/submillimeter Array (ALMA)¹ Band 9 receivers. The observations were conducted on November 16, 2016, with the array in the C40-4 configuration, using 42 antennas, with baselines ranging from 15 to 920 m, under excellent weather conditions, with a precipitable water vapor (PWV) measurement of 0.28 mm. Observing at 683 GHz in this array configuration, the interferometer is sensitive to a maximum recoverable scale of $\sim 1''.3$. The total on-source integration time for these observations was 12.6 minutes.

For these observations, J0854+2006, J0522-3627, and J0909+0121 were used as the bandpass, flux, and phase calibrators, respectively. The data were reduced, imaged, and cleaned using the Common Astronomy Software Application (CASA)², version 4.7.2.

The [C II] data were imaged using 50 km s^{-1} spectral channels and natural weighting, achieving a synthesized beam of size $0''.20 \times 0''.16$. The RMS sensitivity is $\sim 4.5 \text{ mJy beam}^{-1}$ in each 50 km s^{-1} channel.

A continuum image was created by combining all nonline spectral channels present in the measurement set, for a total continuum bandwidth of $\sim 6.5 \text{ GHz}$, which, when imaged similarly to the [C II] line, yields a beam size of $0''.20 \times 0''.15$ and an RMS sensitivity of $0.72 \text{ mJy beam}^{-1}$.

¹The National Radio Astronomy Observatory is a facility of the National Science Foundation operated under cooperative agreement by Associated Universities, Inc.

²<https://casa.nrao.edu/>

3.2.2 Herschel/PACS

The [O IV] 26 μm , [S III] 33 μm , [O III] 52 μm , [N III] 57 μm , and [O I] 63 μm fine-structure lines were all observed in SDP.11 using the *Photodetector Array Camera and Spectrometer* (PACS) (Poglitsch et al., 2010) onboard the *Herschel Space Observatory* (Pilbratt et al., 2010) (OBS ID's: 1342231291, 1342231292, 1342231293, and 1342231294). All of these observations were conducted on October 20, 2011, using the instrument in the RangeSpec mode, with a duration of $\sim 30 - 90$ minutes per observation, and central pointing coordinates of ($9^h10^m43^s.1$, $-00^\circ03'24''.0$). The velocity resolution of these observations is $\sim 110 \text{ km s}^{-1}$, with a typical 1σ statistical noise of $\sim 35 - 85 \text{ mJy}$ per velocity bin.

The raw data were processed using the Herschel Interactive Pipeline Environment (HIPE) (Ott, 2010) version 15.0.1. A point-source correction was applied to the spectrum extracted from the central $9'.4 \times 9'.4$ spatial pixel (spaxel), since the diameter of the Einstein ring is only $\sim 2''.2$.

3.2.3 Herschel/SPIRE

The [O III] 88 μm , [N II] 122 μm , and [C II] 158 μm lines were all observed in SDP.11 using the *Spectral and Photometric Imaging Receiver* (SPIRE) (Griffin et al., 2010) onboard the *Herschel Space Observatory* and were first presented in Zhang et al. (2018).

The raw data were processed using the Herschel Interactive Pipeline Environment (HIPE) (Ott, 2010) version 15.0.1, with SPIRE calibration, version 14.3. The baselines of the resulting spectra were corrected for instrumental effects

using the off-source detectors. The continuum was fitted with a second-order polynomial, and absolute flux calibration was verified by comparing synthetic photometry generated from the spectra, using the HIPE script “spireSynthPhotometry,” to *SPIRE* photometer maps of SDP.11.

3.3 Results and Discussion

3.3.1 Line and Continuum Fluxes

The [C II] 158 μm line is strongly detected in the ALMA observations, emanating from a nearly complete, elliptical, Einstein ring with a diameter of $\sim 2''$ and an axial ratio of ~ 0.8 (see Figure 3.1). The line has two clearly defined velocity components, separated by $\sim 310 \text{ km s}^{-1}$, which appear as two spatially offset Einstein rings on the sky. Creating a moment-zero, primary-beam-corrected map by collapsing the spectral cube along the velocity axis and summing the flux from pixels detected at $> 3\sigma$ in either the red or blue component of the line in the flat-noise maps, we calculate a source-integrated [C II] 158 μm flux of $260 \pm 9 \text{ Jy km s}^{-1}$, or equivalently $(5.9 \pm 0.2) \times 10^{-18} \text{ W m}^{-2}$, where the uncertainties are estimated by propagating the RMS error per beam over the line-emitting region of the source. This method of calculating the flux by creating a mask using the flat-noise map and then applying that mask to the primary-beam-corrected map is employed because the pointing of our ALMA observations was offset from the center of SDP.11 by $\sim 2''$, such that the noise around the source is nonuniformly amplified by the necessary primary-beam correction.

In contrast to the stellar emission seen in HST/WF3 near-IR images and

the [C II] line emission, the rest-frame 158 μm continuum, measured from the ALMA observations, emanates prominently from two locations along the Einstein ring of SDP.11, one in the north and one in the south, which lie neatly between the red and blue Einstein rings seen in the [C II] line emission (see Figure 1). Again, summing the flux density in the primary-beam-corrected map from pixels detected at $> 3\sigma$ in the flat-noise map, we obtain a source-integrated specific flux of 189 ± 4 mJy at 158 μm rest-frame, where the uncertainty is estimated by propagating the RMS error per beam over the continuum-emitting region of the source. We note that this 3σ hard cut should be considered a lower limit on the total flux density since it does not consider extended flux that may be present at lower significance. We expect that extended flux should be present beyond what we observe, given that *SPIRE* photometry measures 232 ± 8 mJy at 500 μm (observed-frame; [Bussmann et al., 2013](#)), the closest photometric point to our continuum measurement at 440 μm (observed-frame).

The ALMA observations of the [C II] 158 μm line in SDP.11 clearly resolve the line into two velocity components (see Figure 3.2). We fit the source-integrated spectrum with a dual Gaussian line profile, one for each velocity component. We suggest a refined redshift for the source of 1.7830 ± 0.0002 for the [C II] 158 μm line, calculated as the average redshift of the two line components, with the error taken from the uncertainty in the Gaussian fitting. This redshift is consistent with the value of 1.786 ± 0.005 reported in [Lupu et al. \(2012\)](#), determined from Z-Spec observations of several mid-J CO lines. From this updated redshift, the [C II] line components are located at $v = -155 \pm 18 \text{ km s}^{-1}$ and $155 \pm 5 \text{ km s}^{-1}$, and have integrated fluxes of $124 \pm 21 \text{ Jy km s}^{-1}$ and $185 \pm 14 \text{ Jy km s}^{-1}$, respectively.

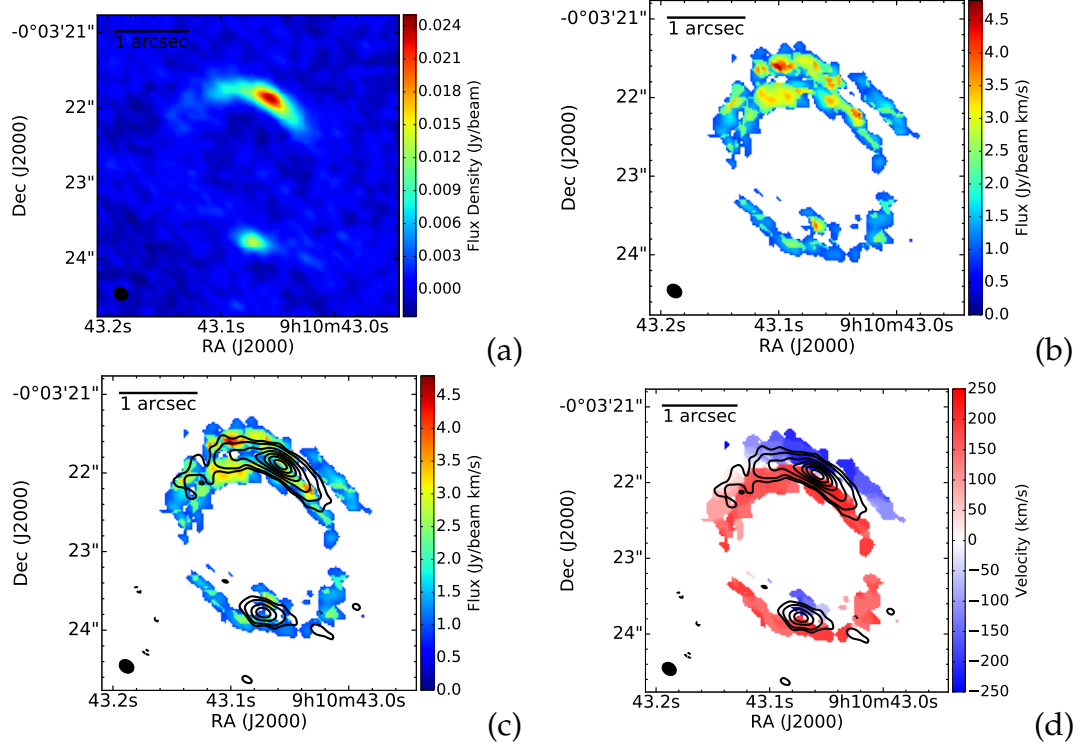


Figure 3.1 (a) SDP.11 rest-frame 158 μm continuum color map, at 0''.2 resolution. The dust continuum emanates prominently from two locations along the Einstein ring. (b) SDP.11 [C II] 158 μm moment-zero color map, at 0''.2 resolution. The moment-zero map was created using a threshold of 4σ per velocity channel. A nearly complete Einstein ring is visible in the line emission which is clearly resolved in the radial direction. (c) SDP.11 [C II] 158 μm moment-zero color map, with rest-frame 158 μm continuum contours superimposed (-5, -3, 3, 5, 10, 15, 20, 25, 30 σ , negative contours dashed), at 0''.2 resolution. (d) SDP.11 [C II] 158 μm moment-one map, created using a threshold of 4σ per velocity channel, with the same rest-frame 158 μm continuum contours as in (c) overplotted. The two velocity components of the [C II] line are spatially offset on the sky, with the continuum emission centered between them.

We use the best-fit [C II] line velocities as priors for fitting the *Herschel/PACS* spectra, only allowing the central line velocity to vary by one *PACS* spectral bin in either direction, and varying the line widths and intensities. The resulting line fluxes are presented in Table 3.1, with the spectra and overplotted best-fit line profiles in Figure 3.3.

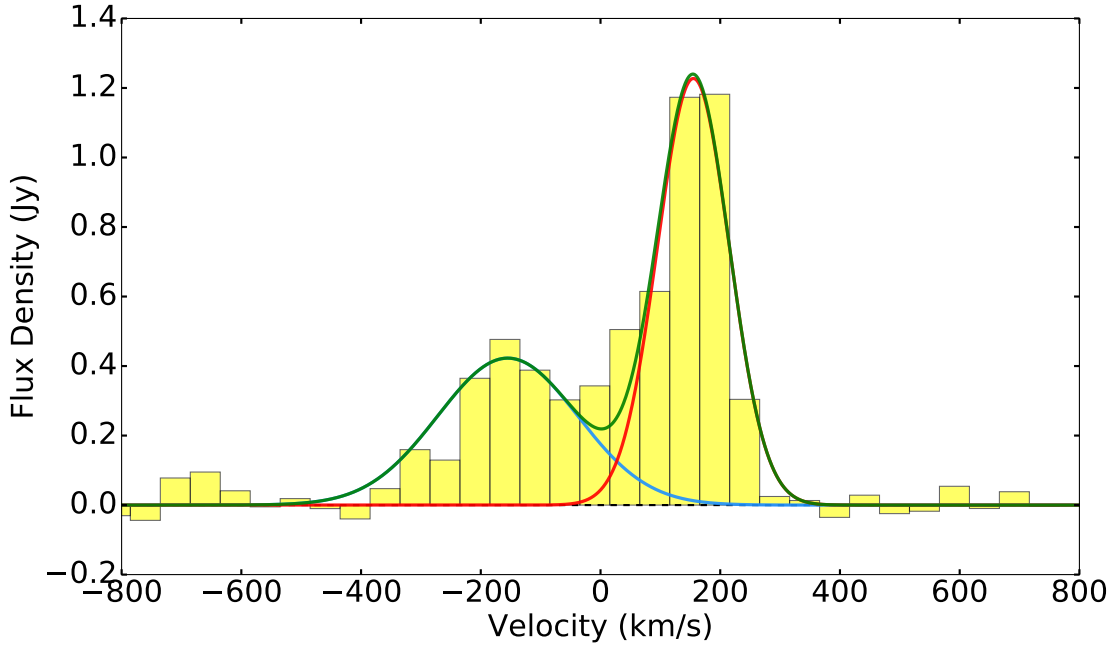


Figure 3.2 Source-integrated ALMA [C II] $158\mu\text{m}$ spectrum of SDP.11 ($v = 0$ corresponds to $z = 1.7830$). The line is clearly resolved into two velocity components, which we fit with two Gaussian line profiles (blue and red curves). The sum of the two components is shown in green.

The 3σ limits for the nondetected lines observed with *Herschel/PACS*, also reported in Table 3.1, were determined by calculating the standard deviation of the baseline at the native spectral resolution of the instrument, at the wavelength of interest, and then binning up to an assumed line width of 500 km s^{-1} .

Fluxes for the lines observed with *SPIRE* were calculated using the built-in HIPE spectrum fitter. HIPE documentation recommends using a Sinc-Gauss model, which combines an intrinsic Gaussian line profile with the Sinc instrument response function, for fitting marginally resolved spectral lines. We used the built-in HIPE spectrum fitter and simultaneously fit Sinc-Gauss models for the well-detected [C II] and [O III] lines, using priors for the line position, width, and separation between the two components, from the ALMA [C II] spectrum, thus our reported fluxes differ slightly from [Zhang et al. \(2018\)](#).

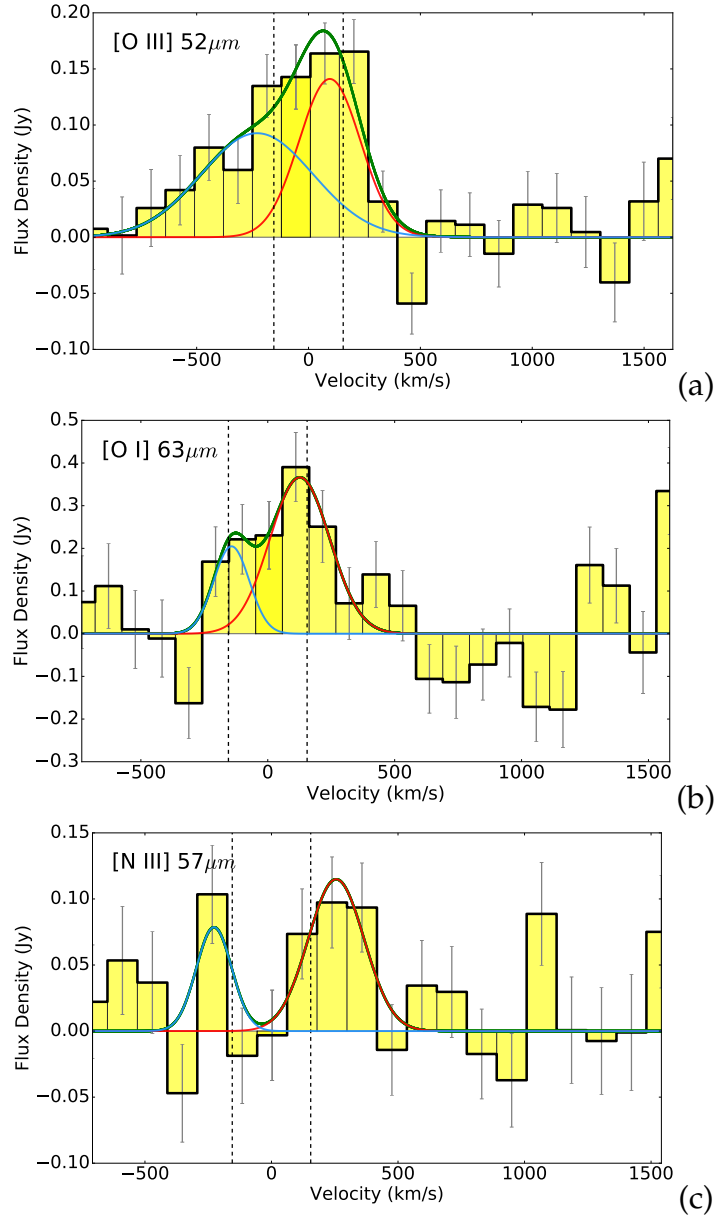


Figure 3.3 *Herschel/PACS* spectra of the (a) $[O\text{ III}]$ $52\text{ }\mu\text{m}$ (130 km s^{-1} bins), (b) $[O\text{ I}]$ $63\text{ }\mu\text{m}$ (105 km s^{-1} bins), and (c) $[N\text{ III}]$ $57\text{ }\mu\text{m}$ (118 km s^{-1} bins) lines in SDP.11, plotted with 1σ statistical error bars ($v = 0$ corresponds to $z = 1.7830$). We fit each of the lines with two Gaussian components (red and blue curves), with the sum of the two components shown in green. The positions of the two line components observed in the ALMA $[C\text{ II}]$ $158\text{ }\mu\text{m}$ spectrum are indicated by vertical dashed lines. The spectral lines observed with *Herschel/PACS* seem to have the same asymmetric line profile as does the $[C\text{ II}]$ $158\text{ }\mu\text{m}$ line.

While the [C II] 158 μm flux that we measure with ALMA is consistent with our previous line flux measurement from APEX/ZEUS-2, $(6.44 \pm 0.42) \times 10^{-18} \text{ W m}^{-2}$ (Ferkinhoff et al., 2014), it is notably lower than the flux obtained from the *SPIRE* measurements, $(12.9 \pm 1.3) \times 10^{-18} \text{ W m}^{-2}$. The same flux discrepancy is found by Zhang et al. (2018), between their reported APEX/SEPIA and *SPIRE* fluxes. This flux discrepancy could be partially due to the diameter of the Einstein ring, $\sim 2''.2$, being larger than the maximum recoverable scale of the utilized ALMA array configuration in band 9, $\sim 1''.3$, such that we are resolving out flux with the interferometer. However, since the ZEUS-2 and SEPIA observations were conducted using a single-dish, they should not be susceptible to such issues. It is also possible that the larger bandwidth of the *SPIRE* spectrum, compared to the ZEUS-2 or ALMA spectra, makes it sensitive to flux from broader spectral features (e.g., outflows), including a broader component of the [CII] line to which our ALMA and ZEUS-2 observations are not sensitive (e.g., Maiolino et al., 2005, 2012). We cannot fully explain the difference between the larger *SPIRE* [C II] flux measurement and the three consistent measurements with ZEUS-2, ALMA, and SEPIA at this time.

3.3.2 Dust Opacity

Before continuing, it is worth noting that even at the far-IR wavelengths discussed here, dust extinction can sometimes be non-negligible. We can estimate the wavelength-dependent dust opacity by modeling the far-IR SED as a modi-

fied blackbody (e.g., Blain et al., 2003):

$$\frac{S_{\nu_r}}{\Omega_{source}} = \frac{1}{(1+z_s)^3} (B_{\nu_r}(T_{dust}) - B_{\nu_r}(T_{CMB})) (1 - e^{-\tau_{\nu_r}}) \quad (3.1)$$

where Ω_{source} is the source size, $B_{\nu_r}(T)$ is the blackbody function evaluated at the rest-frame frequency ν_r and temperature T, and $\tau_{\nu} = (\frac{\nu}{\nu_0})^{\beta} = (\frac{\lambda_0}{\lambda})^{\beta}$ (e.g., Draine & Lee, 1984). Given that gravitational lensing conserves surface brightness, e.g. S_{ν}/Ω_{source} , we use both the observed flux density (uncorrected for lensing) and image-plane source size for this calculation. We estimate an image-plane source size of ~ 0.7 square arcseconds for SDP.11, by applying the same 3σ mask as was used to calculate the $158 \mu\text{m}$ rest-frame continuum flux density. Taking this source size together with the SED-modeled dust temperature of 41K (Bussmann et al., 2013), and the continuum flux at $158 \mu\text{m}$ (rest-frame), we find that $\lambda_0 \sim 20 \mu\text{m}$ (assuming a dust emissivity index, β , value of 1.5). This dust opacity corresponds to corrections ranging from $\sim 21\%$ at $52 \mu\text{m}$, our shortest wavelength — and hence most highly extincted — detected spectral line, to $\sim 4\%$ at $158 \mu\text{m}$, calculated under the approximation that the dust acts as a screen in front of the emitting gas. We apply these extinction corrections to all spectral lines, in all subsequent calculations, and to the luminosities calculated in Table 3.1.

Table 3.1. Spectral lines observed in SDP.11

Line	[O III] 51.8 μm	[O I] 63.2 μm	[N III] 57.3 μm	[O IV] 25.9 μm	[S III] 33.5 μm	[N II] 121.9 μm	[O III] 88.4 μm	[C II] (ALMA) 157.7 μm	[C II] (SPIRE) 157.7 μm
Observed Flux $\mu S \Delta v$ ($10^{-18} \text{ W m}^{-2}$)	7.2 ± 1.2	8.2 ± 2.6	2.9 ± 1.5	< 9.4	< 7.2	< 5.8	8.5 ± 1.6	$5.9 \pm 0.2^*$	12.9 ± 1.3
Estimated Dust Opacity (τ)	0.24	0.18	0.21	0.68	0.46	0.07	0.11	0.05	0.05
Dust Opacity Correction (%)	21.3	16.3	18.6	49.3	37.0	6.4	10.2	4.4	4.4
τ -Corrected Luminosity μL ($10^{10} L_\odot$)	5.2	5.6	2.0	< 8.1	< 5.8	< 3.6	5.5	3.6	7.9

Note. — “ μ ” is the gravitational lensing magnification factor and all quantities appearing with a μ are observed quantities and hence not corrected for magnification due to gravitational lensing. Intrinsic fluxes are obtained by dividing the observed fluxes by μ . Upper limits displayed in the table are 3σ limits. τ -corrected luminosities include an opacity correction to the line luminosity due to dust attenuation (see the text).

*This uncertainty is determined using the RMS error per beam in the ALMA [C II] 158 μm moment-zero map and does not consider uncertainty due to resolving out flux with the interferometer.

Table 3.2. Radio-continuum observations of SDP.11

Observed Frequency (GHz)	1.43	6.0	15.0	33.0
$\mu S_{\nu,obs}$ (μ Jy)	642 ± 176^a	316 ± 26^b	171 ± 14^b	110 ± 13
$\mu S_{\nu,rest}$ (μ Jy)	231 ± 63	114 ± 9	61 ± 5	40 ± 5
Free-Free Fraction (%)	5.2	11.5	18.3	26.5

Note. — The flux densities reported in this table are observed quantities, as indicated by the “ μ ’s”, and hence not corrected for magnification due to gravitational lensing. $S_{\nu,obs}$ and $S_{\nu,rest}$ are related by conserving νS_{ν} under redshift. The free-free fraction indicates the thermal contribution to the total radio continuum at each observed frequency (see the text).

^aBecker et al. (1995)

^bFerkinhoff et al. (in prep.), Ferkinhoff et al. (2017)

3.3.3 H II Regions

The fine-structure lines that we observe in SDP.11 allow us to determine the properties of the ionized gas within this source.

Gas Density and Hardness of the Radiation Field

The level populations of the ground state within the O⁺⁺ ion are density sensitive, such that the [O III] 52 μ m/[O III] 88 μ m line ratio yields the ionized gas density in the regime from $n_e \sim 100$ to 30,000 cm⁻³. We find a line ratio of ~ 0.9 , which indicates H II regions in the low-density limit ($n_e \lesssim 100$ cm⁻³), where here we use the collision strengths from Palay et al. (2012).

Similarly, we use the [N III] 57 μ m/[N II] 122 μ m line ratio to constrain the

hardness of the stellar radiation field. Given our upper limit on the [N II] 122 μm line, we calculate a ratio of > 0.6 . Using the models of Rubin (1985), and the density determined from the [O III] lines, we find that this ratio is consistent with H II regions powered by stars with effective temperatures $> 31,000$ K.

Since the radiation fields on galactic scales in star-formation-dominated galaxies are dominated by the most massive stars on the main sequence, this stellar effective temperature suggests that the starburst in SDP.11 is powered by stars of type B0 or hotter (Vacca et al., 1996), which in turn suggests that the time since the last starburst is $\lesssim 8$ Myr (Meynet & Maeder, 2003), or perhaps that it is still ongoing.

Ionized Gas Mass

Following Ferkinhoff et al. (2010), we can estimate the minimum ionized gas mass required to produce the observed [O III] line flux:

$$M_{\min}(H^+) = \frac{F_{ul}4\pi D_L^2 m_H}{\frac{g_l}{g_t} A_{ul} h \nu_{ul} X_{O^{++}}}, \quad (3.2)$$

where F_{ul} is the flux in the fine-structure line between the upper (u) state and the lower (l) state, D_L is the luminosity distance (13.65 Gpc), m_H is the mass of the hydrogen atom, $X_{O^{++}}$ is the relative abundance of O⁺⁺/H⁺ within the H II regions, g_u and g_l are the statistical weights of the upper and lower states, respectively, g_t is the partition function (the sum of the statistical weights of all relevant states available to the O⁺⁺ ion at T = 8,000 K), A_{ul} is the Einstein coefficient for the relevant transition ($2.6 \times 10^{-5} \text{ s}^{-1}$ for the [O III] 88 μm line; Wiese et al., 1966), and ν_{ul} the frequency of that transition. Using the opacity-

corrected [O III] 88 μm line luminosity and assuming $X_{O^{++}} = 5.9 \times 10^{-4}$ ([Savage & Sembach, 1996](#)), we obtain a minimum ionized gas mass of $1.5 \times 10^9 M_\odot$.

Gas-Phase Metallicity

Comparing the fine-structure line emission to the strength of the thermal free-free emission allows us to determine the absolute gas-phase abundance of the ions that we observe in fine-structure line emission (e.g., [O⁺⁺/H] and [N⁺⁺/H]). This is because the collisionally-excited fine-structure line emissivities scale with the product of electron and ion number density, $\epsilon_{fs} \propto n_e n_i$, while thermal free-free emissivity scales with the square of the electron number density, $\epsilon_{ff} \propto n_e^2$, and hence the ratio of fine-structure line flux to radio free-free flux determines the absolute abundance of the relevant ion, $F_{fs}/S_{ff} \propto n_i/n_e$.

To leverage this gas-phase abundance diagnostic in a number of high-redshift galaxies, we are conducting the ZEUS INvestigated Galaxy Reference Sample (ZINGRS) radio survey ([Ferkinhoff et al. \(in prep.\)](#), [Ferkinhoff et al., 2017](#)) with the National Science Foundation’s Karl G. Jansky Very Large Array (VLA)³, which aims to observe the radio continuum in high-redshift galaxies detected in FIR fine-structure lines at both 6 and 15 GHz (observed-frame), effectively measuring the strength of their free-free emission. Here, we use the 6 and 15 GHz radio fluxes from the ZINGRS radio survey (Project IDs: 16B-331 and 16A-375, respectively), combined with 1.43 GHz (observed-frame) continuum from the VLA Faint Images of the Radio Sky at Twenty centimeters (FIRST) survey ([Becker et al., 1995](#)) and archival VLA data taken at 33 GHz (observed-frame; PI: T. Greve, Project ID: 15B-266), to determine the contribution of the

³The National Radio Astronomy Observatory is a facility of the National Science Foundation operated under cooperative agreement by Associated Universities, Inc.

thermal free-free emission to the total radio continuum in SDP.11. These flux densities are presented in Table 3.2.

We decompose the radio continuum into thermal and nonthermal components using an equation of the following form (e.g., Condon, 1992, Klein et al., 2018):

$$S_{total,r} = S_{th,0,r} \left(\frac{\nu}{\nu_{0,r}} \right)^{-0.1} + S_{nth,0,r} \left(\frac{\nu}{\nu_{0,r}} \right)^{-\alpha_{nth}} \quad (3.3)$$

where $S_{th,0,r}$ and $S_{nth,0,r}$ are the (rest-frame) contributions to the total radio flux from the thermal and nonthermal components, respectively, at $\nu_{0,r}$ (rest-frame), and α_{nth} is the nonthermal power-law index. Adopting a $\nu_{0,r}$ value of 1 GHz, as in Klein et al. (2018), and holding α_{nth} fixed at 0.7, a median value for cosmic-ray electrons accelerated in shocks (e.g., Shu, 1991), we fit for $S_{th,0,r}$ and $S_{nth,0,r}$. We find best-fit values of $S_{th,0,r} = 17 \pm 8 \mu\text{Jy}$ and $S_{nth,0,r} = 675 \pm 68 \mu\text{Jy}$ (see Figure 3.4). At a rest-frame frequency of 3.98 GHz (1.43 GHz observed-frame), where we set our calculations, the free-free contribution to the radio emission is $15 \pm 7 \mu\text{Jy}$ (rest-frame). See Table 3.2 for the thermal contribution to the total radio SED in SDP.11 at each observed frequency.

The method for calculating gas-phase absolute ionic abundances from radio free-free and fine-structure line emission is well established in the literature (c.f. Herter et al., 1981, Rudolph et al., 1997), and can provide an unbiased abundance diagnostic for heavily dust obscured galaxies, especially in the early universe where the traditional optical diagnostics can be difficult to observe and/or

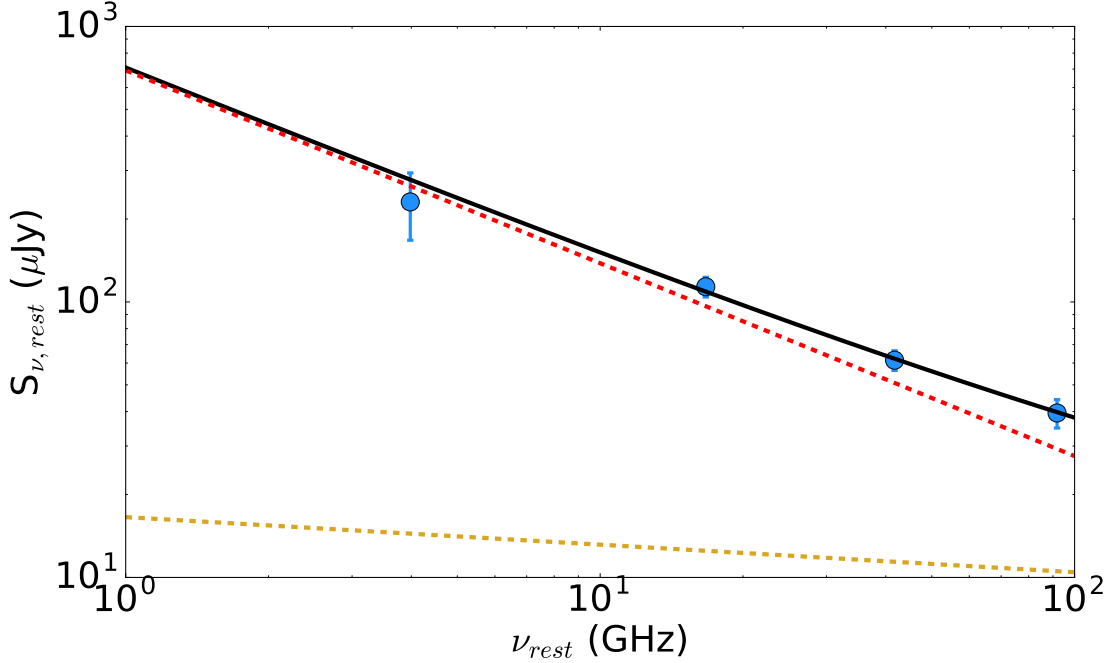


Figure 3.4 A plot showing the radio-SED decomposition for SDP.11. The blue points represent observed continuum flux values, with associated errors, while the black solid line is the best-fit model, composed of both thermal (gold dashed) and nonthermal (red dashed) components. At a rest-frame frequency of 3.98 GHz, the free-free contribution to the total radio emission is $\sim 5\%$.

interpret due to dust extinction:

$$\frac{N_{X^i}}{N_{H^+}} = \frac{F_\lambda}{S_{\nu,r}} \frac{3.485 \times 10^{-16} T_4^{-0.35} \nu_5^{-0.1}}{\epsilon_\lambda} \left(\frac{N_e}{N_p} \right) \quad (3.4)$$

Here, N_{X^i}/N_{H^+} is the abundance of ion i , relative to hydrogen, F_λ is the fine-structure line flux in units of $\text{erg s}^{-1} \text{cm}^{-2}$, $S_{\nu,r}$ is the rest-frame radio free-free flux at rest-frequency ν in units of Jy, T_4 is the electron temperature in units of 10^4 K , ν_5 is the radio emission frequency in units of 5 GHz, ϵ_λ is the emissivity per unit volume of the fine-structure line at wavelength λ , and N_e/N_p is the electron to proton number density ratio, which accounts for the contribution of electrons from non-hydrogen atoms present in the H II regions. We use the

collisional rate coefficients of [Palay et al. \(2012\)](#) for the [O III] lines and [Stafford et al. \(1994\)](#) for the [N III] line to calculate the corresponding emissivity values. We also assume $N_e/N_p = 1.05$, which accounts for the electrons contributed from helium, the second most abundant element, and $T_4 = 1$, a typical value for H II regions.

Using the measured [O III] 52 μm line flux and free-free flux density at 3.98 GHz, together with Equation 3.4, we calculate $[\text{O}^{++}/\text{H}] = 2.5 \times 10^{-4}$. Similarly, using the [N III] 57 μm line flux, we obtain $[\text{N}^{++}/\text{H}] = 4.9 \times 10^{-5}$. In addition to these numbers, an estimate of the fraction of O in the O⁺⁺ state and N in the N⁺⁺ state is required to scale back to the absolute abundances of oxygen and nitrogen.

In order to determine the $[\text{N}^{++}/\text{N}]$ and $[\text{O}^{++}/\text{O}]$ ratios, and hence scale our ionic abundance to total elemental abundances, an estimate for the hardness of the ambient radiation field within SDP.11 is required. While we do not have tight constraints on the hardness of the radiation field with our current observations, we can still make a reasonable estimate of the [N/O] abundance ratio in SDP.11. This is because the O⁺⁺ and N⁺⁺ ions have similar formation potentials (35.12 and 29.60 eV, respectively), such that the $[\text{N}^{++}/\text{N}]/[\text{O}^{++}/\text{O}]$ ratio is nearly independent of stellar effective temperature for a range of parameter space. The models of [Rubin \(1985\)](#) show that the $[\text{N}^{++}/\text{N}]/[\text{O}^{++}/\text{O}]$ ratio is nearly constant at a value of ~ 1.4 (within $\sim 50\%$) for $T_{eff} \gtrsim 33,000\text{K}$. Adopting this value and taking the ratio of $[\text{N}^{++}/\text{H}]/[\text{O}^{++}/\text{H}]$, calculated above, we estimate a [N/O] ratio of ~ 0.14 (again within $\sim 50\%$) in SDP.11, where solar is 0.138 ([Asplund et al., 2009](#)).

Similarly, [Nagao et al. \(2011\)](#) find that the [O III] (52 μm + 88 μm)/[N III] 57

μm ratio scales with gas-phase metallicity and is nearly independent of both gas density and hardness of the ambient radiation field. Our measured value of 5.4, nearly identical to their M82 value, corresponds to a gas-phase metallicity of $\sim 0.5 - 0.7 Z_{\odot}$, consistent with our above estimate.

Star Formation Rate

The star formation rate in SDP.11 — calculated by converting the FIR luminosity (Bussmann et al., 2013) to an IR luminosity assuming a bolometric conversion factor of 1.91 (Dale et al., 2001) and then applying the scaling of Kennicutt (1998) — is $\sim 11,400 \mu M_{\odot} \text{yr}^{-1}$ (uncorrected for lensing magnification). An independent estimate of the star formation rate is obtained from the free-free radio continuum. From Murphy et al. (2011):

$$\frac{SFR_{\nu,r}^T}{M_{\odot} \text{yr}^{-1}} = 4.6 \times 10^{-28} \left(\frac{T_e}{10^4 K} \right)^{-0.45} \left(\frac{\nu_r}{\text{GHz}} \right)^{0.1} \left(\frac{L_{\nu,r}^T}{\text{erg s}^{-1} \text{Hz}^{-1}} \right) \quad (3.5)$$

where T_e is the electron temperature, ν_r is the rest-frame frequency, and $L_{\nu,r}^T$ is the rest-frame thermal free-free luminosity at frequency ν . Calculating the star formation rate using the observations at 1.43 GHz, rest-frame 3.98 GHz, we obtain $\sim 1,700 \mu M_{\odot} \text{yr}^{-1}$ (uncorrected for lensing magnification). This value is a lower limit on the star formation rate in that it is based on the conversion of a star formation rate to the number of hydrogen-ionizing photons emitted by that stellar population, and then from the number of emitted hydrogen-ionizing photons to the observed free-free emission. Working backward, the conversion from observed radio free-free emission to hydrogen-ionizing photons should

be unaffected by extinction, by dust, for example; however the conversion from hydrogen-ionizing photons emitted by the stellar population to those that actually ionize hydrogen atoms can be affected by dust extinction, possibly contributing to the observed discrepancy. Additionally, the differences in the calculated star formation rates could indicate the presence of an AGN, which boosts the IR luminosity and artificially inflates the star formation rate derived from that quantity, while leaving the SFR calculated from the radio free-free emission, which is disentangled from the nonthermal AGN contribution, unaffected. Recently, X-Ray observations conducted with the Chandra X-Ray Observatory (Massardi et al., 2018), and dense-gas tracers observed with ALMA (Oteo et al., 2017), have both been detected to be cospatial with the peak of the dust continuum, suggesting the presence of an AGN within SDP.11, making this scenario plausible.

3.3.4 PDRs

[C II]/FIR Ratio

Photoelectric heating within PDRs is sensitive to the ratio of interstellar FUV radiation field strength and density (G_0/n) (e.g., Wolfire et al., 1990). The $L_{[C\text{ II}]} / L_{FIR}$ ratio is known to trace star formation intensity since it is sensitive to G_0 (e.g., Hailey-Dunsheath et al., 2010, Stacey et al., 1991, 2010c). This means that our spatially resolved ALMA [C II] $158\mu\text{m}$, and underlying continuum, maps of SDP.11 allow us to examine the variations in starforming intensity across this source.

Local ULIRGs have small [C II]/FIR ratios, $\lesssim 0.1\%$, indicating very strong

FUV fields ($G_0 \sim 1,000 - 10,000$ Habing units) and intense star formation activity consistent with collision-induced star formation confined to regions of order a few hundred parsecs in size (e.g., [Díaz-Santos et al., 2017](#)). In contrast, local star-forming galaxies, and many high-luminosity $z \sim 1 - 2$ galaxies, have higher [C II]/FIR ratios, indicating more modest FUV field intensities ($G_0 \sim 100 - 1,000$ Habing units) and star formation rates distributed over kiloparsec scales in the high-redshift cases (e.g., [Brisbin et al., 2015](#), [Stacey et al., 2010c](#)). Using our image-plane [C II]-emitting source size of ~ 1.9 square arcseconds, estimated from the ALMA map, and the average lensing magnification factor of 10.9 ([Bussmann et al., 2013](#)), we estimate an intrinsic source diameter of $\sim 0.5''$ (~ 4 kpc) for SDP.11, indicating extended star formation in this source. Using our spatially resolved [C II] 158 μm line observations, together with the continuum around the line, we additionally investigate the spatial variability of the [C II]/FIR ratio across SDP.11.

The L_{FIR} value per pixel was calculated by modeling the FIR SED of SDP.11 with a modified blackbody function, assuming a constant dust temperature of 41 K across the source and a dust emissivity index (β) of 1.5 (as was determined for SDP.11 using *SPIRE* photometry in [Bussmann et al., 2013](#)), such that the rest-frame 158 μm continuum flux scales directly to the FIR luminosity. Given that gravitational lenses are achromatic, the $L_{[\text{C II}]} / L_{\text{FIR}}$ ratio calculated pixel-by-pixel is expected to be unaffected by gravitational lensing, even though the lensing magnification factor may vary across the source. For this reason, we make no correction to this ratio for lensing effects.

We observe an $L_{[\text{C II}]} / L_{\text{FIR}}$ ratio of $\sim 0.02\%$ at the location of the peak of the dust continuum, which traces the most intense starbursting region. This low

ratio suggests conditions similar to those observed in the local merger-driven ULIRGs. The $L_{[C\,II]}/L_{FIR}$ ratio increases as we move azimuthally along the Einstein ring to up to $\sim 0.28\%$ (similar to that observed in the Milky Way, 0.3%). We note that, given the sensitivity of our observations, we only detect dust continuum from $\sim 40\%$ of the region that is significantly detected in [C II] line emission. As such, the $L_{[C\,II]}/L_{FIR}$ ratio in regions undetected in our continuum map would be higher than those seen in Figure 3.5. Given the ULIRG-like $L_{[C\,II]}/L_{FIR}$ ratios that are present in this source, we cannot rule out the possibility of a merger in SDP.11, even though the velocity profile of the [C II] line is consistent with a single rotating galaxy, with a compact continuum-emitting region in the center surrounded by a more extended, ~ 4 kpc diameter, [C II]-emitting region.

We additionally plot the $L_{[C\,II]}/L_{FIR}$ ratio vs. the star formation rate surface density (Σ_{SFR}), calculated using the L_{FIR} map described above, assuming a bolometric conversion factor from L_{FIR} to L_{IR} of 1.91 (Dale et al., 2001) and then applying the scaling of Kennicutt (1998). We then sample the map at a spatial resolution coarser than the beam to avoid correlated data points (e.g., we sample pixels from the map such that no selected pixel is within one beam width of any other selected pixel). We make no correction to the Σ_{SFR} value calculated per pixel for gravitational lensing, which conserves surface brightness (e.g., Σ_{SFR}). Fitting a power law to the plot of $L_{[C\,II]}/L_{FIR}$ vs. Σ_{SFR} , we find a power-law index of -0.7 (see Figure 3.6), indicating that the [C II] 158 μm emission increases more slowly than does L_{FIR} . This observed “[C II] deficit” is in good agreement with previous studies (e.g., Díaz-Santos et al., 2017, see Figure 3.6). This is because the [C II] line emission saturates at high UV fields, due both to the charging of grains, which reduces the efficiency of photoelectric heating of the gas, and the logarithmic growth of the C⁺ column with UV field strength

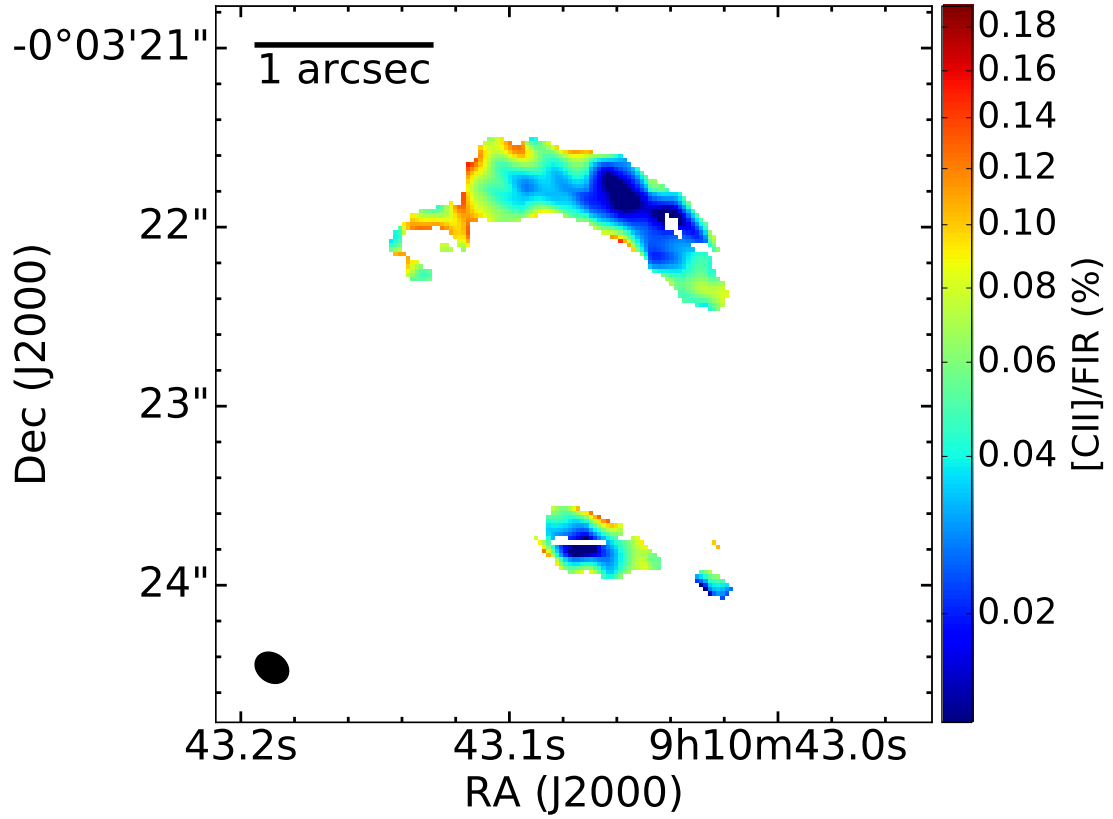


Figure 3.5 Color map of the $L_{[C\text{ II}]}/L_{\text{FIR}}$ ratio (plotted as a percentage) in SDP.11. The map is created by taking the ratio of the [C II] 158 μm moment-zero and L_{FIR} maps, the latter created using the 158 μm (rest-frame) continuum map and assuming a constant dust temperature across the source (see the text), at locations detected at a significance $> 3\sigma$ in both the line and continuum maps.

in the high-excitation limit, indicating that $L_{[C\text{ II}]}$ alone is not a good measure of star formation rate. The range of values calculated for $\Sigma_{\text{SFR}} \sim 65 - 630 M_{\odot} \text{ yr}^{-1} \text{ kpc}^{-2}$, is consistent with the source-averaged value of $10^{11.82} L_{\odot} \text{ kpc}^{-2}$ ($\sim 218 M_{\odot} \text{ yr}^{-1} \text{ kpc}^{-2}$) reported in [Bussmann et al. \(2013\)](#).

PDR Mass

We model the physical properties of the PDRs within SDP.11 using our opacity-corrected [C II] 158 μm and [O I] 63 μm line luminosities, together with the FIR

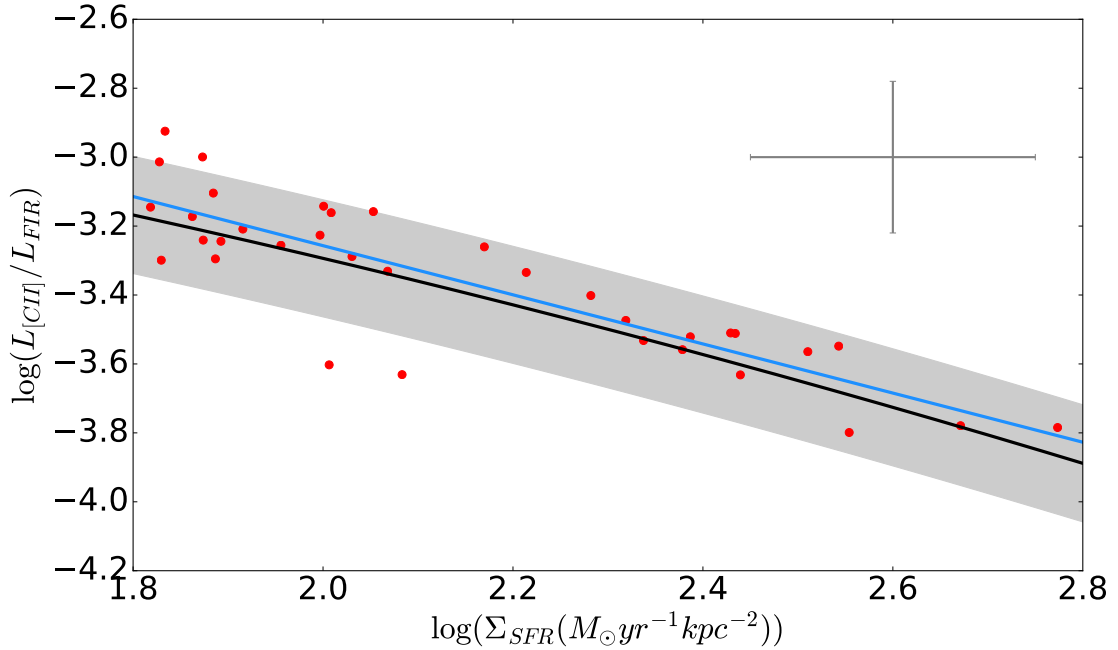


Figure 3.6 $L_{[C\text{ II}]} / L_{FIR}$ vs. the observed star-formation rate surface density (Σ_{SFR}) in SDP.11. The points come from sparsely sampling the 3σ -clipped ALMA [C II] 158 μm line and 158 μm (rest-frame) continuum maps at pixel separations greater than the beam size. The best-fit line (blue) has a power-law index of -0.7, indicating that L_{FIR} changes more quickly than does $L_{[C\text{ II}]}$. This is because the [C II] line emission saturates at high UV fields (see the text). The black line with shaded 1σ error bounds is the best fit from [Díaz-Santos et al. \(2017\)](#), obtained for a sample of local ULIRGs. The gray error bars are representative of the worst-case error in the plot (a 3σ detection in both the continuum and [C II] line) and are correspondingly smaller for locations detected at larger significance.

continuum luminosity ([Bussmann et al., 2013](#)), utilizing the PDR Toolbox ([Kaufman et al., 2006](#), [Pound & Wolfire, 2008](#)). We obtain values of $G_0 \sim 1,800$ Habing units and $n \sim 1,000 \text{ cm}^{-3}$, with a PDR surface temperature of $\sim 370 \text{ K}$.

Using the calculated n , G_0 , and PDR surface temperature values in SDP.11,

we can estimate the PDR mass following Hailey-Dunsheath et al. (2010):

$$\frac{M_{PDR}}{M_\odot} = 0.77 \left(\frac{0.7L_{[C\text{II}]}}{L_\odot} \right) \left(\frac{1.4 \times 10^{-4}}{X_{C^+}} \right) \times \frac{1 + 2 \exp(-\frac{-91K}{T}) + \frac{n_{crit}}{n}}{2 \exp(-\frac{-91K}{T})}, \quad (3.6)$$

where X_{C^+} is the abundance of C^+ per hydrogen atom, taken here to be 1.4×10^{-4} (Savage & Sembach, 1996), n_{crit} is the critical density of the [C II] 158 μm transition ($2,800 \text{ cm}^{-3}$, Stacey, 2011), and assuming that $\sim 70\%$ of the [C II] emission originates within PDRs. We calculate a PDR gas mass of $\sim 3.7 \times 10^9 M_\odot$ after correcting for the average lensing magnification factor of 10.9 (Bussmann et al., 2013).

Molecular Gas

The molecular gas in SDP.11 has been observed in several mid-J CO lines, (J_{upper} , J_{lower}) = (4-3), (5-4), (6-5), (7-6) (Lupu et al., 2012, Oteo et al., 2017). We can estimate the molecular gas mass within SDP.11 by calculating $L'_{CO(4-3)}$, using the measurements from Oteo et al. (2017), assuming an SMG CO excitation of $r_{43/10} = 0.41$ (Bothwell et al., 2013), and taking a ULIRG value of $\alpha_{CO} = 0.8 M_\odot (\text{K km s}^{-1} \text{ pc}^2)^{-1}$ (e.g., Bolatto et al., 2013). We obtain $L'_{CO(4-3)} = 9.2 \times 10^{10} \text{ K km s}^{-1} \text{ pc}^2$ (uncorrected for lensing), such that the molecular gas mass is $\sim 1.6 \times 10^{10} M_\odot$, after correcting for the average gravitational lensing magnification factor of 10.9 (Bussmann et al., 2013). This calculated molecular gas mass is $\sim 5\times$ larger than the PDR gas mass estimated above, making the mass ratio consistent with that observed in other starburst galaxies (e.g., Stacey et al., 1991), and is $\sim 10\times$ larger than the estimated ionized gas mass, consistent with ratios observed in

both high-redshift (e.g., Ferkinhoff et al., 2011) and nearby galaxies (e.g., Lord et al., 1996, Wild et al., 1992). With the intrinsic star formation rate of SDP.11 ($\sim 1,000 M_{\odot} \text{yr}^{-1}$), this molecular gas reservoir will be depleted within ~ 16 Myr. If, instead, we assume the CO excitation of SDP.9 from Oteo et al. (2017), which is more highly excited than is the SMG CO SLED from Bothwell et al. (2013), the depletion timescale for the gas in SDP.11 becomes even shorter.

3.3.5 Lens Modeling

In order to recover the source-plane morphology, velocity structure, and any potential differential lensing, we perform gravitational lens modeling on the ALMA [C II] 158 μm line observations of SDP.11 using the code UVMCMCFIT (Bussmann et al., 2015). This code models the foreground lensing galaxy using a single isothermal ellipsoid (SIE) profile, which has five free parameters: the offset in both R.A. and decl. from the user-defined center of the coordinate system, and the Einstein radius, axial ratio, and position angle of the lens. The lensed background source is modeled using a single elliptical Gaussian and is parameterized by six free parameters: the offset in both R.A. and decl. from the center of the user-defined coordinate system and the intrinsic flux, axial ratio, effective radius, and position angle of the source. It then uses Markov Chain Monte Carlo (MCMC) to sample the parameter space, determining the best-fit parameters and associated uncertainties. For a more complete description of the code, see Bussmann et al. (2015).

Before performing the gravitational lens modeling of SDP.11 using the [C II] 158 μm line, we create two moment-zero maps: one containing the red portion

Table 3.3. Best-fit gravitational-lensing parameters for SDP.11

Parameter	Red Comp.	Blue Comp.
$\delta R.A._{Lens}$ (")	0.064 ± 0.008	$0.064 \pm 0.008^*$
$\delta Dec._{Lens}$ (")	0.016 ± 0.008	$0.016 \pm 0.008^*$
Axial Ratio _{Lens}	0.65 ± 0.01	$0.65 \pm 0.01^*$
P.A. _{Lens} (deg)	128 ± 2	$128 \pm 2^*$
$R_{Einstein}$ (")	1.003 ± 0.004	$1.003 \pm 0.004^*$
$\delta R.A._{Source}$ (")	-0.048 ± 0.007	-0.046 ± 0.006
$\delta Dec._{Source}$ (")	-0.045 ± 0.007	0.318 ± 0.005
Axial Ratio _{Source}	0.60 ± 0.02	0.48 ± 0.02
P.A. _{Source} (deg)	62 ± 3	74 ± 2
$R_{Eff,Source}$ (")	0.176 ± 0.003	0.166 ± 0.005
μ	11.5 ± 0.2	6.2 ± 0.1

Note. — The red comp. and blue comp. column headings refer to the red and blue velocity components of the [C II] 158 μm line, centered at $v = 155 \text{ km s}^{-1}$ and $v = -155 \text{ km s}^{-1}$, respectively (where $v = 0 \text{ km s}^{-1}$ corresponds to $z = 1.7830$). “Lens” subscripts refer to properties of the foreground lensing galaxy, while “source” subscripts refer to properties of the background, lensed, galaxy (SDP.11). The positions of the sources, $\delta R.A._{Source}$ and $\delta Dec._{Source}$, are given relative to the best-fit lens position, while the lens position, $\delta R.A._{Lens}$ and $\delta Dec._{Lens}$, is given relative to the optical centroid of the foreground lensing galaxy ($9^h10^m43^s.07$, $-00^\circ03'22''.91$). $R_{Eff,Source}$ is the effective radius of the source in the source-plane. μ is the gravitational lensing magnification factor. See Section 3.5 for further information on the fitting procedure.

*The best-fit foreground lens properties obtained from the red component fit are fixed for the blue component fit to ensure consistency (see the text for further explanation).

of the line, centered at $v = 155 \text{ km s}^{-1}$, and the other containing the blue portion of the line, centered at -155 km s^{-1} (where $v = 0 \text{ km s}^{-1}$ corresponds to $z = 1.7830$). Each moment-zero map is collapsed over 300 km s^{-1} in the velocity dimension.

Given that the red component of the line is observed to be much brighter than the blue component, and hence detected at much higher significance, we perform lens modeling on that component first, requiring that the foreground lensing galaxy be located within $\pm 0''.2$ of the centroid of the known optical source ($9^h10^m43^s.07$, $-00^o03'22''.91$) obtained from Hubble imaging. We then model the blue component of the line, using the best-fit lens parameters obtained from the red component fit (e.g., we require that both velocity components of the [C II] line are lensed by a common foreground lensing potential). See Table 3.3 for the gravitational lensing best-fit parameters and Figure 3.7 for the model images.

We find that both components of the [C II] line are well fit by a single gravitational lens located at the position of the known optical source. We further find that differential lensing is present with this lensing configuration, varying from $\mu = 11.5 \pm 0.2$ for the red component of the line to $\mu = 6.2 \pm 0.1$ for the blue component. After correcting for this differential lensing, the [C II] $158 \mu\text{m}$ line profile becomes much more symmetric (see Figure 3.8).

Dye et al. (2014) generated a pixelated reconstruction of SDP.11, based on the observed stellar emission, using an enhanced version of the semilinear inversion method (e.g., Warren & Dye, 2003) in the image-plane. They found that a significant external shear component, $\gamma = 0.23 \pm 0.1$, was required to describe the ellipticity of the lensed ring. This shear is attributed to a nearby edge-on spi-

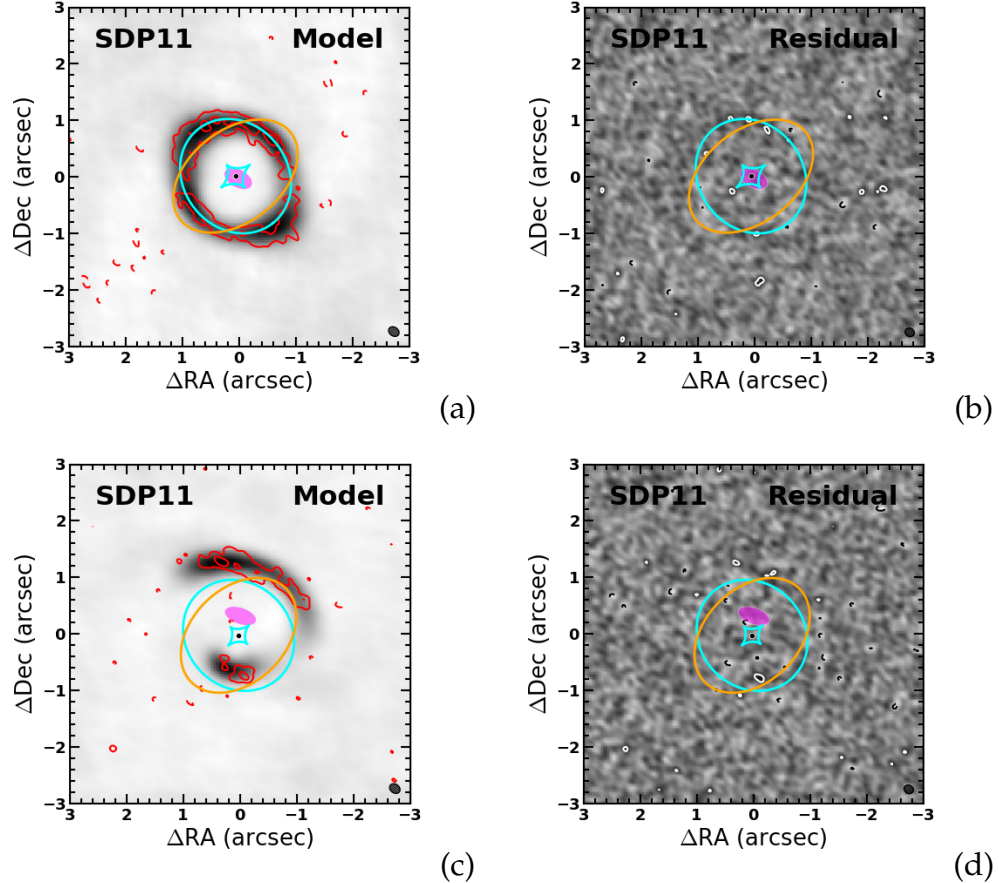


Figure 3.7 (a) Gravitational lens model of the red component ($v = 155 \text{ km s}^{-1}$) of the [C II] $158 \mu\text{m}$ line in SDP.11, created using the code UVMCMCFIT (Bussmann et al., 2015). The red contours show the [C II] $158 \mu\text{m}$ line emission, while the grayscale image is the best-fit model. The position of the foreground lensing galaxy is represented by a black dot, with its critical curve shown in orange. The half-light ellipse of the source is shown in magenta, with the caustic curve in cyan. (b) Residual map for the model shown in (a). Contours are plotted in steps of 3σ . Panels (c) and (d) are the same as (a) and (b), but for the blue component (-155 km s^{-1}) of the [C II] $158 \mu\text{m}$ line.

ral galaxy located $\sim 4''.4$ to the NW of SDP.11. [Dye et al. \(2014\)](#) also vary the mass distribution of the foreground lensing galaxy to determine its mass-density profile. We built upon the lens model presented in [Bussmann et al. \(2013\)](#), based on the thermal dust emission, using the same code, UVMCMCFIT. This code uses the complete information from the visibilities sampled in the uv-plane to model the observed lensing configuration. At present, UVMCMCFIT has neither the ability to include external shear, nor the ability to vary the mass-density profile of the foreground lensing galaxy. A more detailed lens model is beyond the scope of this paper and will be the focus of future work.

If we assume that the [C II] line is indeed emitted from a rotating disk in the case of SDP.11, our gravitational lens modeling predicts that the diameter of that disk, determined from the separation of the red and blue line-emitting regions in the source-plane, is $\sim 0''.4$ or, equivalently, ~ 3.5 kpc. This is consistent with the intrinsic source size estimated in section 3.4.1 from the [C II] image-plane source size and source-averaged gravitational lensing magnification factor.

Additionally, taking the separation between the red and blue [C II] line-emitting regions, and assuming a disk geometry, we can estimate the dynamical mass of SDP.11. For circular orbits:

$$M_{dyn} = \frac{v_{rot}^2 r}{G}, \quad (3.7)$$

where v_{rot} is the true rotational velocity of the disk, estimated from the observed velocity by correcting for the average inclination angle, $\langle v_{rot} \rangle \sim \frac{\pi}{2} v_{obs}$ (e.g., [Erb et al., 2006](#)), r is the radius of the galaxy, and G is the gravitational constant. We estimate the radius from our gravitational lens modeling as half of the

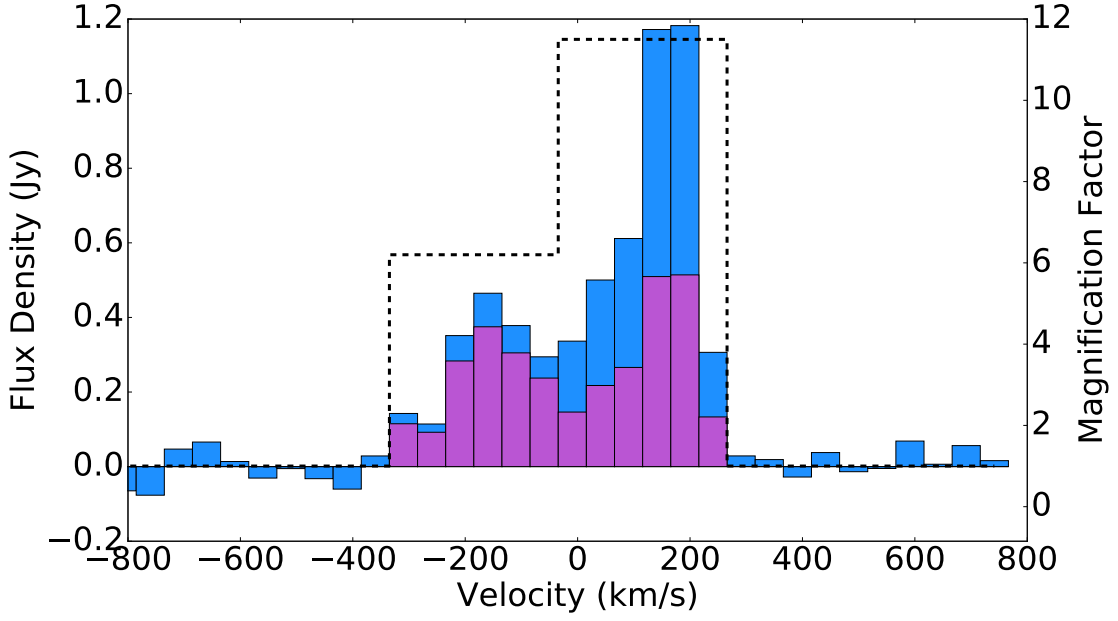


Figure 3.8 Lens-corrected, source-integrated, ALMA [C II] 158 μm spectrum of SDP.11 (purple), scaled up by a factor of 5x for clarity. The lens-corrected spectrum is obtained by dividing the observed spectrum (blue) by the best-fit magnification factors (black dashed line) obtained using the code UVMCMCFIT (Bussmann et al., 2015). Differential lensing is present for the lensing configuration seen here, with the magnification factor varying from ~ 6.2 to 11.5 across the source. After correcting for differential lensing, a more symmetric line profile is recovered.

distance between the red and blue line-emitting regions (1.75 kpc). Similarly, we take half of the velocity separation between our blue and red line components, 155 km s^{-1} , to be the observed rotational velocity. We obtain a dynamical mass of $\sim 2.4 \times 10^{10} M_{\odot}$. While this dynamical mass estimate depends on the assumed inclination angle of the source, taken here to be the average value, it suggests that the reported value of the stellar mass within SDP.11, $\sim 1.9 \times 10^{11} M_{\odot}$ (Negrello et al., 2014), may be an overestimate, potentially due to contamination of the optical light by an AGN.

3.4 Conclusions

We have mapped the [C II] 158 μm line in SDP.11, a strongly-lensed galaxy at redshift 1.7830, at 0''.2 resolution (source-plane ~ 500 pc), using ALMA. At this resolution, the image of the gravitationally-lensed source is resolved into two spatially and velocity offset Einstein rings on the sky. This dataset showcases the ability of ALMA to perform high-frequency observations of high-redshift galaxies and is one of only a handful of such results available in the literature. We have also presented detections of the [O III] 52 μm , [O I] 63 μm , and [N III] 57 μm lines observed with *Herschel/PACS*.

Using the ionized gas lines from *Herschel*, we have modeled the H II regions of SDP.11, finding that they are heated by a starburst headed by stars hotter than spectral type B0. This stellar population constrains the age of the starburst to be $\lesssim 8$ Myr.

Combined with multiband radio continuum measurements, which allow us to disentangle the free-free and nonthermal contributions to the radio SED, the ionized gas lines that we detect with *Herschel* have allowed us to estimate the gas-phase metallicity within SDP.11. We find that the [N/O] abundance ratio in SDP.11 is consistent with solar metallicity.

Examining the [C II]/FIR ratio map of SDP.11, we find that the mean value is consistent with that of local ULIRGs, suggesting an intense starburst. We further find that the variation in the $L_{[\text{C II}]}/L_{\text{FIR}}$ ratio across SDP.11, when plotted against Σ_{SFR} , is best-fit with a power law of index -0.7, indicating that the [C II] 158 μm emission increases more slowly than does L_{FIR} , leading to the observed “[C II] deficit.”

We have modeled the gravitational lensing configuration present for SDP.11 using the code UVMCMCFIT, finding that the position of the lens is cospatial with a known optical source, in agreement with previous lens modeling. We further find differential lensing across SDP.11, with the lensing magnification factor varying from ~ 6.2 to 11.5 across the source. After correcting for the effects of differential lensing, a more symmetric profile is recovered for the [C II] line, indicating that the starburst present here need not be the result of a major merger, with a compact starbursting region located at the center, as is the case for local ULIRGs, but may instead be star formation extended across a ~ 3.5 kpc rotating disk. A more detailed study of the gravitational lensing present for this source will be the subject of a future paper.

We have estimated the ionized, PDR, and molecular gas masses in SDP.11, finding that the proportions are consistent with those of other starburst galaxies. We have additionally estimated the dynamical mass of SDP.11, finding that the previously reported stellar mass may be an overestimate, potentially due to contamination of the optical emission, attributed previously to stellar light, from an AGN.

We have recently been awarded ALMA time to map the [C I] 609 and $370\mu\text{m}$ lines, as well as the CO(4-3) and CO(7-6) lines, within SDP.11, at comparable spatial resolution to the [C II] map presented here, to further study the molecular and neutral gas within this source. Specifically, these observations will yield the spatially resolved gas temperature, [C I] $370/609\mu\text{m}$, and CO excitation, CO(7-6)/CO(4-3), across the source, allowing for PDR modeling on subkiloparsec scales of SDP.11 at redshift ~ 1.8 .

CHAPTER 4

CO AND FINE-STRUCTURE LINES REVEAL LOW METALLICITY IN A STELLAR-MASS-RICH GALAXY AT $z \sim 1$?

*C. Lamarche, G. J. Stacey, A. Vishwas, D. Brisbin, C. Ferkinhoff, T. Nikola,
S. J. U. Higdon, J. Higdon*

Accepted For Publication In The Astrophysical Journal

4.1 Introduction

Recent studies have made great strides in inventorying molecular gas, the fuel for star formation, in galaxies during the peak epoch of cosmic star formation, redshift (z) ~ 1 -3, in an effort to determine the efficiency with which these galaxies convert their molecular gas reservoirs into stars (e.g., Harrington et al., 2018, Harris et al., 2012, Pavesi et al., 2018, Sharon et al., 2016, Tacconi et al., 2010). These surveys are complicated by the fact that hydrogen, whose lowest rotational transition takes ~ 500 K to excite, is difficult to observe in cold molecular clouds, so that the easily-excited low-J rotational levels of carbon-monoxide (CO) are generally used as a proxy for molecular gas content. Under some interstellar medium (ISM) conditions however, appreciable amounts of molecular hydrogen are not accompanied by CO. These so-called “CO-dark” molecular clouds are troublesome in that they cause galaxies containing them to appear very gas poor when employing CO-derived gas-mass estimates. Several possible explanations for these CO-dark molecular clouds exist, including low-metallicity gas present within the ISM of galaxies (e.g., Maloney & Black, 1988, Stacey et al., 1991) and highly-fractionated molecular clouds (e.g., Stoerzer et al.,

1997). Here we investigate one such CO-dark galaxy, 3C 368 (e.g., Evans et al., 1996, Lamarche et al., 2017), which has an appreciable star-formation rate and seemingly very little molecular gas.

3C 368 was discovered as part of the Third Cambridge Radio Catalog (Edge et al., 1959) and has come to be known as one of the archetypal Fanaroff-Riley class II (FR-II) galaxies. It is an interesting source, situated within the peak epoch of cosmic star-formation, forming stars at a rate of $\sim 350 M_{\odot} \text{ yr}^{-1}$ (Podigachoski et al., 2015), and containing an active galactic nucleus (AGN) that has launched radio-emitting lobes which span $\sim 73 \text{ kpc}$ (Best et al., 1998a).

In Lamarche et al. (2017) we used both mid- and far-infrared (FIR) fine-structure line observations of 3C 368 to infer the age of the young stellar component present within the source, finding an age of $\sim 6.5 \text{ Myrs}$, consistent with that determined using a multi-component model for the observed UV-FIR spectral energy distribution (SED) (Drouart et al., 2016). We also presented a non-detection of the CO(2-1) line, constraining the CO luminosity to a level twelve times lower than expected in star-forming galaxies, based on standard ratios with the [C II] 158 μm line (e.g., Stacey et al., 1991), which we attributed to either a low-metallicity or highly-fractionated interstellar medium (ISM). In this follow-up paper, we present observations of the CO(4-3) and [C I](1-0) 609 μm spectral lines, which emanate from molecular clouds and photo-dissociation regions (PDRs), respectively, as well as the dust continuum emission at 480.5 GHz (rest-frame), in 3C 368, and show how these measurements help us to disentangle these two competing scenarios.

We assume a flat Λ CDM cosmology, with $\Omega_M = 0.27$, $\Omega_{\Lambda} = 0.73$, and $H_0 = 71 \text{ km s}^{-1} \text{ Mpc}^{-1}$, throughout this paper (Spergel et al., 2003).

4.2 Observations and Data Reduction

4.2.1 ALMA

The CO(4-3) and [C I] 609 μm lines were observed simultaneously in 3C 368, using the Atacama Large Millimeter/submillimeter Array (ALMA)¹ band-6 receivers. The observations were split into two separate execution blocks: the first conducted on June 3, 2016, with a precipitable water vapor (PWV) measurement of 1.24 mm and baselines up to 772 m, and the second conducted on August 20, 2016, with a PWV of 0.31 mm and baselines up to 1462 m. The total on-source integration time for these two observations was ~ 1 hour and 40 minutes.

For both execution blocks, J1751+0939 (PKS 1749 +096) was used as the band-pass, flux, and phase calibrator. The data from the two execution blocks were reduced using the Common Astronomy Software Application (CASA)² ALMA pipeline, version 38366 (C4 — R2B), run in CASA version 4.7.0, and subsequently combined, imaged, and cleaned, using CASA version 4.7.2.

Imaging the CO(4-3) measurement set at a spectral resolution of 60 km s^{-1} , and employing a robust parameter of 0.5, we obtain an RMS sensitivity of 120 $\mu\text{Jy beam}^{-1}$ in each spectral channel, with a synthesized beam of size $0''.41 \times 0''.31$.

The [C I] 609 μm measurement set was similarly imaged at 60 km s^{-1} spectral resolution, employing a robust parameter value of 0.5. Here we obtain an RMS sensitivity of 130 $\mu\text{Jy beam}^{-1}$ in each spectral channel, with a synthesized beam

¹The National Radio Astronomy Observatory is a facility of the National Science Foundation operated under cooperative agreement by Associated Universities, Inc.

²<https://casa.nrao.edu/>

of size $0''.39 \times 0''.29$.

A continuum image was created by combining the two line-free spectral windows present in the measurement set, for a total continuum bandwidth of ~ 4 GHz, centered at 225.5 GHz (observed-frame). Imaging with a robust parameter value of 0.5, as was done for the line data, we obtain an RMS noise of $13 \mu\text{Jy beam}^{-1}$, with a beam of size $0''.38 \times 0''.29$.

4.3 Results and Discussion

4.3.1 Line and Continuum Fluxes

Both the CO(4-3) and [C I] 609 μm lines are well detected in our ALMA observations, emanating from the core component of 3C 368. A continuum-subtracted moment-zero map was created for each of the two spectral lines (see Figure 4.1), with the corresponding line fluxes determined by fitting a two-dimensional Gaussian to the emitting region of each moment-zero map. We obtain a CO(4-3) line flux of $1.08 \pm 0.14 \text{ Jy km s}^{-1}$, or equivalently $(7.8 \pm 1.0) \times 10^{-21} \text{ W m}^{-2}$, and a [C I] 609 μm line flux of $0.85 \pm 0.09 \text{ Jy km s}^{-1}$, or equivalently $(6.6 \pm 0.7) \times 10^{-21} \text{ W m}^{-2}$. These fluxes were verified by numerically integrating the spectra extracted from an aperture containing the core of 3C 368 (see Figure 4.3) and were found to be consistent within the quoted uncertainties.

The continuum in 3C 368 is resolved into three components in the 225.5 GHz (observed-frame) map: the northern lobe at $226 \pm 59 \mu\text{Jy}$, the southern lobe at $128 \pm 28 \mu\text{Jy}$, and the core at $96 \pm 21 \mu\text{Jy}$ (see Figure 4.2), where these flux densi-

ties were determined by fitting a two-dimensional Gaussian to each component in the continuum image. We note that continuum flux extended around the core component of 3C 368 at the same spatial scales as the [C I] and CO emission could be resolved out at the resolution and sensitivity of our observations, making the quoted flux density from the core a lower limit on the true value.

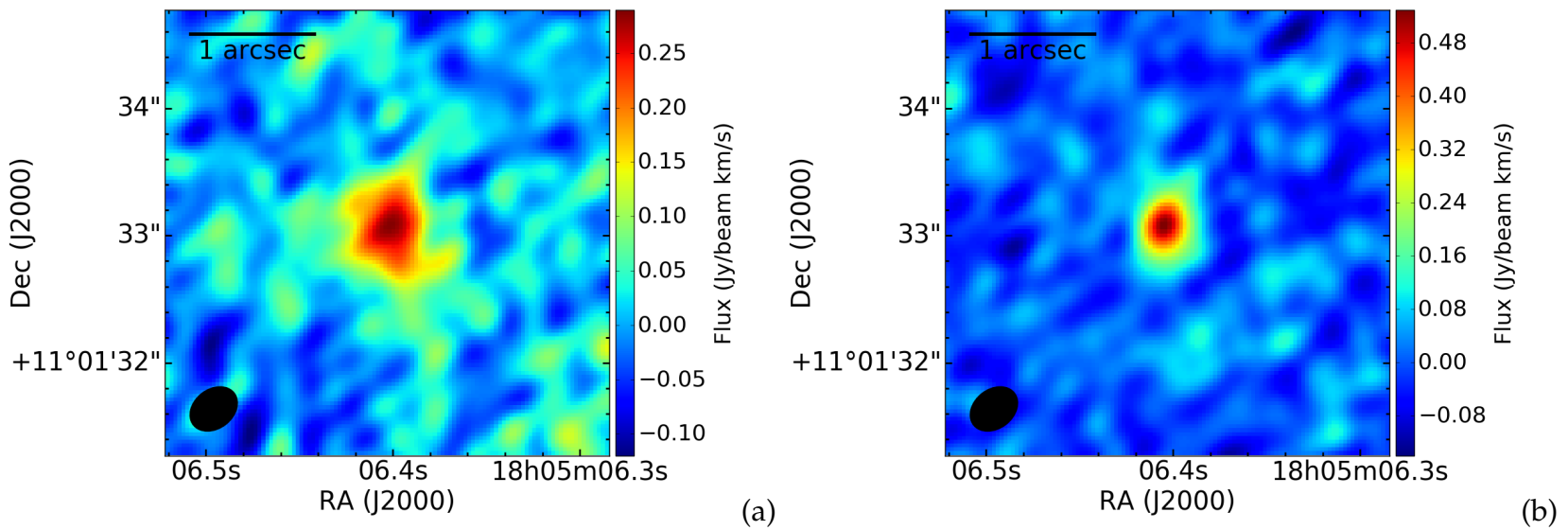


Figure 4.1 (a) ALMA CO(4-3) moment-zero map showing the core component of 3C 368 at 0''.4 resolution. The CO-emitting source has a size of $0''.77 \times 0''.46$, deconvolved from the beam. (b) ALMA [C I] 609 μm moment-zero map showing the same region of 3C 368 at 0''.4 resolution. The deconvolved [C I]-emitting source size is $0''.43 \times 0''.23$.

Table 4.1. Spectral-line and continuum observations of 3C 368

Observation	Core	N. Lobe	S. Lobe	Unit
CO(4-3)	7.8 ± 1.0	-	-	$F_{obs} (10^{-21} \text{ W m}^{-2})$
"	4.6 ± 0.6	-	-	$L' (10^9 \text{ K km s}^{-1} \text{ pc}^2)$
[C I](1-0)	6.6 ± 0.7	-	-	$F_{obs} (10^{-21} \text{ W m}^{-2})$
"	3.2 ± 0.3	-	-	$L' (10^9 \text{ K km s}^{-1} \text{ pc}^2)$
Continuum ($\nu_{obs} = 225.5 \text{ GHz}$)	96 ± 21	226 ± 59	128 ± 28	$S_{\nu,obs} (\mu\text{Jy})$

Note. — These flux and flux-density values were determined by fitting two-dimensional Gaussian profiles to the respective maps for each of the source components within 3C 368 (see the text).

4.3.2 Continuum Science

Spectral Energy Distribution

Using the ALMA continuum observations centered at 480.5 GHz (rest-frame) presented here, together with our previous ALMA continuum measurements at 205 μm (rest-frame; Lamarche et al., 2017), we can calculate the slope of the Rayleigh-Jeans power-law for the thermal dust continuum of 3C 368. This is particularly interesting in this case, since the core component of 3C 368, the star-forming galaxy, makes up the smallest contribution to the continuum flux at rest-frame 480.5 GHz, the flux being dominated instead by the radio lobes. Hence, unresolved continuum measurements at mm/sub-mm wavelengths may have overestimated the flux from the core of 3C 368. We obtain a Rayleigh-Jeans power-law index, $S_\nu \sim \nu^\alpha$, of 3.7 ± 0.4 , or equivalently a dust-emissivity β value, $S_\nu \sim \nu^{2+\beta}$, of 1.7 ± 0.4 . This is consistent with the dust-

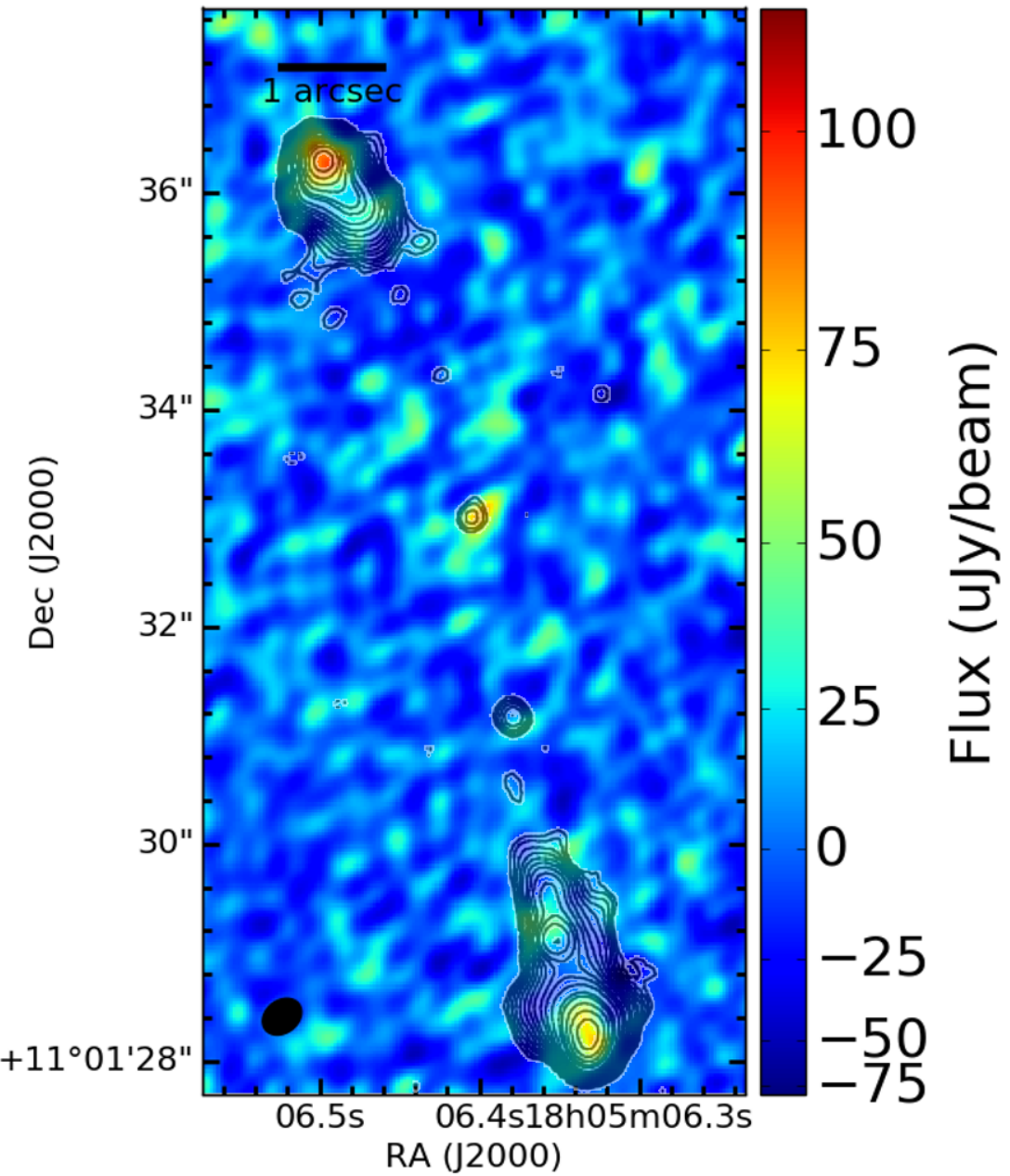


Figure 4.2 ALMA 225.5 GHz (observed-frame) continuum colormap of 3C 368 at $0''.4$ resolution. The source is resolved into three components: a core, a northern lobe, and a southern lobe, co-spatial with those seen in 8.21 GHz (observed-frame) radio-continuum emission (contour map; Best et al., 1998a). The core component of 3C 368 is unresolved at this resolution and sensitivity.

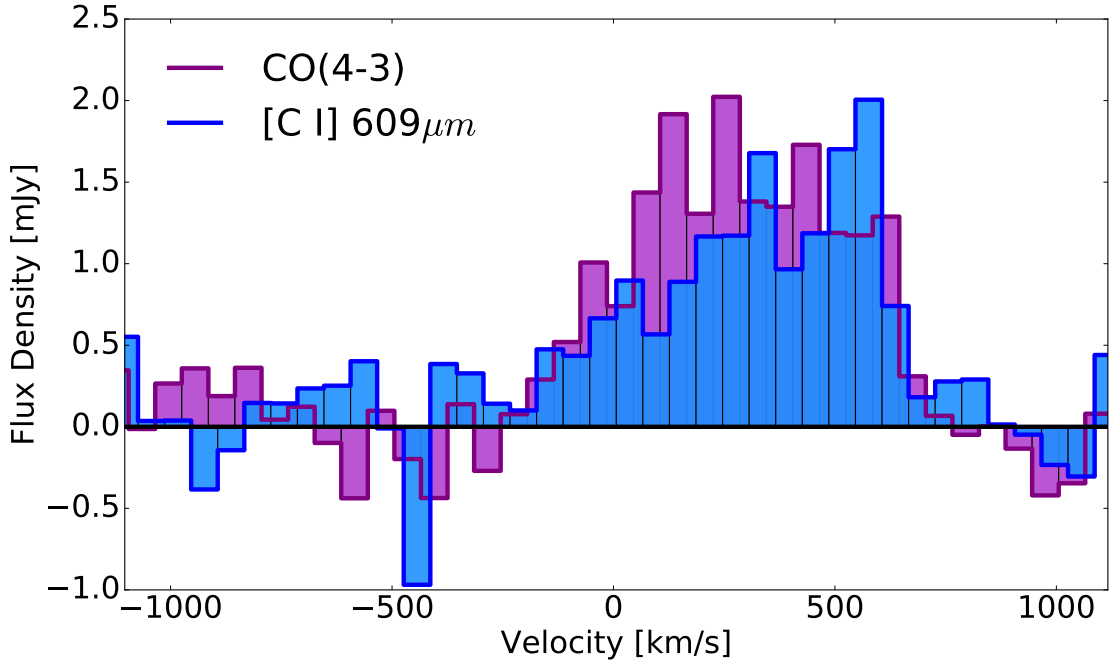


Figure 4.3 Continuum-subtracted ALMA spectra of both the CO(4-3) and [C I] $609\mu\text{m}$ lines extracted from the core component of 3C 368. $v = 0$ corresponds to $z = 1.131$.

emissivity β value assumed in [Podigachoski et al. \(2015\)](#), who used that value to derive an FIR luminosity of $2.0 \times 10^{12} L_{\odot}$, which we used in our previous work and will adopt throughout this paper.

We can also decompose the radio spectral energy distribution (SED) from the core of 3C 368 into thermal and nonthermal components, using our previous ALMA 230 GHz (rest-frame) continuum observations ([Lamarche et al., 2017](#)), together with radio continuum observations at 8.21 and 4.71 GHz (observed-frame) ([Best et al., 1998a](#)), using an equation of the following form (e.g., [Condon, 1992](#), [Klein et al., 2018](#)):

$$S_{total,r} = S_{th,0,r} \left(\frac{\nu}{\nu_{0,r}} \right)^{-0.1} + S_{nth,0,r} \left(\frac{\nu}{\nu_{0,r}} \right)^{-\alpha_{nth}} \quad (4.1)$$

where $S_{th,0,r}$ and $S_{nth,0,r}$ are the (rest-frame) contributions to the total radio flux from the thermal and nonthermal components, respectively, at $\nu_{0,r}$ (rest-frame), and α_{nth} is the nonthermal power-law index. Adopting a $\nu_{0,r}$ value of 230 GHz and holding α_{nth} fixed at 0.7 (e.g., Shu, 1991), we fit for $S_{th,0,r}$ and $S_{nth,0,r}$. We find best-fit values of $S_{th,0,r} = 45 \pm 18 \mu\text{Jy}$ and $S_{nth,0,r} = 4 \pm 3 \mu\text{Jy}$ (see Figure 4.4).

We do not consider any contribution to this part of the SED from thermal dust emission, which, continuing the Rayleigh-Jeans power-law found above, would contribute only $\sim 5\%$ of the flux measured at 230 GHz (rest-frame). Indeed, the continuum flux from the core of 3C 368 is observed to be brighter at rest-frame 230 GHz than at rest-frame 480.5 GHz, indicating that the dominant emission mechanism at 230 GHz is not thermal dust – an inference made possible by the continuum observations presented here.

Beyond the core component of 3C 368, we note that the radio lobes have considerable emission even in the high-frequency observations presented here (rest-frame 480.5 GHz). Between observed-frame 8.21 and 4.71 GHz, Best et al. (1998a) find a spectral index, $S_\nu \sim \nu^\alpha$, of ~ -1.5 for both the northern and southern radio lobes. While the flux densities at rest-frame 480.5 GHz fall below the extrapolated power-law values, by factors of ~ 1.4 and 2.3 for the northern and southern lobes, respectively, the fact that such energetic electrons are present within the radio-emitting lobes is noteworthy. While detailed modeling is beyond the scope of this paper, the observations presented here suggest that the radio-emitting lobes of 3C 368 are quite young (e.g., Murgia et al., 1999).

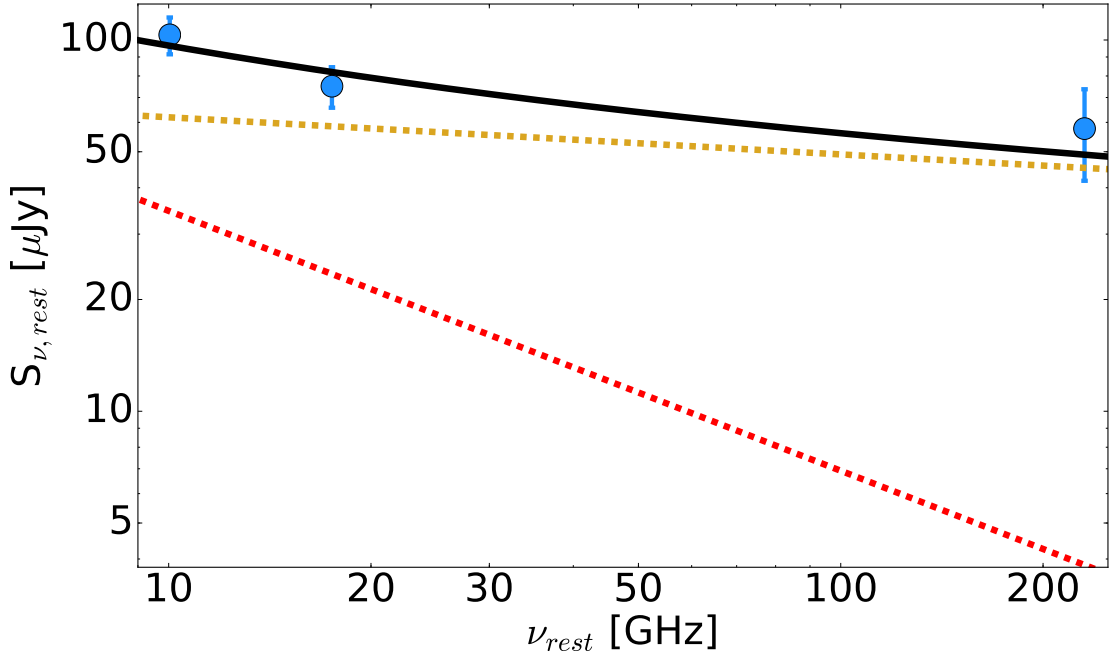


Figure 4.4 Radio SED of the core component of 3C 368, decomposed into thermal (gold) and non-thermal (red) contributions. Data from Best et al. (1998a) and Lamarche et al. (2017).

Metallicity From Free-Free Continuum and Far-IR Fine-Structure Lines

Having determined that the radio SED of the star-forming core of 3C 368 is dominated by thermal free-free continuum at 230 GHz (rest-frame), we can estimate the gas-phase oxygen abundance in 3C 368 using our previous observations of the [O III] 52 μm line (Lamarche et al., 2017).

The method for determining gas-phase absolute ionic abundances using fine-structure line emission and radio free-free continuum has been applied historically to galactic H II regions (e.g., Herter et al., 1981, Rudolph et al., 1997) and more recently to high-redshift galaxies (e.g., Lamarche et al., 2018). This technique provides an alternative to optically-derived metallicities, which suffer both from uncertainties in the temperature structure of H II regions, as well as dust extinction of the line flux. Dust obscuration is important in the local

Universe, especially in the more luminous star-forming galaxies, and becomes an increasingly important effect in the epoch of peak cosmic star formation, at redshift $\sim 1 - 3$. It can be shown that the abundance of ion X^{i+} , relative to hydrogen, is given by:

$$\frac{n_{X^{i+}}}{n_{H^+}} = \frac{F_\lambda}{S_{\nu,r}} \frac{4.21 \times 10^{-16} T_4^{-0.35} \nu_9^{-0.1}}{\epsilon_\lambda} \left(\frac{n_e}{n_p} \right) \quad (4.2)$$

where F_λ is the fine-structure line flux in units of $\text{erg s}^{-1} \text{cm}^{-2}$, $S_{\nu,r}$ is the rest-frame radio free-free flux density at rest-frequency ν in units of Jy, T_4 is the electron temperature in units of 10^4 K, ν_9 is the radio emission rest-frequency in units of GHz, n_e/n_p is the electron to proton number density ratio, which accounts for the contribution of electrons from non-hydrogen atoms present in the H II regions, and ϵ_λ is the emissivity per unit volume of the fine-structure line at wavelength λ , given by:

$$\epsilon_\lambda = \frac{j_{ul}}{n_i n_e} = \frac{h \nu_{ul} A_{ul} n_u}{n_e n_i}, \quad (4.3)$$

where h is the Planck constant, A_{ul} is the Einstein A coefficient for the line transition at frequency ν_{ul} , $9.8 \times 10^{-5} \text{ s}^{-1}$ and 5785.9 GHz, respectively, for the [O III] 52 μm line (Carilli & Walter, 2013), and the ratio of the level population in the upper state (n_u) to the total (n_i) is determined by detailed balance. Adopting the collisional coefficients of Palay et al. (2012), and an H II region electron density of $1,000 \text{ cm}^{-3}$, as has been determined to be the case in 3C 368 (Lamarche et al., 2017), we calculate a value of $\epsilon_\lambda = 7.6 \times 10^{-22} \text{ erg s}^{-1} \text{ cm}^3$ for the [O III] 52 μm line. We additionally assume $n_e/n_p = 1.05$, which accounts for the electrons contributed from helium, and $T_4 = 1$, a typical value for H II regions.

Combining the total integrated [O III] 52 μm line flux ($1.34 \times 10^{-17} \text{ W m}^{-2}$; Lamarche et al., 2017) with the estimated free-free flux density at 230 GHz (rest-frame), and using Equation 4.2, we calculate $[\text{O}^{++}/\text{H}] = 1 \times 10^{-4}$. Then, to determine the $[\text{O}^{++}/\text{O}]$ ratio, and hence scale our ionic oxygen abundance to total oxygen abundance, an estimate for the hardness of the ambient radiation field within 3C 368 is required. Using the H II region models of Rubin (1985), we predicted that $\sim 84\%$ of the oxygen within the H II regions of 3C 368 is in the O⁺⁺ state (Lamarche et al., 2017). Using that ionization fraction here, we obtain an estimated [O/H] ratio of 1.2×10^{-4} , or $\sim 0.3 Z_{\odot}$ (Asplund et al., 2009), within about a factor of two uncertainty, where this uncertainty is dominated by both the uncertainty in determining the free-free contribution to the radio SED and the uncertainty in the measured [O III] 52 μm line flux.

This low-metallicity value is consistent with the results of Croxall et al. (2017), who found empirically that the [C II] 158 μm / [N II] 205 μm line ratio is highly elevated in low-metallicity sources. In Lamarche et al. (2017) we found a lower-bound of $[\text{C II}] 158 \mu\text{m} / [\text{N II}] 205 \mu\text{m} > 60$, which would indicate $12 + \log(\text{O/H}) \sim 8.1$, or equivalently $Z \sim 0.25 Z_{\odot}$, in the sample from Croxall et al. (2017).

An alternative explanation for the radio emission emanating from the core component of 3C 368 is that it originates from the AGN itself. Strong synchrotron self-absorption can lead to AGN with flat radio spectra, such that the radio emission which we attribute to thermal free-free emission from extended star-forming H II regions may instead come from a compact AGN (e.g., Roellig et al., 1986). As a check on this possibility, we examine the radio/IR correlation,

q_{IR} (e.g., [Ivison et al., 2010](#)), where

$$q_{IR} \equiv \log_{10} \left(\frac{S_{IR}/(3.75 \times 10^{12} W m^{-2})}{S_{1.4 GHz}/(W m^{-2} Hz^{-1})} \right), \quad (4.4)$$

S_{IR} is the total integrated IR flux (rest-frame 8 – 1000 μ m) in units of $W m^{-2}$, and $S_{1.4 GHz}$ is the flux density at 1.4 GHz in units of $W m^{-2} Hz^{-1}$. Extrapolating the SED-decomposed thermal contribution to the radio emission at rest-frame 230 GHz (45 μ Jy) to the expected value at 1.4 GHz using a free-free power-law index of -0.1, and using the total FIR luminosity attributed to star formation in 3C 368 ($2.0 \times 10^{12} L_\odot$, [Podigachoski et al., 2015](#)) to calculate S_{IR} , we obtain a value of $q_{IR} = 2.6$. This value is within the range seen in star-forming galaxies (e.g., [Ivison et al., 2010](#)), suggesting that the attribution of the radio continuum to free-free emission in 3C 368 is appropriate.

Unfortunately, our 230 GHz rest-frame ALMA observations ([Lamarche et al., 2017](#)), with a synthesized beam of size $3''.12 \times 1''.81$, do not resolve the core of 3C 368. We will propose for higher resolution continuum imaging with ALMA to test the theory of extended H II regions vs. compact AGN as the source for the high-frequency radio continuum in 3C 368, thereby confirming or rejecting the low-metallicity hypothesis for the ISM within 3C 368.

Comparison With Optically-Derived Metallicity

The sub-solar oxygen abundance that we derive for 3C 368 using the [O III] 52 μ m line and radio free-free continuum can be compared to the same value derived using optical lines. Observations exist for 3C 368 in the [O III] 5007 Å, [O II] 3727 Å, and H δ lines, such that R_{23} (e.g., [Pagel et al., 1979](#)) can be calculated

by assuming a scaling from H δ to H β , where

$$R_{23} \equiv \frac{[OII]\lambda3727 + [OIII]\lambda\lambda4959, 5007}{H\beta}. \quad (4.5)$$

Adopting an [O III] 5007 Å line flux of 6.8×10^{-18} W m $^{-2}$ (Jackson & Rawlings, 1997), an [O II] 3727 Å line flux of 5.9×10^{-18} W m $^{-2}$ (Best et al., 2000), an H δ line flux of 2.8×10^{-19} W m $^{-2}$ (Best et al., 2000), and assuming the theoretical scaling of H δ /H β = 0.26 (Case-B recombination, e.g., Osterbrock & Ferland, 2006), we obtain an R₂₃ value of ~ 12 . This R₂₃ value indicates 12 + log(O/H) ~ 8.3 (Kewley & Dopita, 2002), or ~ 0.4 Z $_{\odot}$ (Asplund et al., 2009), making it consistent with the FIR/radio-derived estimate.

4.3.3 PDRs

PDR Parameters

In Lamarche et al. (2017), we modeled the photo-dissociation regions (PDRs) within 3C 368 utilizing the PDR Toolbox (Kaufman et al., 2006, Pound & Wolfire, 2008), together with detections of the [C II] 158 μ m (Stacey et al., 2010b) and [O I] 63 μ m lines, as well as the modeled far-IR continuum luminosity (Podigachoski et al., 2015), obtaining best-fit parameters of G₀ ~ 280 Habing units and n $\sim 7,500$ cm $^{-3}$. Here we update the model to include the two newly-detected lines.

Including the CO(4-3) and [C I] 609 μ m lines, we obtain new best-fit values of G₀ ~ 320 Habing units and n $\sim 3,200$ cm $^{-3}$, with a PDR surface temperature of ~ 200 K (see Figure 4.5). These PDR parameters are similar to those which

we obtained previously, up to a decrease in the density, due to the detection significance of the CO(4-3) and [C I] 609 μm lines, which tightly constrain that parameter. We again see that the [C II] emission is elevated relative to the CO emission, and now also relative to the [C I] emission.

The penetration of far-UV photons capable of photodissociating CO and ionizing carbon is limited by dust extinction. Therefore, assuming dust content scales with metallicity, the CO-photodissociated surface of a molecular cloud becomes much larger relative to the shielded CO-emitting core in low-metallicity environments. In PDR models (e.g., [Kaufman et al., 2006](#)), [C I] line emission arises from a thin transition region of neutral carbon that lies between the C⁺ and CO regions. The [C II] line flux is therefore enhanced relative to both CO and [C I] in these environments (e.g., [Maloney & Black, 1988](#), [Stacey et al., 1991](#)).

PDR Mass

Using the calculated n, G₀, and PDR surface temperature values in 3C 368, we can estimate the PDR mass following [Hailey-Dunsheath et al. \(2010\)](#):

$$\frac{M_{PDR}}{M_{\odot}} = 0.77 \left(\frac{0.93 L_{[C\,II]}}{L_{\odot}} \right) \left(\frac{1.4 \times 10^{-4}}{X_{C^+}} \right) \times \frac{1 + 2 \exp(-\frac{-91K}{T}) + \frac{n_{crit}}{n}}{2 \exp(-\frac{-91K}{T})}, \quad (4.6)$$

where X_{C⁺} is the abundance of C⁺ per hydrogen atom, taken here to be 1.4 × 10⁻⁴ ([Savage & Sembach, 1996](#)), n_{crit} is the critical density of the [C II] 158 μm transition (2,800 cm⁻³, [Stacey, 2011](#)), and assuming that ∼93% of the [C II]

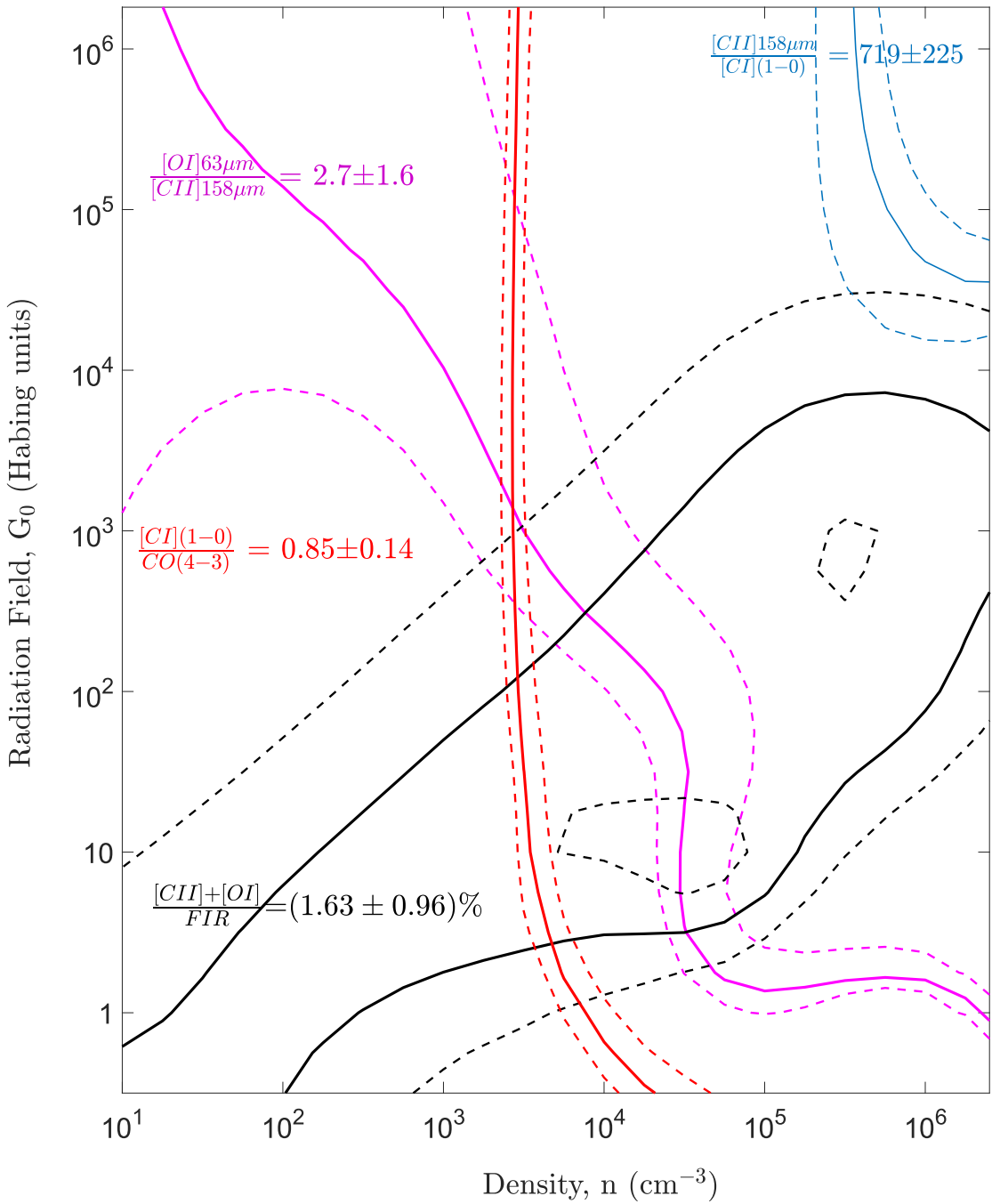


Figure 4.5 A plot of the best-fit PDR parameters in 3C 368, generated using the models of Pound & Wolfire (2008) and Kaufman et al. (2006). The fit favors PDRs with $G_0 \sim 320$ Habing units and $n \sim 3,200 \text{ cm}^{-3}$.

emission originates within the PDRs of 3C 368 as we estimated in Lamarche et al. (2017). We calculate a PDR gas mass of $\sim 1.7 \times 10^{10} M_{\odot}$ in this source.

Molecular-Gas Mass

With detections of both the CO(4-3) and [C I] 609 μm lines, the molecular-gas mass within 3C 368 can be estimated in three ways:

First, using the detection of the CO(4-3) line, we can estimate the molecular-gas mass by assuming a conversion factor back to CO(1-0) and then adopting an α_{CO} value. The measured CO(4-3) line flux of $1.08 \pm 0.14 \text{ Jy km s}^{-1}$ equates to a value of $L'_{CO(4-3)} = 4.6 \pm 0.6 \times 10^9 \text{ K km s}^{-1} \text{ pc}^2$. Our previous non-detection of the CO(2-1) line with ALMA yields a 3σ upper limit of $L'_{CO(2-1)} < 3.45 \times 10^9 \text{ K km s}^{-1} \text{ pc}^2$ (Lamarche et al., 2017). This implies that $r_{43/21} > 1.3$, so we use this excitation ratio to scale $L'_{CO(4-3)}$ back to $L'_{CO(1-0)}$. Taking a ULIRG value of $\alpha_{CO} = 0.8 M_{\odot}(\text{K km s}^{-1} \text{ pc}^2)^{-1}$ (e.g., Bolatto et al., 2013), we obtain a molecular-gas mass of $2.9 \times 10^9 M_{\odot}$.

If, instead, we calculate a value of α_{CO} based on the metallicity estimates from section 3.2, adopting the scaling of Glover & Mac Low (2011) (and see also Bolatto et al., 2013), we obtain $\alpha_{CO} \sim 18 M_{\odot}(\text{K km s}^{-1} \text{ pc}^2)^{-1}$. Adopting this larger value of α_{CO} , and assuming the same super-thermal CO-excitation as above, we obtain a molecular mass of $6.4 \times 10^{10} M_{\odot}$. This metallicity-adjusted α_{CO} -based molecular gas mass is $\sim 4x$ larger than the PDR gas mass estimated above, making the mass ratio consistent with that observed in other starburst galaxies (e.g., Stacey et al., 1991), lending further credibility to the low-metallicity explanation for the small CO luminosity in 3C 368.

Second, we can calculate the molecular-gas mass by scaling from the observed [C I] 609 μm line flux. Following Bothwell et al. (2017):

$$M(H_2)^{[CI]} = 1375.8 D_L^2 (1+z)^{-1} \left(\frac{X_{[CI]}}{10^{-5}} \right)^{-1} \times \left(\frac{A_{10}}{10^{-7} \text{s}^{-1}} \right)^{-1} Q_{10}^{-1} S_{[CI]} \Delta v, \quad (4.7)$$

where D_L is the luminosity distance in Mpc (7,735 in the case of 3C 368), $X_{[CI]}$ is the [C I]/H₂ abundance ratio, taken here to be 3×10^{-5} (e.g., Papadopoulos & Greve, 2004, Weiß et al., 2003), A_{10} is the Einstein A coefficient, $7.93 \times 10^{-8} \text{s}^{-1}$ (Wiese et al., 1966), Q_{10} is the excitation parameter which depends on gas density, kinetic temperature and radiation field (e.g., Papadopoulos et al., 2004), which we take to be 0.6 (Bothwell et al., 2017), and $S_{[CI]} \Delta v$ is the flux of the [C I] 609 μm line in units of Jy km s⁻¹. We obtain a molecular-gas mass of $2.3 \times 10^{10} M_\odot$. We note that this molecular-gas mass is ~ 3 x smaller than that derived using the metallicity-corrected α_{CO} method above. If we scale the [C I]/H₂ abundance ratio, $X_{[CI]}$, by the sub-solar gas-phase metallicity estimated in section 3.2, $Z \sim 0.3 Z_\odot$, we calculate an H₂ mass of $7.7 \times 10^{10} M_\odot$. Boosting this mass by $\sim 20\%$ to account for the contribution from helium, which is already accounted for in the α_{CO} -based method above, increases the mass estimate to $9.2 \times 10^{10} M_\odot$, such that the two methods produce masses which differ by $\sim 30\%$.

Finally, we can use the dust mass calculated by multi-component SED modeling, along with a gas-to-dust ratio, δ_{GDR} , to estimate the molecular-gas mass within 3C 368. Adopting an SED-modeled dust-mass of $1.4 \times 10^8 M_\odot$ (Podigachoski et al., 2015) and a gas-to-dust ratio of 540, appropriate for $Z \sim 0.3 Z_\odot$

(Rémy-Ruyer et al., 2014), we obtain a molecular-gas mass of $7.6 \times 10^{10} M_{\odot}$. Or, equivalently, if we use the CO-derived gas-mass together with the SED-modeled dust-mass, we obtain a value of $\delta_{GDR} = 464$. Since α_{CO} and δ_{GDR} scale differently with metallicity, the CO- and dust-derived gas masses are incompatible at solar metallicity, giving us more confidence that 3C 368 does indeed have sub-solar metallicity, and that our derived gas masses are robust.

The calculated molecular-gas mass implies that, at its current star-formation rate, $\sim 350 M_{\odot} \text{ yr}^{-1}$ (Podigachoski et al., 2015), 3C 368 will deplete its supply of molecular gas in ~ 170 Myrs. We can additionally calculate the gas fraction, $f_{gas} \equiv \frac{M_{gas}}{M_{gas} + M_{stars}}$, and the specific star-formation rate, $sSFR \equiv \frac{SFR}{M_{stars}}$, in 3C 368, finding values of ~ 0.15 and $\sim 1 \text{ Gyr}^{-1}$, respectively. The calculated sSFR puts 3C 368 on the upper end of the galaxy main-sequence as defined by Genzel et al. (2015), with $SFR/SFR_{MS} = 2.8$, and the gas fraction lies exactly on the scaling with $sSFR/sSFR_{MS}$, stellar mass, and redshift found in Scoville et al. (2017). Moreover, 3C 368 lies along the $L'_{[CI]}$ to L_{IR} correlation found in other high-redshift main-sequence galaxies, however it is elevated in its $L'_{[CI]}/L'_{CO(2-1)}$ ratio, with a lower limit of 0.9, by a factor of ~ 4.4 (Valentino et al., 2018). The models of Papadopoulos et al. (2018) find the [C I](1-0)/CO(1-0) brightness ratio to be much larger than unity in low-metallicity or cosmic-ray-dominated regions, however, since we have only a modest lower limit on this ratio, we cannot draw any strong conclusions from it. When compared to a sample of low-metallicity high-redshift sources (Coogan et al., 2019), 3C 368 is observed to be similarly deficient in CO emission, and when compared to a sample of local luminous infrared galaxies (LIRGs) and spirals (Liu et al., 2015), it has a CO(4-3) flux which falls below that expected from the scaling with FIR luminosity, by a factor of ~ 3.7 .

4.3.4 Dynamical Mass

Since our ALMA observations of 3C 368 spatially resolve the source, we can additionally estimate the dynamical mass of the galaxy. Assuming a disk geometry and circular orbits:

$$M_{dyn} = \frac{v_{rot}^2 r}{G}, \quad (4.8)$$

where v_{rot} is the true rotational velocity of the disk, estimated from the observed velocity by correcting for the average inclination angle, $\langle v_{rot} \rangle \sim \frac{\pi}{2} v_{obs}$ (e.g., [Erb et al., 2006](#)), r is the radius of the line-emitting region of the galaxy, and G is the universal gravitational constant.

We estimate the radius from two-dimensional Gaussian fits to the CO(4-3) moment-zero map ($r = 0.5 \text{ FWHM} = 3.14 \text{ kpc}$). Similarly, we take the observed velocity to be half the full-width-half-maximum (FWHM) of the CO(4-3) line ($v_{obs} = 284 \text{ km s}^{-1}$). We obtain a dynamical mass of $\sim 1.5 \times 10^{11} M_{\odot}$. This dynamical mass estimate is $\sim 2x$ smaller than the estimated stellar mass within 3C 368 ($\sim 3.6 \times 10^{11} M_{\odot}$, [Best et al., 1998b](#)), a discrepancy that can be due to the effects of inclination angle and mass profile on the calculated dynamical mass.

4.4 Conclusions

We have presented detections of the CO(4-3) and [C I] 609 μm spectral lines, as well as the rest-frame 480.5 GHz dust continuum, in 3C 368, an FR-II type galaxy at redshift 1.131.

Table 4.2. Physical properties of 3C 368

Property	Value	Reference
R.A. (J2000)	$18^h 05^m 06^s.40$	Best et al. (1998a)
Dec. (J2000)	$+11^\circ 01' 33''.09$	Best et al. (1998a)
z	1.131	Meisenheimer & Hippelein (1992)
SFR	$350 M_\odot \text{ yr}^{-1}$	Podigachoski et al. (2015)
M_*	$3.6 \times 10^{11} M_\odot$	Best et al. (1998b)
M_{gas}	$6.5 \times 10^{10} M_\odot$	This Work
M_{PDR}	$1.7 \times 10^{10} M_\odot$	This Work
M_{dust}	$1.4 \times 10^8 M_\odot$	Podigachoski et al. (2015)
M_{dyn}	$>1.5 \times 10^{11} M_\odot$	This Work
δ_{GDR}	464	This Work
f_{gas}	0.15	This Work
sSFR	1 Gyr^{-1}	This Work
SFR/SFR _{MS}	2.8	This Work, Genzel et al. (2015)
$\tau_{Depletion}$	170 Myr	This Work

Note. — See the text for explanations of the physical properties presented in this work.

We have estimated the gas-phase metallicity in 3C 368 using two independent methods: (1) combining the observed [O III] 52 μm fine-structure line flux with radio free-free continuum emission and (2) employing the optical [O III] 5007 Å and [O II] 3727 Å lines (R_{23} technique). Both methods arrive at a consistent gas-phase metallicity of $\sim 0.3 Z_\odot$.

We have calculated the molecular-gas mass within 3C 368 in three independent ways: (1) using the CO(4-3) line luminosity, gas excitation, and a metallicity-adjusted α_{CO} conversion factor, (2) scaling from the luminosity of the atomic carbon line, and (3) adopting a conversion factor from dust mass to molecular-gas mass. We find a consistent gas mass estimate of $\sim 6.5 \times 10^{10} M_\odot$

across these three methods only when adopting a gas-phase metallicity of ~ 0.3 Z_{\odot} .

Considering this molecular-gas mass, and a star-formation rate of $\sim 350 M_{\odot}$ yr^{-1} (Podigachoski et al., 2015), we deduce that 3C 368 has a molecular-gas depletion-time, $\tau_{\text{Depletion}}$, of ~ 170 Myrs. We also calculate a gas fraction, f_{gas} , and specific star-formation rate, sSFR, adopting a stellar mass of $\sim 3.6 \times 10^{11} M_{\odot}$ (Best et al., 1998b), of ~ 0.15 and $\sim 1 \text{ Gyr}^{-1}$, respectively. The calculated sSFR puts 3C 368 on the upper end of the galaxy main-sequence, as defined by Genzel et al. (2015), and the gas fraction lies exactly on the scaling with sSFR/sSFR_{MS}, stellar mass, and redshift found in Scoville et al. (2017).

Further observations will allow us to determine whether 3C 368 does indeed have low gas-phase metallicity, if indeed free-free continuum emission dominates the radio spectrum at high frequencies, or whether the AGN is strongly contaminating the emission in those bands. In particular, we will propose for higher angular-resolution observations at rest-frame 230 GHz to determine whether the radio continuum is extended, as should be the case if it originates from star-forming H II regions, or compact, as would be the case if it is of AGN origin.

CHAPTER 5

SUMMARY AND FUTURE WORK

In this thesis, we have presented observations of the ionized, neutral, and molecular, phases of the ISM within galaxies during the peak epoch of cosmic star formation, in an effort to better understand the modes of star formation in the early universe. In the following sections, we briefly summarize our findings and discuss the next steps in this line of research.

5.1 Star formation during the peak epoch

In chapter 2, we presented the detection of four far-infrared fine-structure oxygen lines, as well as strong upper limits for the CO(2–1) and [N II] 205 μm lines, in 3C 368, a well-studied radio-loud galaxy at $z = 1.131$. These oxygen lines, taken in conjunction with previously observed neon and carbon fine-structure lines, suggest a powerful active galactic nucleus (AGN), accompanied by vigorous and extended star formation. A starburst dominated by O8 stars, with an age of ~ 6.5 Myr, provides a good fit to the fine-structure line data. This estimated age of the starburst makes it nearly concurrent with the latest episode of AGN activity, suggesting a link between the growth of the supermassive black hole and stellar population in this source. We did not detect the CO(2–1) line, down to a level twelve times lower than the expected value for star-forming galaxies. This lack of CO line emission is consistent with recent star-formation activity if the star-forming molecular gas has low metallicity, is highly fractionated (such that CO is photodissociated through much of the clouds), or is chemically very young (such that CO has not yet had time to form).

In chapter 3, we investigated the properties of the interstellar medium, star formation, and the current-day stellar population in the strongly-lensed star-forming galaxy H-ATLAS J091043.1-000321 (SDP.11), at $z = 1.7830$. We reported detections of the [O III] $52 \mu\text{m}$, [N III] $57 \mu\text{m}$, and [O I] $63 \mu\text{m}$ lines from *Herschel/PACS*, and presented high-resolution imaging of the [C II] $158 \mu\text{m}$ line, and underlying continuum, using ALMA. We resolved the [C II] line emission into two spatially-offset Einstein rings, tracing the red- and blue-velocity components of the line, in the ALMA/Band-9 observations at $0''.2$ resolution. The values seen in the [C II]/FIR ratio map, as low as $\sim 0.02\%$ at the peak of the dust continuum, are similar to those of local ULIRGs, suggesting an intense starburst in this source. This is consistent with the high intrinsic FIR luminosity ($\sim 3 \times 10^{12} L_\odot$), ~ 16 Myr gas depletion timescale, and $\lesssim 8$ Myr timescale since the last starburst episode, estimated from the hardness of the UV radiation field. By applying gravitational-lens models to the visibilities in the uv-plane, we found that the lensing magnification factor varies by a factor of two across SDP.11, affecting the observed line profiles. After correcting for the effects of differential lensing, a symmetric line profile was recovered, suggesting that the starburst present here may not be the result of a major merger, as is the case for local ULIRGs, but instead could be powered by star-formation activity spread across a 3-5 kpc rotating disk.

In chapter 4, we returned to 3C 368, presenting detections of the CO(4-3) and [C I] $609 \mu\text{m}$ spectral lines, as well as the dust continuum at 480.5 GHz (rest-frame). Our observations allowed us to inventory the molecular-gas reservoirs in 3C 368 by applying three independent methods: (1) using the CO(4-3)-line luminosity, excitation state of the gas, and an α_{CO} conversion factor, (2) scaling from the [C I]-line luminosity, and (3) adopting a gas-to-dust conversion

factor. We also presented gas-phase metallicity estimates in this source, both using far-infrared (FIR) fine-structure lines together with radio free-free continuum emission and independently employing the optical [O III] 5007 Å and [O II] 3727 Å lines (R_{23} method). Both methods agree on a sub-solar gas-phase metallicity of $\sim 0.3 Z_\odot$. Intriguingly, comparing the molecular-gas mass estimated using this sub-solar metallicity, $M_{gas} \sim 6.5 \times 10^{10} M_\odot$, to dust-mass estimates from multi-component spectral energy distribution (SED) modeling, $M_{dust} \sim 1.4 \times 10^8 M_\odot$, yields a gas-to-dust ratio within $\sim 15\%$ of the accepted value for a metallicity of $0.3 Z_\odot$. The derived gas-mass puts 3C 368 on par with other galaxies at $z \sim 1$ in terms of specific star-formation rate and gas fraction. We suggest that perhaps 3C 368 is accreting pristine molecular gas from an external source, thereby diluting its gas-phase metallicity.

The findings presented in this thesis support the idea of a different mode of star formation being present in high-redshift galaxies. We observe star formation extended over kiloparsec-scale disks in galaxies at $z \sim 1 - 2$, in contrast to local ULIRGs, which generally have intense star formation confined to their centers after major-merger events. We also find evidence of AGN feedback at play in the galaxies which we studied, indicating that it does indeed play an important role in shaping the star-formation histories of galaxies.

5.2 Future work

More work is required to develop the full picture of star formation across cosmic time. One piece of the puzzle that I'm very excited about studying is the buildup of metals in galaxies. Gas-phase metallicity is accumulated through

generations of stars fusing metals in their interiors and expelling them back into the surrounding ISM, and hence is a great way of studying the star-formation histories of galaxies.

5.2.1 FIR abundance determinations in nearby galaxies

Absolute abundances of the most common metals (e.g., oxygen, nitrogen, carbon) remain poorly known in galaxies to this day, even in the local universe. This is because abundance determinations are generally made using observations of spectral lines in the optical bands, where emission from ionized-gas regions is very sensitive to both the temperature structure of the emitting plasma and dust extinction along the line-of-sight. Indeed, metallicities calculated in the same sample of galaxies can vary greatly, depending on the adopted calibration (e.g., [Kewley & Ellison, 2008](#), see Figure 5.1).

As part of my postdoctoral position at the University of Toledo, I will use FIR fine-structure line observations, together with radio free-free emission data, to calculate the absolute gas-phase abundance of oxygen in a sample of nearby galaxies. FIR abundance determinations are much less sensitive to both the temperature structure of the ionized gas and the line-of-sight dust extinction, making them excellent abundance tracers. These absolute oxygen abundances will be instrumental in determining the metal enrichment, and hence the star-formation histories, of the observed galaxies. We have successfully employed this technique to probe the metallicity in galaxies at $z \sim 1 - 2$, where *Herschel* observations of the [O III] 52 and 88 μm lines were available. This method may also be extended to very high-redshift galaxies, where the [O III] 52 and/or 88 μm

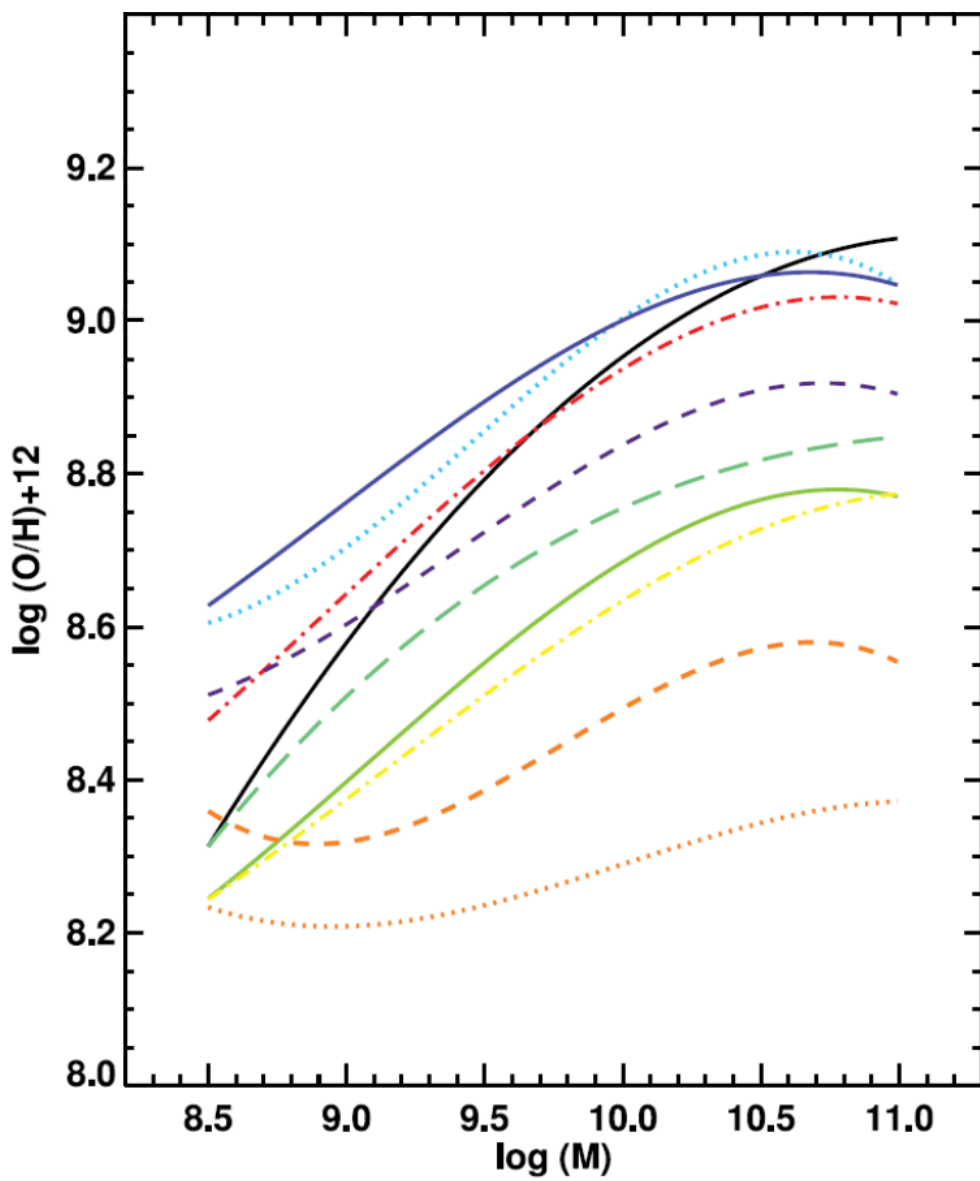


Figure 5.1 A plot showing the mass-metallicity relation in a sample of $>20,000$ galaxies from the Sloan Digital Sky Survey (SDSS) Data Release 4 (DR4). The different colors denote different calibrations used to determine the optically-derived metallicities in the same sample of galaxies. The different calibrations produce metallicities which vary by ~ 0.6 dex, a factor of ~ 4 , in the same sample of galaxies (adapted from [Kewley & Ellison, 2008](#)).

lines are red-shifted into the high-frequency bands accessible with ALMA.

5.2.2 The James Webb Space Telescope

In addition to determining metal abundances in nearby galaxies in the far-infrared bands, and continuing high-redshift studies with ALMA at sub-millimeter wavelengths, the new *James Webb Space Telescope (JWST)* will allow for high-redshift observations of rest-frame optical nebular lines. Scheduled to launch in 2021, *JWST*'s near- and mid-infrared integral-field spectrographs will enable the mapping of optical nebular lines in high-redshift galaxies, as well as mid-IR lines at more moderate redshifts. This capability will allow us to determine optical metal abundances in the era of peak cosmic star formation, keeping in mind the caveats mentioned above.

Additionally, *JWST*, with its 6.5 m primary mirror, and hence increased angular resolution, will allow us to build upon the discoveries made with the *Spitzer Space Telescope*. For example, a correlation between [Ne III] and [Ne V] line emission in galaxies with dominant AGN was discovered using *Spitzer* (e.g., Gorjian et al., 2007). In galaxies which lie above this correlation, e.g. have stronger [Ne III] emission than is expected from their [Ne V] line flux, the excess [Ne III] emission is generally attributed to star formation. The mid-IR integral-field spectrograph onboard *JWST* will allow us to test this assumption directly, out to modest redshift, both confirming the AGN relation and allowing for spatially-resolved modeling of the stellar populations within the targeted galaxies.

BIBLIOGRAPHY

- Archibald, E. N., Dunlop, J. S., Hughes, D. H., et al. 2001, MNRAS, 323, 417
- Armus, L., Heckman, T., & Miley, G. 1987, AJ, 94, 831
- Asplund, M., Grevesse, N., Sauval, A. J., & Scott, P. 2009, ARA&A, 47, 481
- Becker, R. H., White, R. L., & Helfand, D. J. 1995, ApJ, 450, 559
- Bernard Salas, J., Pottasch, S. R., Beintema, D. A., & Wesselius, P. R. 2001, A&A, 367, 949
- Best, P. N., Carilli, C. L., Garrington, S. T., Longair, M. S., & Röttgering, H. J. A. 1998a, MNRAS, 299, 357
- Best, P. N., Longair, M. S., & Roettgering, H. J. A. 1998b, MNRAS, 295, 549
- Best, P. N., Röttgering, H. J. A., & Longair, M. S. 2000, MNRAS, 311, 1
- Blain, A. W., Barnard, V. E., & Chapman, S. C. 2003, MNRAS, 338, 733
- Bolatto, A. D., Wolfire, M., & Leroy, A. K. 2013, ARA&A, 51, 207
- Boreiko, R. T., Betz, A. L., & Zmuidzinas, J. 1988, ApJ, 325, L47
- Bothwell, M. S., Smail, I., Chapman, S. C., et al. 2013, MNRAS, 429, 3047
- Bothwell, M. S., Aguirre, J. E., Aravena, M., et al. 2017, MNRAS, 466, 2825
- Brisbin, D., Ferkinhoff, C., Nikola, T., et al. 2015, ApJ, 799, 13
- Bussmann, R. S., Pérez-Fournon, I., Amber, S., et al. 2013, ApJ, 779, 25
- Bussmann, R. S., Riechers, D., Fialkov, A., et al. 2015, ApJ, 812, 43
- Carilli, C. L., & Walter, F. 2013, ARA&A, 51, 105

- Casey, C. M., Narayanan, D., & Cooray, A. 2014, *Phys. Rep.*, 541, 45
- Chambers, K. C., Miley, G. K., & Joyce, R. R. 1988, *ApJ*, 329, L75
- Condon, J. J. 1992, *ARA&A*, 30, 575
- Coogan, R. T., Sargent, M. T., Daddi, E., et al. 2019, *MNRAS*, 485, 2092
- Coppin, K. E. K., Danielson, A. L. R., Geach, J. E., et al. 2012, *MNRAS*, 427, 520
- Cormier, D., Lebouteiller, V., Madden, S. C., et al. 2012, *A&A*, 548, A20
- Cormier, D., Madden, S. C., Lebouteiller, V., et al. 2015, *A&A*, 578, A53
- Crawford, C. S., & Fabian, A. C. 1995, *MNRAS*, 273, 827
- Crawford, M. K., Lugten, J. B., Fitelson, W., Genzel, R., & Melnick, G. 1986, *ApJ*, 303, L57
- Croft, S., van Breugel, W., de Vries, W., et al. 2006, *ApJ*, 647, 1040
- Croxall, K. V., Smith, J. D., Pellegrini, E., et al. 2017, *ApJ*, 845, 96
- Daddi, E., Dickinson, M., Morrison, G., et al. 2007, *ApJ*, 670, 156
- Dale, D. A., Helou, G., Contursi, A., Silbermann, N. A., & Kolhatkar, S. 2001, *ApJ*, 549, 215
- Dekel, A., Birnboim, Y., Engel, G., et al. 2009, *Nature*, 457, 451
- Dey, A., van Breugel, W., Vacca, W. D., & Antonucci, R. 1997, *ApJ*, 490, 698
- Díaz-Santos, T., Armus, L., Charmandaris, V., et al. 2017, *ApJ*, 846, 32
- Djorgovski, S., Spinrad, H., Pedelty, J., Rudnick, L., & Stockton, A. 1987, *AJ*, 93, 1307

Draine, B. T. 2011, Physics of the Interstellar and Intergalactic Medium (Princeton University Press)

Draine, B. T., & Lee, H. M. 1984, ApJ, 285, 89

Drouart, G., Rocca-Volmerange, B., De Breuck, C., et al. 2016, A&A, 593, A109

Dye, S., Negrello, M., Hopwood, R., et al. 2014, MNRAS, 440, 2013

Eales, S., Dunne, L., Clements, D., et al. 2010, PASP, 122, 499

Edge, D. O., Shakeshaft, J. R., McAdam, W. B., Baldwin, J. E., & Archer, S. 1959, MmRAS, 68, 37

Emonts, B. H. C., Norris, R. P., Feain, I., et al. 2014, MNRAS, 438, 2898

Erb, D. K., Steidel, C. C., Shapley, A. E., et al. 2006, ApJ, 646, 107

Evans, A. S., Sanders, D. B., Mazzarella, J. M., et al. 1996, ApJ, 457, 658

Ferkinhoff, C., Hailey-Dunsheath, S., Nikola, T., et al. 2010, ApJ, 714, L147

Ferkinhoff, C., Brisbin, D., Nikola, T., et al. 2011, ApJ, 740, L29

Ferkinhoff, C., Brisbin, D., Parshley, S., et al. 2014, ApJ, 780, 142

Ferkinhoff, C., Higdon, S., Higdon, J. L., et al. 2017, in American Astronomical Society Meeting Abstracts, Vol. 229, American Astronomical Society Meeting Abstracts #229, 214.06

Ferrarese, L., & Merritt, D. 2000, ApJ, 539, L9

Gaibler, V., Khochfar, S., Krause, M., & Silk, J. 2012, MNRAS, 425, 438

Genzel, R., Tacconi, L. J., Gracia-Carpio, J., et al. 2010, MNRAS, 407, 2091

- Genzel, R., Tacconi, L. J., Lutz, D., et al. 2015, *ApJ*, 800, 20
- Glover, S. C. O., & Clark, P. C. 2012, *MNRAS*, 421, 116
- Glover, S. C. O., & Mac Low, M. M. 2011, *MNRAS*, 412, 337
- Gorjian, V., Cleary, K., Werner, M. W., & Lawrence, C. R. 2007, *ApJ*, 655, L73
- Graciá-Carpio, J., Sturm, E., Hailey-Dunsheath, S., et al. 2011, *ApJ*, 728, L7
- Griffin, M. J., Abergel, A., Abreu, A., et al. 2010, *A&A*, 518, L3
- Gullberg, B., De Breuck, C., Vieira, J. D., et al. 2015, *MNRAS*, 449, 2883
- Hailey-Dunsheath, S., Nikola, T., Stacey, G. J., et al. 2010, *ApJ*, 714, L162
- Hammer, F., Proust, D., & Le Fevre, O. 1991, *ApJ*, 374, 91
- Harrington, K. C., Yun, M. S., Magnelli, B., et al. 2018, *MNRAS*, 474, 3866
- Harris, A. I., Baker, A. J., Frayer, D. T., et al. 2012, *ApJ*, 752, 152
- Hayes, M. A., & Nussbaumer, H. 1984, *A&A*, 134, 193
- Hernán-Caballero, A., Spoon, H. W. W., Lebouteiller, V., Rupke, D. S. N., & Barry, D. P. 2016, *Monthly Notices of the Royal Astronomical Society*, 455, 1796
- Herrera-Camus, R., Bolatto, A., Smith, J. D., et al. 2016, *ApJ*, 826, 175
- Herter, T., Helfer, H. L., Pipher, H. L., et al. 1981, *ApJ*, 250, 186
- Hollenbach, D. J., & Tielens, A. G. G. M. 1999, *Reviews of Modern Physics*, 71, 173
- Hönig, S. F., & Kishimoto, M. 2010, *A&A*, 523, A27

- Houck, J. R., Roellig, T. L., van Cleve, J., et al. 2004, ApJS, 154, 18
- Hughes, T. M., Foyle, K., Schirm, M. R. P., et al. 2015, A&A, 575, A17
- Ivison, R. J., Magnelli, B., Ibar, E., et al. 2010, A&A, 518, L31
- Jackson, N., & Rawlings, S. 1997, MNRAS, 286, 241
- Kaufman, M. J., Wolfire, M. G., & Hollenbach, D. J. 2006, ApJ, 644, 283
- Kaufman, M. J., Wolfire, M. G., Hollenbach, D. J., & Luhman, M. L. 1999, ApJ, 527, 795
- Kennicutt, Robert C., J. 1998, Annual Review of Astronomy and Astrophysics, 36, 189
- Kereš, D., Katz, N., Weinberg, D. H., & Davé, R. 2005, MNRAS, 363, 2
- Kewley, L. J., & Dopita, M. A. 2002, The Astrophysical Journal Supplement Series, 142, 35
- Kewley, L. J., & Ellison, S. L. 2008, ApJ, 681, 1183
- King, A., & Pounds, K. 2015, ARA&A, 53, 115
- Klein, U., Lisenfeld, U., & Verley, S. 2018, A&A, 611, A55
- Kormendy, J., & Ho, L. C. 2013, ARA&A, 51, 511
- Lamarche, C., Stacey, G., Brisbin, D., et al. 2017, ApJ, 836, 123
- Lamarche, C., Verma, A., Vishwas, A., et al. 2018, ApJ, 867, 140
- Larson, R. B. 1981, MNRAS, 194, 809
- Lebouteiller, V., Barry, D. J., Goes, C., et al. 2015, ApJS, 218, 21

- Lebouteiller, V., Barry, D. J., Spoon, H. W. W., et al. 2011, ApJS, 196, 8
- Lester, D. F., Dinerstein, H. L., Werner, M. W., et al. 1987, ApJ, 320, 573
- Liu, D., Gao, Y., Isaak, K., et al. 2015, ApJ, 810, L14
- Lord, S. D., Hollenbach, D. J., Haas, M. R., et al. 1996, ApJ, 465, 703
- Luhman, M. L., Satyapal, S., Fischer, J., et al. 1998, ApJ, 504, L11
- Lupu, R. E., Scott, K. S., Aguirre, J. E., et al. 2012, ApJ, 757, 135
- Madau, P., & Dickinson, M. 2014, ARA&A, 52, 415
- Madden, S. C., Poglitsch, A., Geis, N., Stacey, G. J., & Townes, C. H. 1997, ApJ, 483, 200
- Maiolino, R., Cox, P., Caselli, P., et al. 2005, A&A, 440, L51
- Maiolino, R., Gallerani, S., Neri, R., et al. 2012, MNRAS, 425, L66
- Malhotra, S., Helou, G., Stacey, G., et al. 1997, ApJ, 491, L27
- Malhotra, S., Kaufman, M. J., Hollenbach, D., et al. 2001, ApJ, 561, 766
- Maloney, P., & Black, J. H. 1988, ApJ, 325, 389
- Massardi, M., Enia, A. F. M., Negrello, M., et al. 2018, A&A, 610, A53
- McCarthy, P. J., van Breugel, W., Spinrad, H., & Djorgovski, S. 1987, ApJ, 321, L29
- Meijerink, R., Spaans, M., & Israel, F. P. 2007, A&A, 461, 793
- Meisenheimer, K., & Hippelein, H. 1992, A&A, 264, 455
- Meynet, G., & Maeder, A. 2003, A&A, 404, 975

- Murgia, M., Fanti, C., Fanti, R., et al. 1999, *A&A*, 345, 769
- Murphy, E. J., Condon, J. J., Schinnerer, E., et al. 2011, *ApJ*, 737, 67
- Nagao, T., Maiolino, R., Marconi, A., & Matsuhara, H. 2011, *A&A*, 526, A149
- Negrello, M., Hopwood, R., De Zotti, G., et al. 2010, *Science*, 330, 800
- Negrello, M., Hopwood, R., Dye, S., et al. 2014, *MNRAS*, 440, 1999
- Oberst, T. E., Parshley, S. C., Stacey, G. J., et al. 2006, *ApJ*, 652, L125
- Ossenkopf, V., Röllig, M., Neufeld, D. A., et al. 2013, *A&A*, 550, A57
- Osterbrock, D. E., & Ferland, G. J. 2006, *Astrophysics of gaseous nebulae and active galactic nuclei* (University Science Books)
- Oteo, I., Zhang, Z. Y., Yang, C., et al. 2017, *ApJ*, 850, 170
- Ott, S. 2010, in *Astronomical Society of the Pacific Conference Series*, Vol. 434, *Astronomical Data Analysis Software and Systems XIX*, ed. Y. Mizumoto, K.-I. Morita, & M. Ohishi, 139
- Pagel, B. E. J., Edmunds, M. G., Blackwell, D. E., Chun, M. S., & Smith, G. 1979, *MNRAS*, 189, 95
- Palay, E., Nahar, S. N., Pradhan, A. K., & Eissner, W. 2012, *MNRAS*, 423, L35
- Papadopoulos, P. P., Bisbas, T. G., & Zhang, Z.-Y. 2018, *MNRAS*, 478, 1716
- Papadopoulos, P. P., & Greve, T. R. 2004, *ApJ*, 615, L29
- Papadopoulos, P. P., Thi, W. F., & Viti, S. 2004, *MNRAS*, 351, 147
- Parkin, T. J., Wilson, C. D., Schirm, M. R. P., et al. 2013, *ApJ*, 776, 65

- Pavesi, R., Sharon, C. E., Riechers, D. A., et al. 2018, *ApJ*, 864, 49
- Pilbratt, G. L., Riedinger, J. R., Passvogel, T., et al. 2010, *A&A*, 518, L1
- Podigachoski, P., Barthel, P. D., Haas, M., et al. 2015, *A&A*, 575, A80
- Poglitsch, A., Krabbe, A., Madden, S. C., et al. 1995, *ApJ*, 454, 293
- Poglitsch, A., Waelkens, C., Geis, N., et al. 2010, *A&A*, 518, L2
- Pound, M. W., & Wolfire, M. G. 2008, in Astronomical Society of the Pacific Conference Series, Vol. 394, Astronomical Data Analysis Software and Systems XVII, ed. R. W. Argyle, P. S. Bunclark, & J. R. Lewis, 654
- Read, J. I., & Trentham, N. 2005, Philosophical Transactions of the Royal Society of London Series A, 363, 2693
- Rémy-Ruyer, A., Madden, S. C., Galliano, F., et al. 2014, *A&A*, 563, A31
- Rodighiero, G., Daddi, E., Baronchelli, I., et al. 2011, *ApJ*, 739, L40
- Roellig, T. L., Becklin, E. E., Impey, C. D., & Werner, M. W. 1986, *ApJ*, 304, 646
- Rubin, R. H. 1985, *ApJS*, 57, 349
- Rubin, R. H., Simpson, J. P., Colgan, S. W. J., et al. 2016, *MNRAS*, 459, 1875
- Rudolph, A. L., Simpson, J. P., Haas, M. R., Erickson, E. F., & Fich, M. 1997, *ApJ*, 489, 94
- Sanders, D. B., Soifer, B. T., Elias, J. H., et al. 1988, *ApJ*, 325, 74
- Savage, B. D., & Sembach, K. R. 1996, Annual Review of Astronomy and Astrophysics, 34, 279
- Scoville, N., Sheth, K., Aussel, H., et al. 2016, *ApJ*, 820, 83

- Scoville, N., Lee, N., Vanden Bout, P., et al. 2017, *ApJ*, 837, 150
- Sharon, C. E., Riechers, D. A., Hodge, J., et al. 2016, *ApJ*, 827, 18
- Shu, F. H. 1991, *The Physics of Astrophysics* (University Science Books)
- Silk, J. 2013, *ApJ*, 772, 112
- Solomon, P. M., & Vanden Bout, P. A. 2005, *ARA&A*, 43, 677
- Spergel, D. N., Verde, L., Peiris, H. V., et al. 2003, *ApJS*, 148, 175
- Spitzer, L. 1978, *Physical processes in the interstellar medium* (John Wiley & Sons, Inc.)
- Stacey, G. J. 2011, *IEEE Transactions on Terahertz Science and Technology*, 1, 241
- Stacey, G. J., Charmandaris, V., Boulanger, F., et al. 2010a, *ApJ*, 721, 59
- Stacey, G. J., Geis, N., Genzel, R., et al. 1991, *ApJ*, 373, 423
- Stacey, G. J., Hailey-Dunsheath, S., Ferkinhoff, C., et al. 2010b, *ApJ*, 724, 957
- . 2010c, *ApJ*, 724, 957
- Stacey, G. J., Smyers, S. D., Kurtz, N. T., & Harwit, M. 1983, *ApJ*, 265, L7
- Stafford, R. P., Bell, K. L., & Hibbert, A. 1994, *MNRAS*, 266, 715
- Stoerzer, H., Stutzki, J., & Sternberg, A. 1997, *A&A*, 323, L13
- Tacconi, L. J., Genzel, R., Neri, R., et al. 2010, *Nature*, 463, 781
- Tayal, S. S. 2011, *ApJS*, 195, 12
- Tielens, A. G. G. M., & Hollenbach, D. 1985, *ApJ*, 291, 722

Vacca, W. D., Garmany, C. D., & Shull, J. M. 1996, *ApJ*, 460, 914

Valentino, F., Magdis, G. E., Daddi, E., et al. 2018, *ApJ*, 869, 27

Warren, S. J., & Dye, S. 2003, *ApJ*, 590, 673

Weiß, A., Henkel, C., Downes, D., & Walter, F. 2003, *A&A*, 409, L41

Wiese, W. L., Smith, M. W., & Glennon, B. M. 1966, Atomic transition probabilities. Vol.: Hydrogen through Neon. A critical data compilation (National Bureau of Standards)

Wild, W., Harris, A. I., Eckart, A., et al. 1992, *A&A*, 265, 447

Wolfire, M. G., Tielens, A. G. G. M., & Hollenbach, D. 1990, *ApJ*, 358, 116

Zhang, Z.-Y., Ivison, R. J., George, R. D., et al. 2018, *MNRAS*, 2001